HISTORY INDUCED CRITICAL SCALING IN DISORDERED MEDIA AND SUPER DIFFUSIVE GROWTH IN HIGHLY ADVECTIVE RANDOM ENVIRONMENTS

BY

JOHN HALSEY CARPENTER

B.S., Kansas State University, 1999

DISSERTATION

Submitted in partial fulfillment of the requirements
for the degree of Doctor of Philosophy in Physics
in the Graduate College of the
University of Illinois at Urbana-Champaign, 2004

Urbana, Illinois

UMI Number: 3153261

INFORMATION TO USERS

The quality of this reproduction is dependent upon the quality of the copy submitted. Broken or indistinct print, colored or poor quality illustrations and photographs, print bleed-through, substandard margins, and improper alignment can adversely affect reproduction.

In the unlikely event that the author did not send a complete manuscript and there are missing pages, these will be noted. Also, if unauthorized copyright material had to be removed, a note will indicate the deletion.

UMI®

UMI Microform 3153261

Copyright 2005 by ProQuest Information and Learning Company.

All rights reserved. This microform edition is protected against unauthorized copying under Title 17, United States Code.

ProQuest Information and Learning Company
300 North Zeeb Road
P.O. Box 1346
Ann Arbor, MI 48106-1346

CERTIFICATE OF COMMITTEE APPROVAL

University of Illinois at Urbana-Champaign
Graduate College

September 1, 2004

We hereby recommend that the thesis by:

JOHN HALSEY CARPENTER

Entitled:

HISTORY INDUCED CRITICAL SCALING IN DISORDERED MEDIA AND SUPER DIFFUSIVE GROWTH IN HIGHLY ADVECTIVE RANDOM ENVIRONMENTS

Be accepted in partial fulfillment of the requirements for the degree of:

Doctor of Philosophy

Signatures:

Karin Dahmen
Director of Research - Karin Dahmen

Head of Department - Jeremiah Sullivan

Committee on Final Examination*

Michael B Weissman
Chairperson - Michael Weissman

Paul M Goldbart
Committee Member - Paul Goldbart

Committee Member - Robert Clegg

Committee Member -

Committee Member -

Committee Member -

* Required for doctoral degree but not for master's degree

HISTORY INDUCED CRITICAL SCALING IN DISORDERED MEDIA AND SUPER DIFFUSIVE GROWTH IN HIGHLY ADVECTIVE RANDOM ENVIRONMENTS

John Halsey Carpenter, Ph.D.
Department of Physics
University of Illinois at Urbana-Champaign, 2004
Karin A. Dahmen, Advisor

The behavior of non-equilibrium systems in the presence of quenched random disorder is studied. In noisy, hysteretic systems, the role of driving force history is studied in the context of the non-equilibrium, zero-temperature Random Field Ising Model (RFIM). The RFIM was originally developed as a simple model for disordered magnets, but has applications far beyond magnetic systems. Previous work examining history effects in models and experiments are briefly reviewed, followed by a summary of the saturation loop behavior of the RFIM. A numerical scaling analysis of the AC demagnetization curve of the RFIM is performed, examining the effect of the underlying disorder on avalanche size distributions, correlation functions, and spanning avalanches. Furthermore, a similar scaling analysis for nested, concentric, symmetric subloops is performed via an analysis of history-induced disorder. Next the effects of long range demagnetizing fields on the demagnetization curve and subloops are studied. Finally, an analysis of corrections to scaling for subloops is presented, along with a derivation of the exponent relations.

Disorder in population biology is studied for the case of a spreading cluster of bacteria in a highly advective environment with inhomogeneous nutrient concentration. A model reaction-diffusion equation with Fisher growth terms is introduced with a brief discussion of previous work on similar equations and experiments. The linear two-dimensional problem is mapped onto a simplified one-dimensional equation. Numerical simulations of concentration profiles reveal anomalous growth and super-diffusive spreading in the direction perpendicular to the convection velocity. A time characterizing the crossover from pure diffusion to this super-diffusive behavior is perturbatively calculated. The crossover time's dependence on the velocity and disorder strength is then tested numerically. Two-dimensional simulations of the full linear reaction-diffusion equation also show the onset of super-diffusive growth in concentration contour maps. On the other hand, with nonlinear growth in two dimensions, a symmetric wave front develops with a propagation velocity greater than the minimum Fisher velocity. An expression is derived and tested for this velocity.

Acknowledgments

Foremost I wish to thank my advisor Karin A. Dahmen for recommending very interesting research topics as well as for the excellent suggestions, criticisms, and attention to detail which has greatly improved the quality of this work. I would also like to recognize my other committee members, Michael B. Weissman, Paul M. Goldbart, and Robert M. Clegg for their many useful questions and comments. I am particularly grateful to Andrea Mills, Michael Weissman, Andreas Berger, and Olav Hellwig for providing experimental data testing the predictions of this work. I also thank my other collaborators, Jim Sethna, Gary Friedman, Ali Vanderveld, and Sharon Loverde for many helpful suggestions and conversations. Finally, I would like to thank the many other people with which I have had discussions, including Robert White, Ferenc Pazmandi for his suggestion to use H_{max} as a scaling variable instead of M_{max}, David Nelson, Nadav Shnerb, and Amit Mehta.

This work was supported by NSF grants DMR 99-76550 (MCC), DMR 03-25939 ITR (MCC), DMR 00-72783, and DMR 03-14279 as well as an A. P. Sloan Fellowship (to K. Dahmen). The extensive simulations were also made possible thanks to a generous equipment award through the IBM Shared University Research Program and through the use of the Materials Computation Center's IBM Workstation Cluster.

Table of Contents

List of Tables ix

List of Figures x

Chapter 1 Introduction 1

Chapter 2 History in Hysteresis 4
- 2.1 Models 5
- 2.2 Experiments 8

Chapter 3 The Random Field Ising Model 13
- 3.1 Critical Behavior 14
- 3.2 Behavior with Long Range Anti-Ferromagnetic Forces 17
- 3.3 Previous Work on Field History 18
- 3.4 Notation 19

Chapter 4 Demagnetization 20
- 4.1 Algorithm 20
- 4.2 Critical Transition 21
- 4.3 Critical Scaling 22
  - 4.3.1 Integrated Avalanche Size Distribution 23
  - 4.3.2 Integrated Spin-Flip Correlation Function 24
  - 4.3.3 Number of Spanning Avalanches 24
  - 4.3.4 Second Moments of Integrated Avalanche Size Distribution 26
  - 4.3.5 Jump in Magnetization due to Spanning Avalanches 27
  - 4.3.6 Scaling Summary 28

Chapter 5 Subloops 30
- 5.1 Critical Transition 31
- 5.2 Critical Scaling 33
  - 5.2.1 Integrated Avalanche Size Distribution 34
  - 5.2.2 Integrated Spin-Flip Correlation Function 35
  - 5.2.3 Second Moments of Integrated Avalanche Size Distribution 36
  - 5.2.4 Number of Spanning Avalanches 37
  - 5.2.5 Scaling Summary 39

Chapter 6 Long Range Forces **42**
- 6.1 Concentric, Symmetric Subloops 42
- 6.2 Demagnetization Curve 47

Chapter 7 Scaling Considerations **49**
- 7.1 Corrections to Scaling 50
- 7.2 Exponent Relations 54
  - 7.2.1 Relations from History-Induced Scaling 55
  - 7.2.2 Relations from Demagnetization Curve 56
  - 7.2.3 Unconstrained Exponents 58

Chapter 8 Introduction to Population Biology **60**
- 8.1 Large Velocity Simplification 63

Chapter 9 One-Dimensional Spreading **65**
- 9.1 Perturbation Expansion 66
  - 9.1.1 Diffusion Crossover Time 69
- 9.2 Numerics 70
  - 9.2.1 Concentration Profiles 71
  - 9.2.2 Anomalous Growth 73
  - 9.2.3 Diffusion Exponent 76
  - 9.2.4 Crossover Time Behavior 77

Chapter 10 Two-Dimensional Spreading **80**
- 10.1 Linear Equation 81
  - 10.1.1 Concentration Contours 82
  - 10.1.2 Population Width 88
- 10.2 Nonlinear Equation 90
  - 10.2.1 Concentration Contours 90
  - 10.2.2 Wave Front Velocity 91
  - 10.2.3 Theoretical Wave Front Velocity 95

Appendix A Random Field Ising Model Simulation Code **97**
- A.1 Interface 97
  - A.1.1 General Commands 99
  - A.1.2 Demagnetization 99
  - A.1.3 Subloops 101
- A.2 Search Algorithm 104
- A.3 Back-Flip Algorithm 106

Appendix B Spreading Simulation Code **109**
- B.1 1-D Code 109
- B.2 2-D Code 110
  - B.2.1 Linear vs. Nonlinear Growth 114

Appendix C Experimental Noise Determination **115**

References 120

Curriculum Vitae 127

List of Tables

4.1 Relations between exponents 29

5.1 Universal critical exponents 41

List of Figures

2.1 Concentric subloops for two thin film samples 9
2.2 Experimental avalanche size distributions 11

3.1 Saturation hysteresis loops 15
3.2 Saturation hysteresis loop with long range forces 18

4.1 Demagnetization curves 22
4.2 Integrated avalanche size distributions 23
4.3 Integrated spin-flip correlation functions 25
4.4 Number of system spanning avalanches 25
4.5 Second moments of the integrated avalanche size distribution 27
4.6 Size of the magnetic discontinuity 28

5.1 Concentric inner subloops above the critical disorder 31
5.2 Concentric inner subloops below the critical disorder 32
5.3 Integrated avalanche size distributions 35
5.4 Integrated spin-flip correlation functions 36
5.5 Second moments of the integrated avalanche size distribution 37
5.6 Number of spanning avalanches 38

6.1 Saturation loop and concentric subloops with long range forces 43
6.2 Avalanche size distributions with long range forces 44
6.3 Integrated avalanche size distributions with long range forces 45
6.4 Demagnetization curve with long range forces 47
6.5 Integrated avalanche size distributions with long range forces for the demagnetization curve 48

8.1 Fisher wave in one dimension 62

9.1 Diagrammatic representation of the Fourier-Laplace transformed, simplified equation 67
9.2 Concentration profiles for one-dimensional spreading 72
9.3 Average concentration profiles for one-dimensional spreading 74
9.4 Total population vs. time for a disordered environment 75
9.5 Concentration width vs. time for a disordered environment with $v = 4.0$ and $\Delta = 4.0$ 76
9.6 Concentration width vs. time for a disordered environment with $v = 4.0$ and $\Delta = 1.0$ 78

9.7 Crossover time dependence on Δ and v 79

10.1 Concentration contours for two-dimensional spreading 83
10.2 Average concentration contours for two-dimensional spreading 85
10.3 Two-dimensional spreading contours for small concentrations 86
10.4 Total population vs. time for two-dimensional spreading 87
10.5 Concentration width vs. time for a two-dimensional disordered environment 89
10.6 Concentration contours with a carrying capacity for two-dimensional spreading 92
10.7 Population diameter vs. time for nonlinear spreading 93

A.1 Schematic of the subloop detection algorithm 102

C.1 Barkhausen noise 115
C.2 Noise window power spectra 117
C.3 Voltage offsets 118
C.4 Avalanche size distributions 119

Chapter 1

Introduction

A typical starting point in modeling real systems centers around a simple model that usually assumes a general homogeneity of the environment. However it quickly becomes apparent that quite often mother nature is inherently "dirty" and so the simplistic view breaks down. These inhomogeneities have been analyzed in the context of disorder by adding in random elements into the various models. Herein, two separate phenomena each with an underlying connection to random disorder will be examined, history's role in systems with crackling noise and super-diffusive spreading in a reaction diffusion system with strong convection.

When a system far from equilibrium is driven by an external force hysteresis occurs. The system state then depends on the history of the external force. In many systems such as ferromagnets [1], superconductors [2; 3], and martensites [4], the response to the driving force is not continuous but occurs in discrete jumps which are often referred to as "crackling noise", or specifically for magnets, Barkhausen noise. In magnets, broad ranges of power-law scaling of noise have been attributed to either a disorder-induced critical point, such as the one found in the non-equilibrium zero-temperature random-field Ising model (RFIM) [5], or to self-organized criticality (SOC) [6], as found in soft magnets.

The study of population growth is an integral part of the biological sciences.

Recently the behavior of microbial species, such as bacteria, has enjoyed much mathematical analysis due to the formation of intricate equilibrium patterns [7; 8]. Due to environmental and health concerns the behaviors in driven systems is also of interest. In this regime the dynamics are typically described using reaction-diffusion equations which may involve a number of species and their interactions [7]. While much work has been done on these types of systems, the inclusion of inhomogeneities in the environment has received limited attention. The addition of disorder may manifest itself in a variety of ways, from spatial variations in the available food or in the presence of poisons to random diffusion constants.

The text is laid out as follows. First the effect of history on the behavior of crackling noise is examined in Chs. 2 - 7. Chapter 2 starts out with a brief review of the role of field history in hysteresis models and experiments, including a more detailed look at three experiments more closely connected to the author's work and which display behaviors predicted in later chapters. An overview of the saturation loop behavior for the RFIM is then given in Ch. 3. Following this are two chapters that numerically examine the scaling that arises when field history is included, first looking at the demagnetization curve in Ch. 4 and then at concentric, symmetric subloops in Ch. 5. Next, Ch. 6 examines the same field histories as in Chs. 4 and 5 in the context of long range demagnetizing fields. A concluding chapter, Ch. 7, provides a look at two scaling details, namely corrections to the scaling behavior in Ch. 5 and the derivation of the relations between the various critical exponents. Details on the simulation code are found in App. A along with an explanation of the experimental analysis used to obtain Fig. 2.2 in App. C.

The second portion of the text, Chs. 8 - 10 focus on the bacteria spreading problem. An introduction to some previous work and experiments as well as the governing equation are given in Ch. 8. Following this, Ch. 9 considers a simplified one-dimensional case both from a theoretical perspective using perturbation techniques as well as through numerical simulations. Finally, the full two-dimensional case is examined numerically for both linear and non-linear growth in Ch. 10. For the latter case a simple relation describing the spreading behavior is derived. Appendix B gives details of the simulation code.

Chapter 2

History in Hysteresis

The role of disorder in hysteretic processes is not a new subject. As mentioned in Ch. 1 a wide range of experimental systems exhibit these behaviors. The saturation hysteresis loop, the loop swept out when moving between oppositely saturated states, is typically measured in experiments. This curve has been studied in detail in the context of a disorder-induced critical point, with an analysis of related experiments found in Ref. [9]. More recently, many new experiments have been performed looking at this area, including a first demonstration of the critical point in thin films [10]. While the saturation loop is an interesting topic, herein the focus is on the role of history in relation to the critical behavior of the saturation loop. For this reason, in the following a brief review of the role of history in hysteresis, for both model and experimental systems will be examined in Secs. 2.1 and 2.2. A more detailed look at three experiments related to the subloop behaviors of Chs. 5 and 6 will also be given at the end of Sec. 2.2.

Taking a brief sojourn into terminology, the addition of history has produced a range of descriptions. In later chapters, the behavior of subloops and the demagnetization curve will be discussed. Typically in the literature the term minor loop is used instead of subloop to represent a closed loop with at least one endpoint that does not fall on the saturation curve. Also falling in this category are reversal curves and recoil curves [11]. These generally start from the saturation loop at intermediate fields and do not close, with only one hysteresis branch being examined. The demagnetization curve studied in Ch. 4 is that curve drawn out as the field is increased, or decreased, from the AC demagnetized state. This curve also goes by the phrases AC demagnetization curve, virgin curve, and initial curve [11]. The latter two cases refer to the first curve obtained from a sample prepared in zero field and so the state of the sample most likely does not reside in the same microscopic state as the AC demagnetized state. It should be noted that the literature often associates the term "demagnetization curve" with a hysteresis branch that ends in zero magnetization, an entirely different situation to that of Ch. 4. Finally, there is also an anhysteretic demagnetization curve, or simply anhysteretic curve, which is given by the equilibrium magnetization at each field. It has been argued that this curve may be obtained by an AC demagnetization around a bias field [12], although again the final state may not necessarily be the corresponding equilibrium state [13].

2.1 Models

One of the most popular models to describe hysteresis is the Preisach model, which consists of a set of non-interacting domains each with an independent hysteresis loop of variable width [14]. The state of the system, for example the magnetism in ferromagnets, is given by the linear superposition of the magnetization of each of these domains' hysteresis loops. This phenomenological model is fit to describe an experimental system by adjusting the distribution of widths and amplitudes for the domain hysteresis loops via a given set of experimental hysteresis curves [11]. The two main characteristics of the Preisach model that pertain to the field history are return-point memory and subloop congruence. The former refers to the fact that when a minor loop is closed, the system returns to the identical microscopic state.

In the latter, subloops performed with endpoints of identical field values have identical shapes regardless of the starting magnetization [11]. Due to the simplicity of the Preisach model, many experiments introduce history in the form of subloops to test their congruence and thus the model applicability. These experiments cover many different phenomena including magnets [15; 16], martensites [17; 18], superconductors [19], resistance-temperature measurements of VO_2 films [20], a spin-state transition [21], and fluid invasion in porous media [22; 23]. Very often the congruence test fails, and so many modifications have been made to the Preisach model to make it behave more appropriately, leading to broken congruence and better fits to the experiments [15; 24–32].

The Jiles-Atherton model has also been used to model magnetic hysteresis. The model takes as its starting point the anhysteretic curve and computes hysteresis loops from energetic considerations arising from the pinning of domain walls by defects [33]. This results in five physical parameters that one must fit to an experimental system by measuring values along the initial, anhysteretic, and saturation curves [34]. Experiments have used this model to fit the initial curve, saturation curve and minor loops [34]. As does the Preisach model, the basic Jiles-Atherton model fails in fitting many experimental data, particularly for large fields, so a number of adaptations have been made to increase the agreement with experiments [35–38].

The Stoner-Wohlfarth model [39] is another energetic model, based on non-interacting particles with uniaxial anisotropy. While no longer widely used, it has an interesting prediction for the effect of history. In particular, it predicts that the initial magnetization curve is equal to half the shifted saturation curve [40]. In this context the saturation curve is often referred to as a demagnetization curve. To test this relation in experimental systems, a Henkel plot is used which plots the initial magnetization curve versus the saturation curve [41]. Deviations from a straight line with slope -2 indicates disagreement with this model, that inter-particle interactions are present. Such deviations have been found in many experiments [16; 42–44].

In the realm of soft magnetic materials with multiple domain walls, the ABBM model [45] has been widely used. As with the previous models its goal is to fit the experimental data through the adjustment of the various physical parameters relating to an experiment [46]. The model has one degree of freedom describing the mean position of a magnetic domain wall in a random pinning potential. Closely related is the mean field version of the random field Ising magnetic domain wall model of Ref. [47].

A final class of models is based on Ising spin systems. The models typically include some sort of random parameter or coupling in the model's Hamiltonian to mimic disorder in experimental samples. For example, these random terms may be random anisotropies [48], random bonds [49], random fields [5], and random coercivities [50]. Depending on the choice of random term and distribution these models may break return point memory [48–50], although this is not always the case [5]. On the other hand congruence of subloops is always broken by the interaction present in these systems. Upon varying the strength of disorder, these models exhibit the same second-order phase transition in their saturation loops [5; 48; 49] and lie in the same universality class, assuming that the spin interactions are on average ferromagnetic. On the other hand, a transition similar to that found in the classical anti-ferromagnetic Ising model arises when the interactions are on average anti-ferromagnetic [50]. In Chs. 5-6, the Random Field Ising Model (RFIM) with ferromagnetic nearest neighbor interactions will be used to explore the effect of history in relation to the former critical point and so a more detailed description of its representative behavior may be found in Ch. 3.

The study of superconductors has also led to several different models to explain hysteretic behavior. These so called critical-state models—critical in that they describe a critical current density found in a sample—include the Bean model [51], the exponential model [52] and the Kim-Anderson model [53; 54]. The initial magnetization curve as well as concentric, symmetric subloops have been calculated for the exponential model for a range of parameters describing the shape of the saturation loop [52]. For small values of the field these typically look similar to those found in Fig. 5.1. Subloops in the Kim-Anderson model [55; 56] and a modified Bean model [57] have also been explored and resemble the inner loops of Fig. 5.1. Lastly, a general formalism for minor loops of critical-state models has been developed [58].

There exists a wide range of other magnetic hysteresis models many of which have included the effects of field history with measurements of nested subloops and the demagnetization curve. Some of these are a scalar model [59], a transplantation model [60], an energetic model (Hauser model) [61], and a thermodynamic model [62].

2.2 Experiments

Generally, magnetic samples are formed in zero magnetic field. Therefore experimental investigations naturally begin with measurements of the initial magnetization curve. Considering the transition found in the saturation loop of models such as the RFIM [5] and the first measurements of such a transition in magnetic materials [10], coupled with the Wohlfarth prediction of similar behavior between saturation and demagnetization, it seems reasonable to expect that a similar transition may be found in the demagnetization curve. In experimental systems, changing the disorder can involve, for example, changing the relative concentration of the constituent atoms. To observe a possible transition, this concentration change would need to change the slope of the demagnetization curve. This type of experiment has been done for $SmCo_5/\alpha$-Fe nano-composites, where increasing the Fe content showed signs of increasing steepness in the initial curves [63]. Similar behavior was found in Al-substituted haematites, with increasing Al concentration decreasing the steepness [64]. The addition of M = Fe, Zr, and/or Cu to a 40% $SmCo_5$ + 60% $Sm_2(Co,M)_{17}$ powder

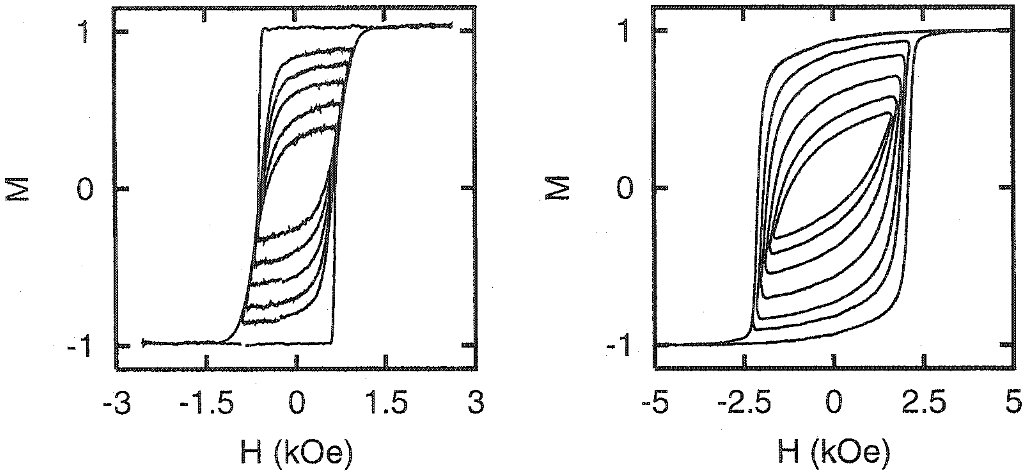

Figure 2.1: Concentric subloops for two thin film samples. On the right, curves for a CoPtCrB alloy thin film are shown as measured using an Alternating Gradient Magnetometer. The plot on the left displays subloops for a Co/Pt multilayer thin film as measured in a MOKE setup. The experiments were performed by A. Berger and O. Hellwig respectively (see Ref. [69]).

also caused slightly steeper initial curves [65] with similar results for $Sm_{12}(Co,M)_{88}$ compounds [42]. Furthermore, $Sm(Co,Cu)_7$ ribbons showed increasing steepness for increasing Cu concentrations [66] as did Nd_xFeB compounds upon increasing the Nd concentration [67].

While the analysis in Ch. 5 of nested symmetric, concentric subloops in terms of critical behavior has only recently been suggested [68; 69], nested subloops have been measured previously on a variety of experimental systems. To obtain a feeling for the two general types of behavior possible, two thin film experiments measuring magnetization curve will be examined. The magnetization curves for symmetric, concentric subloops are shown for the two different thin films in Fig. 2.1. The Co/Pt multilayer sample shown on the left side of Fig. 2.1 has the field applied perpendicular to the plane of the sample. Due to the strong interface anisotropy of such multilayer samples [70], the easy axis of magnetization is perpendicular to the film plane even though the long range demagnetizing effect is largest in this direction [71], due to magnetostatic poles along the entire surface of the sample which impose a labyrinth structure of domains [72]. Despite the fairly rectangular major loop shape, indicating easy-axis orientation, the loop exhibits an extended linear segment on which all minor loops merge due to the presence of long range dipolar effects. Detailed studies show that domain wall propagation rather than nucleation presides in this region [72; 73]. The analog of this behavior, seen in Fig. 6.1, is discussed in terms of the RFIM in Ch. 6. There have been other experimental systems where similar behavior has arisen. In particular, in amorphous $Fe_{21}Co_{64}B_{15}$ and nanocrystalline $Fe_{86}Zr_7Cu_1B_6$ [15], Co/Pd multilayers [74], and for a MnBi thin film [75]. Nested subloops have also been measured for other soft ferromagnetic materials, but do not show such a clear behavior as in Fig. 2.1. Some examples are 9S20 and C15 samples [26]. Additionally, $BaFe_{12}O_{19}$ perpendicular thin films [76] displayed a mix of the two behaviors shown in Fig. 2.1.

A different situation is found in the right panel of Fig. 2.1. There the measured CoPtCrB alloy film is polycrystalline, with grain sizes narrowly distributed around 10 nm diameter. It exhibits strong exchange coupling between grains. Here the magnetization is in the plane of the sample. As magnetostatic surface poles only occur on the boundaries, the corresponding demagnetizing field is minimal and negligibly affects the system's behavior. This fact results in loops that no longer contain a shared linear portion. Instead, as one moves to more deeply nested loops, the loops become thinner and increasingly sheared. A very similar behavior is found in the RFIM (see Fig. 5.1) and is discussed in detail in Ch. 5. There is a small difference between this sample and the loops of Fig. 5.1 in that there is a greater shearing found for the thin film. This is due to long range ferromagnetic interactions arising from stray fields which are neglected in Ch. 5. A number of similar magnetization curves have been previously measured. These include the hard magnet AlNiCo [26] which has a asymmetric magnetization final state due to a large changes in the field between loops (see Ch. 5), $[Ba,Sr]Fe_{12}O_{19}$ ferrites [77], Co/Cr multilayer films [78], 3.5% FeSi-steel (ARMCO M6) [61], nanocrystalline SmFeCo [16] and ex-

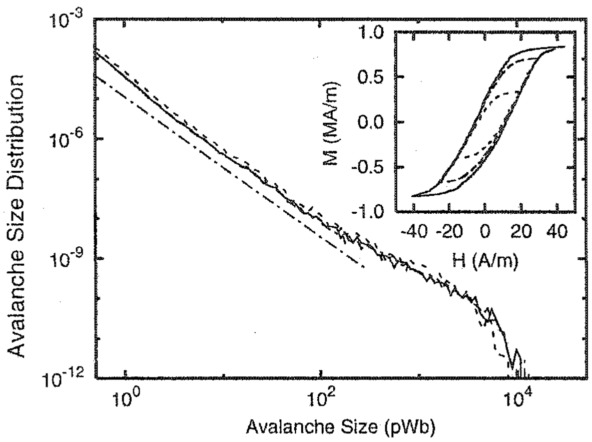

Figure 2.2: Experimental avalanche size distributions for subloops of a soft ferromagnet. The three subloops analyzed are shown in the inset, with the largest corresponding to the saturation loop. The distributions were extracted from a window of width $\Delta H \approx 20A/m$ which started near $H = 0A/m$. A power law of -1.75 is shown by the offset, dash-dot line. The experiment was performed by A. Mills and M. Weissman (see Ref. [69]).

change coupled $Sm_{18}(Fe,Co)_{82}$ alloys [79], nano-composite $Nd_{3.6}Pr_{5.4}Fe_{83}Co_3B_5$ [80], a 0.4 wt% carbon steel [30], annealed 3% nickel steel [81; 82], Nd(Dy)-Fe-B thin films on Si(111) or Ta/Si(111) with an asymmetric final magnetization [83], CoSm/FeCo thin films [84], and a micromagnetic finite element calculation simulating nanocrystalline $Pr_2Fe_{14}B$ [85]. Such histories have also been measured for a Bi-2223 filament superconductor [86], a superconducting NdBCO crystal [87], and for martensites [88].

Experiments that measure the noise associated with hysteretic behavior are less common, even less so when considering the effect of field history. The noise along subloops has been measured to test the extent of return-point memory found in soft magnets [89]. One experiment that measures the pulse size distribution of the Barkhausen noise in nested subloops of a soft ferromagnet is shown in Fig. 2.2. The sample was a 21 cm x 1cm x 30 μm ribbon (an effective three dimensional system) of a $Fe_{21}Co_{64}B_{15}$ amorphous alloy. With the magnetization and applied field in-plane, this soft magnet forms multiple stripe domains with their walls parallel to the field [47], indicating net anti-ferromagnetic long range forces. In the experiment, a solenoid provided a triangular driving field along the long axis of the sample, varying slow enough (at 0.03 Oe/s) to prevent overlapping of avalanches, which were measured with a pick-up coil. The first cycle drove the sample to saturation, while subsequent cycles drove the field through nested subloops. Integrating the pick-up voltage yields the magnetization, and the resulting hysteresis loops are shown in the inset of Fig. 2.2. The avalanche distributions for the subloops all display the same power-law exponent and cutoff size, indicating that the system is self-organized critical [6; 47; 90]. The field is simply driving the domain walls back and forth through the system. The measured power-law exponent (1.75) is larger than has been predicted and measured for the saturation loop ($1.25 - 1.5$) [47; 90]. This is due to $M(H)$ not being strictly linear in the window analyzed. Choosing a smaller window closer to the linear regime results in an exponent 1.45 ± 0.15, consistent with the mean-field exponent $\tau = 1.5 - c/2$ [47], with the sweep rate $c \approx 0.1$ taken into account. This sample's behavior coincides well with the behavior of the RFIM described in Ch. 6, and the comparison is justified by arguments presented in Ch. 3. A description of the data analysis performed to obtain Fig. 2.2 is given in App. C.

Chapter 3

The Random Field Ising Model

The Random Field Ising Model (RFIM) is studied at zero temperature and far from equilibrium. The RFIM places spins $s_i = \pm 1$ on a hyper-cubic lattice. The energy of a system with N spins is then given by [90]

$$\mathcal{H} = -J \sum_{\langle ij \rangle} s_i s_j - \sum_i (h_i + H) s_i + \frac{J_{LR}}{N} \sum_{ij} s_i s_j. \tag{3.1}$$

The first term of Eq. (3.1) couples nearest-neighbor spins ferromagnetically ($\langle ij \rangle$ implies summing over nearest-neighbor pairs of spins). The next two terms couple the spins to an external field H as well as a site dependent local field h_i. This local field is randomly chosen from a Gaussian distribution, $\rho(h_i) = \frac{1}{\sqrt{2\pi}R} \exp(-\frac{h_i^2}{2R^2})$. Here the standard deviation R of the random distribution is termed the "disorder". Finally, the last term of Eq. (3.1) couples the spins through an infinite-range mean-field antiferromagnetic (AF) interaction. This AF coupling models the dipole interactions such as are relevant in soft ferromagnets. For a single elastic domain wall, Zapperi, et al. [6; 47] have shown that the upper critical dimension is reduced from five to three dimensions upon introduction of dipole interactions. Hence in three dimensions the AF dipole interactions may be described by a mean-field demagnetization term, such as in Eq. (3.1), and the long range ferromagnetic interactions by infinite-range mean-field interactions along the domain wall [47]. This is the situation for the soft ferromagnet experiment of Sec. 2.2, and the mean-field limit of Eq. (3.1) describes its behavior. Additionally, when the experimental sample has stress applied along the direction parallel to the domain walls, stress-induced local anisotropies become dominant and the ferromagnetic interactions from dipole fields become negligible [91]. In this case, the ferromagnetic interactions are effectively short ranged, so the three dimensional version of Eq. (3.1) applies. For experiments where the long range dipole fields are negligible one may choose $J_{LR} = 0$ thus resetting Eq. (3.1) to the purely ferromagnetic RFIM. Note that two types of dynamics are possible. One imposing propagation of a domain wall [92] and one allowing the nucleation of avalanches [5]. Herein only the latter case is examined.

Simulations of the above model are run by starting with the external field at $H = -\infty$, thus saturating the system with all spins down ($s_i = -1$). The field is then adiabatically slowly (at zero sweep-rate) taken through a particular path, or history. As the field H changes, spins are induced to flip when the effective local field, $h_i^{\text{eff}} = H + h_i + J\sum_{\langle ij \rangle} s_j - J_{LR}M$, changes sign. Here $M = \frac{1}{N}\sum_i s_i$ is the magnetization of the system. The initial spin flip, which may be in either direction depending on the direction of change in H, may induce its neighboring (or for $J_{LR} \neq 0$ even distant) spins to flip. This creates an avalanche of flipping spins which is the analog of a Barkhausen pulse. To ensure adiabaticity, the external field remains fixed during an avalanche, changing only after the avalanche terminates. The simulations use an algorithm that stores the random fields, ensuring exact microscopic return point memory for $J_{LR} = 0$ [93]. Details on the code may be found in App. A.

3.1 Critical Behavior

In the absence of long range AF forces, $J_{LR} = 0$, the RFIM (with nucleation dynamics) exhibits a non-equilibrium second-order phase transition, due to the competing

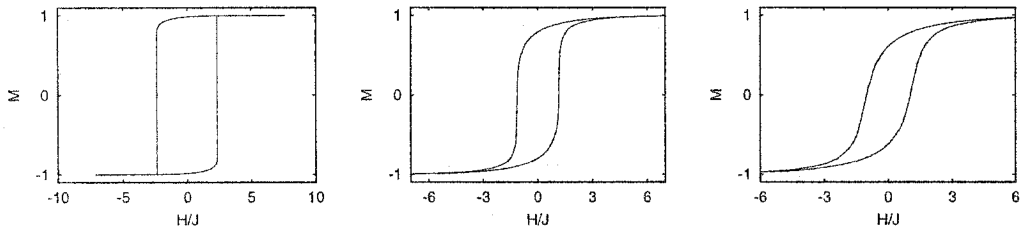

Figure 3.1: Saturation hysteresis loops for 10^5 systems at disorders of $4J$, $6.1J$, and $7J$ from left to right. For low disorder (left plot) a large jump in magnetization occurs, while for high disorder (right plot) the hysteresis loop is smooth. A transition occurs in the intermediate disorders where the jump in magnetization becomes a point singularity in the slope (center plot).

forces of the random fields and the ferromagnetic nearest-neighbor coupling [5]. The transition, as it appears in the shape of the saturation hysteresis loop, is shown in Fig. 3.1. Below the critical disorder $R_c = 2.16J$ (in three dimensions), the ferromagnetic interactions dominate the energetics, causing there to be a finite jump discontinuity in the hysteresis curve (left side of Fig. 3.1). This jump scales to zero as one approaches the critical disorder as $\Delta M \sim (R_c - R)^\beta$ where β is a universal exponent with $\beta = 0.035 \pm 0.028$ in three dimensions [5]. At the critical disorder R_c, corresponding to the center of Fig. 3.1, there is a single point of infinite slope. Around this point, the magnetization exhibits power-law scaling, $M(H) - M_c \sim (H - H_c)^{1/\delta}$, where $H_c = 1.435J$ (for the increasing branch of the hysteresis loop) and δ is another universal exponent with $\beta\delta = 1.81 \pm 0.32$ in three dimensions [5]. Above the critical disorder the random fields dominate Eq. (3.1) and the hysteresis curves become smooth, containing mostly small avalanches. This case is shown on the right side of Fig. 3.1. The values of R_c, H_c, and M_c are all non-universal.

Many quantities associated with this critical point display scaling behavior for $R \to R_c$. In the following some of these quantities will be briefly reviewed. A more detailed discussion is given in Ref. [94]. The first quantity of interest is the (field) integrated avalanche size distribution $D_{\text{int}}(S, R)$, which is a histogram of avalanche sizes S, and scales as [94]

$$D_{\mathrm{int}}(S,R) \sim S^{-(\tau+\sigma\beta\delta)}\bar{\mathcal{D}}_{+}^{\mathrm{int}}(S^{\sigma}(R-R_c)), \tag{3.2}$$

where $\bar{\mathcal{D}}_{+}^{\mathrm{int}}$ is a universal scaling function and $\tau+\sigma\beta\delta$ (as well as σ) are universal exponents with values given in Table 5.1. As $R \to R_c$ from above, the avalanche size distribution shows increasing decades of power-law scaling, up to a cutoff size which grows as $S_{\max} \sim (R-R_c)^{-1/\sigma}$. Near the critical point $S_{\max}$ reaches the system size.

The (field) integrated spin-flip correlation function $G_{\mathrm{int}}(x,R)$, which measures the probability that a spin a distance x from the start of an avalanche will flip in the same avalanche, also displays scaling behavior according to the form [94],

$$G_{\mathrm{int}}(x,R) \sim x^{-(d+\beta/\nu)}\mathcal{G}_{+}(x(R-R_c)^{\nu}). \tag{3.3}$$

Again $\mathcal{G}_{+}$ is a universal function, $d+\beta/\nu$ and ν are universal exponents with values as given in Table 5.1, and d is the dimension of the system. The correlation function also has a cutoff length given by the correlation length, $\xi \sim (R-R_c)^{-\nu}$. It reaches the system length near R_c.

As the correlation length reaches the system length, spanning avalanches appear in the system. These are avalanches that propagate across the entire length L of the system, thus touching opposite boundaries. The number of spanning avalanches $N(L,R)$ in a hysteresis loop is measured by summing the number of directions the avalanches span and then dividing by the system dimension. The jump in magnetization due to these spanning avalanches $\Delta M(L,R)$ is calculated by summing the sizes of all the spanning avalanches and normalizing by the system size. Both the number of spanning avalanches and the jump in magnetization due to the spanning avalanches display finite-size scaling as the disorder is changed. The scaling forms are [94]

$$N(L,R) \sim L^{\theta}\mathcal{N}_{+}(L^{1/\nu}(R-R_c)) \tag{3.4}$$

and

$$\Delta M(L,R) \sim L^{-\beta/\nu}\Delta\widetilde{\mathcal{M}}_{\pm}(L^{1/\nu}(R-R_c)), \tag{3.5}$$

respectively. Similar to the scaling forms of the avalanche size distribution and correlation function, both $\mathcal{N}_+$ and $\Delta\widetilde{\mathcal{M}}_{\pm}$ are universal scaling functions and θ, β/ν, and ν universal exponents, listed in Table 5.1.

The final quantity of interest, the second moment of the integrated avalanche size distribution, is calculated as $\langle S^2\rangle(L,R) \equiv \sum_i S_i^2/\sum_i S_i$ where the sums run over all avalanches in the loop. It also displays finite-size scaling with the form [94]:

$$\langle S^2\rangle(L,R) \sim L^{\rho}\tilde{\mathcal{S}}_{+}^{(2)}(L^{1/\nu}(R-R_c)). \tag{3.6}$$

Again, $\tilde{\mathcal{S}}_{+}^{(2)}$ is a universal scaling function and $\rho \equiv -(\tau+\sigma\beta\delta-3)/\sigma\nu$ and ν are universal exponents, given in Table 5.1.

3.2 Behavior with Long Range Anti-Ferromagnetic Forces

Now turning to the case where long range anti-ferromagnetic forces are important, one finds a much different picture for the saturation loop than in Section 3.1. Instead of a disorder-induced critical point, for $R < R_c$ the system appears to behave as if operating at a self-organized critical (SOC) point [95], assuming $J_{LR} \sim 1/L$ for linear system size L [47]. An example saturation loop is shown in Fig. 3.2. As the field is increased from saturation the hysteresis curve follows a nearly identical path to the the case with $J_{LR} = 0$ until reaching an onset avalanche, which corresponds to the onset of the large system-spanning avalanche when $J_{LR} = 0$. After this point the magnetization behaves linearly with increasing field, the slope being dependent on the strength of J_{LR}. The avalanche size distribution along the linear portion of the hysteresis curve displays a power-law, regardless of the disorder value for $R < R_c$.

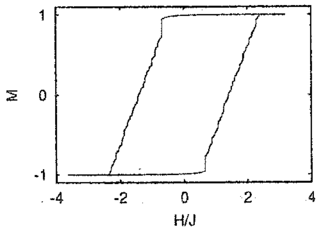

Figure 3.2: Saturation hysteresis loop with long range forces at a disorder of $R = 1.8J$ and $J_{LR} = 0.25J$ in a 100^3 system. After an onset avalanche the hysteresis curve becomes linear.

Again this indicates that the system is SOC [6; 47; 90]. The main effect of the demagnetization field is to force the system to operate near the interface depinning point [47; 96]. At the onset avalanche, a large domain develops in the system, after which further increases of the field push this domain wall (interface) through the system. Note that the model does not require avalanches to nucleate only at the domain wall. However, the anti-ferromagnetic interactions suppress the nucleation of large avalanches far ahead of the interface, resulting in the simple domain wall motion. The exponents governing the avalanche size distribution and other quantities have been measured, and the model has been shown to be in the same universality class as the front propagation model, which requires avalanches to nucleate at the domain wall [90].

3.3 Previous Work on Field History

Only recently has work been done on understanding the role of history in the RFIM. These studies include exact solutions of the RFIM, with field reversal, in one dimension [97] and on the Bethe lattice [98]. The demagnetization curve has also been computed on the Bethe lattice [99] and also an examination of the Rayleigh Law near the demagnetized state has been made [99–101]. Numerical studies have also recently been undertaken, including examining the behavior of First Order Reversal Curves (FORCs) [102], which provide an alternative view of the effect of history to the results presented herein. Additionally, early reports of the author's work on the scaling of subloops [68; 69] and the demagnetization curve [103] will be repeated and extended in the later chapters.

3.4 Notation

In the scaling analyses of the demagnetization curve (Ch. 4) and subloops (Ch. 5) three new sets of exponents and scaling functions will be introduced. The notation will provide a subscript letter for each new set. These letters are d for the demagnetization curve, f for the history induced scaling, and l for the critical subloop. The exponents related to the saturation loop will remain bare. So for example, the three new exponents associated with the saturation loop's σ will be σ_d, σ_f, and σ_l respectively. The relations between all these new quantities will be discussed in Ch. 7.

Chapter 4

Demagnetization

4.1 Algorithm

In the laboratory, the AC demagnetization of a sample involves first applying a sufficiently large magnetic field to saturate the sample followed by a "ringdown", in which the field oscillates with an amplitude that slowly decreases to zero. This brings the sample to the demagnetized state. As one then reapplies a slowly increasing field, the demagnetization curve is traced out. One uses a similar process to simulate the demagnetization curve. A simulation begins with all spins down and the driving field at negative infinity. The field is then increased as if one were tracing out the lower part of the saturation hysteresis loop. However, one stops immediately before the last avalanche prior to saturation. The direction of the changing field is then reversed and the process repeated, stopping just prior to the final avalanche that would close each particular subloop. The process ends when one encounters a subloop branch containing only a single avalanche, leaving the system in the demagnetized state. This process will be termed an "exact" demagnetization. As in the laboratory, to trace out the demagnetization curve itself, starting from the demagnetized state, one simple raises (or lowers) the field until the system saturates.

One may also start the simulation with all spins up and the field at positive infinity and then repeat the process above. This results in an identical demagnetization curve, except possibly for the first avalanches starting from the demagnetized state. When the termination of the exact demagnetization process ends in a multi-spin avalanche, the alternate starting direction may allow this multi-spin avalanche to be broken into smaller avalanches as the field is moving in the opposite direction. Hence the spins of the multi-spin avalanche may have different directions in the two demagnetized states. However, due to return-point memory, after raising or lowering the field past the first avalanche the demagnetization curves once again become identical. Other algorithms for demagnetization are possible, in particular one may perform an "inexact" demagnetization by simply reducing the maximum amplitude of the field by a given interval at each change of sweeping direction. For large enough intervals this results in few to many avalanches being left unflipped when the sweep direction is reversed in a given subloop branch. As the interval is reduced to zero, this algorithm then becomes equivalent, in the thermodynamic limit, to the process of exact demagnetization. However, as the number of avalanches in a given interval ΔH grows as one approaches the critical point, $H \to H_c^d$, for any finite ΔH the inexact demagnetization will blur out the critical point, changing both the demagnetized state as well as the scaling behavior of the demagnetization curve. For this reason only the "exact" algorithm was used when analyzing properties of the demagnetization curve.

4.2 Critical Transition

The demagnetization curve exhibits a similar transition to that found in the saturation loop as one tunes the system disorder R [104]. In Fig. 4.1 demagnetization curves are shown, with the saturation loop included as a reference, at three values of the disorder R. On the left, the disorder is below the critical disorder, resulting in a demagnetization curve with a finite jump in magnetization. As one approaches the

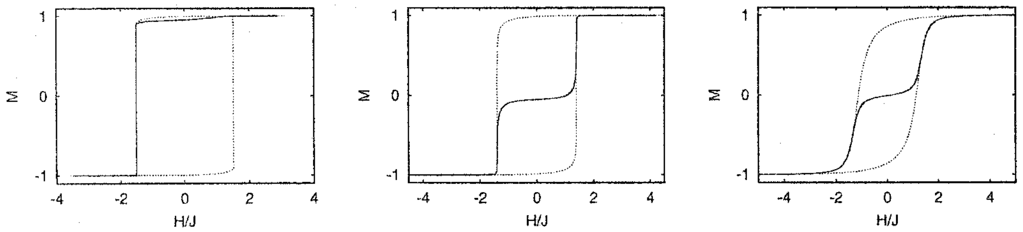

Figure 4.1: Demagnetization curves (solid lines) and saturation loops (dotted lines) for 100^3 systems at disorders $R = 2.0J$, $2.3J$, and $3.3J$ from left to right. For low disorder (left plot) a large jump in magnetization occurs, while for high disorder (right plot) the demagnetization curve looks smooth. A transition occurs in the intermediate disorders, at $R_c^d \approx 2.12$ in an infinite system, where the jump in magnetization becomes a point singularity in the slope (center plot).

critical disorder, the size of this jump reduces and vanishes at the critical disorder. The corresponding plot is shown in the center plot of Fig. 4.1. For disorders above the critical disorder, as depicted in the right plot of Fig. 4.1, the demagnetization curve has no large jump in magnetization, but instead looks smooth for large systems. In reality there is a succession of jumps corresponding to avalanches in the system, but these are small compared to the system size. Note that the large jump in magnetization present below the critical point, responsible for the asymmetry of the demagnetization curve, may occur upon sweeping the field either up or down, depending on the system's underlying configuration of random fields. This jump and its implications are further discussed in the context of subloops in Sec. 5.1.

4.3 Critical Scaling

Qualitatively, the critical transition found in the demagnetization curve behaves identically with that of the saturation loop. However, the details of the transition differ. In this section the differences will be analyzed by examining the universal scaling of quantities associated with the avalanches in the demagnetization curve, including the avalanche size distribution (Sec. 4.3.1) and avalanche correlation function (Sec. 4.3.2) plus finite-size scaling for the number of system-spanning avalanches (Sec. 4.3.3), sec-

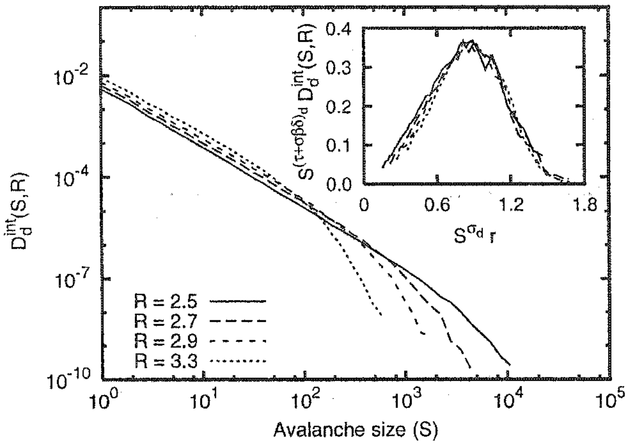

Figure 4.2: Integrated avalanche size distributions for 100^3 systems at disorders $R = 2.5J$, $2.7J$, $2.9J$, and $3.3J$ and averaged over 10, 5, 4, and 1 random seeds respectively. The scaling collapse is shown in the inset where $r = (R - R_c^d)/R$ with $R_c^d = 2.12J$. The critical exponents are $(\tau + \sigma\beta\delta)_d = 2.1$ and $1/\sigma_d = 4.1$.

ond moments of the avalanche size distribution (Sec. 4.3.4), and the jump in magnetization due to spanning avalanches (Sec. 4.3.5). A similar analysis has been performed on the saturation hysteresis loop [94].

4.3.1 Integrated Avalanche Size Distribution

The integrated avalanche size distribution $D_d^{\text{int}}(S)$ was measured along the demagnetization curve. Here integrated refers to the fact that avalanches along the entire demagnetization curve are included. Figure 4.2 displays the integrated avalanche size distributions obtained from simulations of a system with 100^3 spins for several values of the disorder R that are above the critical disorder R_c^d. Curves closer to the critical disorder display an increasing size cutoff, similar to the saturation loop behavior [94]. Thus, in analogy with the saturation loop, the avalanche size distribution is given the scaling form,

$$D_d^{\text{int}}(S, R) \sim S^{-(\tau+\sigma\beta\delta)_d} \mathcal{D}_d^{\text{int}}(S^{\sigma_d} r), \tag{4.1}$$

where $(\tau + \sigma\beta\delta)_d$ and σ_d are universal scaling exponents. The avalanche distributions were collapsed using this scaling ansatz and are shown in the inset of Fig. 4.2. The resulting exponents are shown in Table 5.1. The value of $(\tau + \sigma\beta\delta)_d$ was found to be slightly larger than its saturation loop counterpart (also listed in Table 5.1), although their error bars overlap slightly. On the other hand, the exponent governing the size cutoff, σ_d, was found to be the same. These values are consistent with the exponent relations derived in Sec. 7.2 and listed in Table 4.1. Also of interest is the universal scaling function itself, $\mathcal{D}_d^{\mathrm{int}}$, which turns out to be indistinguishable from the saturation loop scaling function $\bar{\mathcal{D}}_+^{(\mathrm{int})}$ [94] after a simple rescaling of the vertical axis.

4.3.2 Integrated Spin-Flip Correlation Function

The integrated spin-flip correlation function $G_d^{\mathrm{int}}(x)$ was also measured along the demagnetization curve for the same disorders as the avalanche size distribution and the results are shown in Fig. 4.3. Similar to the avalanche size distribution, as the disorder increases, the power-law cutoff length (or correlation length) decreases. Again taking the saturation loop as an analogy, one may write the scaling form for the correlation function as

$$G_d^{\mathrm{int}}(x, R) \sim x^{-(d+\beta_d/\nu_d)}\mathcal{G}_d^{\mathrm{int}}(xr^{\nu_d}). \tag{4.2}$$

The collapse resulting from this scaling ansatz is shown in the inset of Fig. 4.3 with the resulting exponents listed in Table 5.1. The power-law exponent $d+\beta_d/\nu_d$ was found to be slightly larger than for the saturation loop, although with overlapping error bars, whereas the correlation length exponent ν_d is the same as for the saturation loop. Both of these results are consistent with the exponent relations found in Table 4.1.

4.3.3 Number of Spanning Avalanches

The number of system-spanning avalanches $N_d^{\mathrm{int}}(L, R)$ was measured for a range of disorders and system sizes. The resulting curves are shown in Fig. 4.4. The scaling

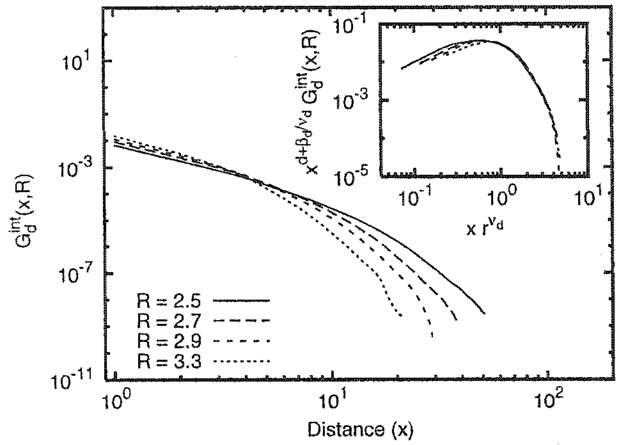

Figure 4.3: Integrated spin-flip correlation functions for 100^3 systems at disorders $R = 2.5J$, $2.7J$, $2.9J$, and $3.3J$ and averaged over 10, 5, 4, and 1 random seeds respectively. Curves are collapsed using $r = (R - R_c^d)/R$ with $R_c^d = 2.12J$, $d + \beta_d/\nu_d = 3.1$, and $\nu_d = 1.4$.

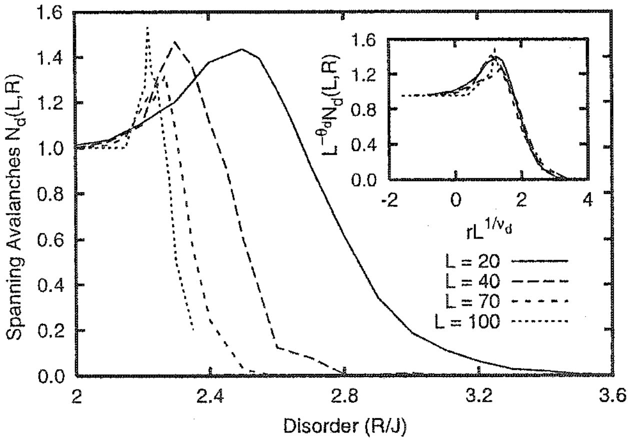

Figure 4.4: Number of system spanning avalanches for system sizes of 20^3, 40^3, 70^3, and 100^3 averaged over up to 40 random configurations. Curves are collapsed using $r = (R - R_c^d)/R$ with $R_c^d = 2.12J$, $\theta_d = 0.01$, and $1/\nu_d = 0.71$.

form for the number of spanning avalanches is given by,

$$N_d^{\text{int}}(L,R) \sim L^{\theta_d} \mathcal{N}_d^{\text{int}}(L^{1/\nu_d} r). \tag{4.3}$$

The result of collapsing the curves using this form is shown in the inset of Fig. 4.4 with the corresponding exponents listed in Table 5.1. As seen in the inset, the decay of the number of spanning avalanches for larger disorders collapse well. However, near the peak a very poor collapse is obtained. This is due in part to averaging the curves over too few configurations of random fields, particularly for the largest systems. However, this is currently unavoidable, due to the long simulation times required. For the same reason it was impractical to have a very small mesh size in sampling the R axis. Hence, the power-law exponent θ_d has been given a large error estimate, and could possibly vanish. Due to the inability to simulate large systems, again due to time constraints, it is not clear whether there is a diverging number of spanning avalanches at the critical point in three dimensions as $L \to \infty$. Note that a similar conclusion was drawn for the saturation loop in three dimensions [94], although it was possible to extract a very small value for θ (with $\theta = 0$ within its error bars). The value of ν_d was kept consistent with the other scaling collapses.

4.3.4 Second Moments of Integrated Avalanche Size Distribution

The second moments of the integrated avalanche size distribution $\langle S^2 \rangle_d^{\text{int}}(L,R)$ were also measured for the same range of disorders and system sizes as the spanning avalanches. The resulting curves are shown in Fig. 4.5. Using Eq. (4.1) one arrives at the scaling form

$$\langle S^2 \rangle_d^{\text{int}}(L,R) \sim L^{\rho_d} \mathcal{S}_d^{\text{int}}(L^{1/\nu_d} r) \tag{4.4}$$

where $\rho_d = -(\tau_d + \sigma_d \beta_d \delta_d - 3)/\sigma_d \nu_d$. The inset of Fig. 4.5 shows the collapse resulting from this form and the corresponding exponents are listed in Table 5.1. The value

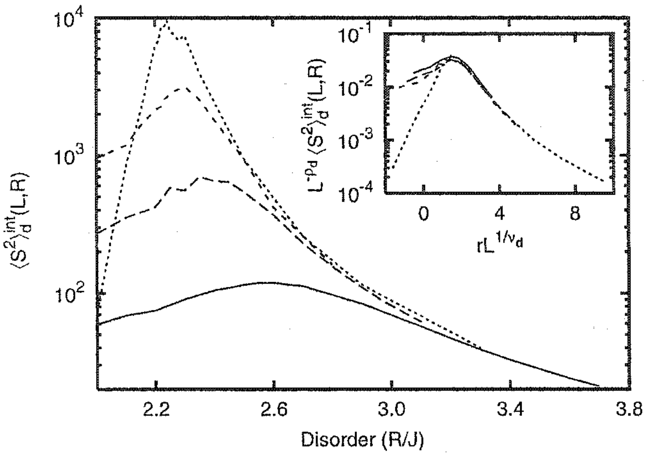

Figure 4.5: Second moments of the integrated avalanche size distribution for system sizes of 20^3, 40^3, 70^3, and 100^3 averaged over up to 40 random configurations. Curves are collapsed using $r = (R - R_c^d)/R$ with $R_c^d = 2.12J$, $\rho_d = 2.7$, and $1/\nu_d = 0.71$.

of ρ_d was found to be slightly smaller than expected from the relations of Table 4.1. However, within the error bars it remains consistent with those relations. As before, the value of ν_d was kept the same as in the other collapses.

4.3.5 Jump in Magnetization due to Spanning Avalanches

Finally, the jump in magnetization due to the spanning avalanches $\Delta M_d^{\rm int}(L, R)$ was measured for the same range of disorders and system sizes as above. The resulting curves are shown in Fig. 4.6. The scaling form for the jump in magnetization is

$$\Delta M_d^{\rm int}(L, R) \sim L^{-\beta_d/\nu_d} \Delta \mathcal{M}_d^{\rm int}(L^{1/\nu_d} r), \tag{4.5}$$

and the resulting collapse is shown in the inset of Fig. 4.6, again with the exponents listed in Table 5.1. As before, the value of ν_d was kept consistent with the other collapses. Moreover, although the power-law exponent of the correlation function also includes the factor β_d/ν_d, due to its small value one cannot reliably extract it from the dimension in the equation $d + \beta_d/\nu_d$ (other than noting that it must be small). Thus the value of β_d/ν_d was determined solely from this collapse of the jump in magnetization.

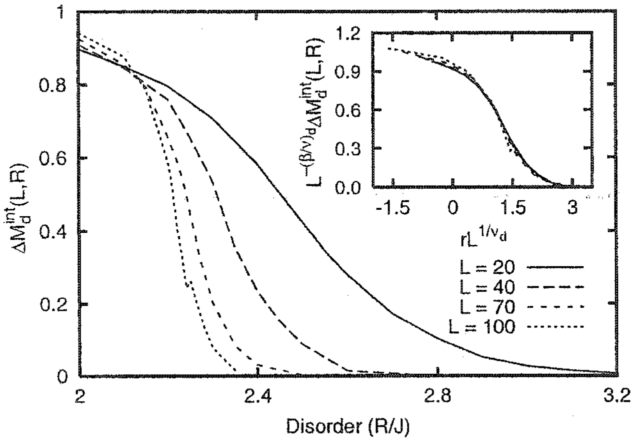

Figure 4.6: Size of the magnetic discontinuity ΔM_d^{int} due to system spanning avalanches for system sizes of 20^3, 40^3, 70^3, and 100^3 averaged over 400, 60, 80, and 10 random configurations respectively. Curves are collapsed using $r = (R - R_c^d)/R$ with $R_c^d = 2.12J$. The inset shows the collapse using the critical exponents $\beta_d/\nu_d = 0.03$ and $1/\nu_d = 0.71$.

4.3.6 Scaling Summary

For each quantity measured along the demagnetization curve, the resulting data collapses yielded exponents that were consistent with the relations listed in Table 4.1. One may note two types of relations therein. First, the exponents governing the cutoffs are the same as the saturation loop counterparts, indicating that the underlying cause of the transition is the same as for the saturation loop, namely the system's random disorder.

On the other hand, the power-law exponents were found to differ slightly, although with overlapping error bars, from the saturation loop counterparts. This difference is expressed in the correction factor $X' = \beta_l\delta_l/\nu_l - \beta_d\delta_d/\nu_d$ which, as estimated from the finite size scaling exponents, is $X' = -0.005 \pm 0.005$. The power-law exponents from the other two collapses also contain the correction factor, but due to relatively small system sizes, finite size effects do not allow one to reliably extract X'. While X' was found to be slightly negative, because of the large uncertainty in the critical exponents for both the saturation loop and demagnetization curve, one cannot rule

Table 4.1: Relations between exponents describing the critical subloop (subscript l), subloops (subscript f), and demagnetization curve (subscript d) scaling behaviors.

Relation	Source
$\tau_d + \sigma_d\beta_d\delta_d = \tau_l + \sigma_f = \tau_l + \sigma_l\beta_l\delta_l - \sigma_l\nu_l X'$	$D^{\text{int}}(S, R)$
$\beta_d/\nu_d = \beta_l/\nu_l - X'$	$G^{\text{int}}(x, R)$
$\sigma_d = \sigma_l$	$D^{\text{int}}(S, R)$
$\theta_d = \theta_l + X'$	$N(L, R)$
$\tau_d = \tau_l$	$D(S, R, H)$
$X' = (\beta_l\delta_l - \sigma_f/\sigma_l)/\nu_l = {}^{a}(\beta_l\delta_l - \beta_d\delta_d)/\nu_l$	

[a] From relations 1, 3, and 5.

out the possibility that it vanishes (as occurs on the Bethe lattice[1]). If such were the case then all the critical exponents would be identical for both the saturation loop and demagnetization curve.

Also noteworthy is the fact that to obtain the finite-size scaling collapses the critical disorder for the demagnetization curve $R_c^d = 2.12 \pm 0.04$ was smaller than the saturation loop, $R_c = 2.16 \pm 0.03$. Due to the small difference between the values, one cannot rule out the possibility that the two critical disorders are the same. On the other hand, the smaller value is consistent with a value of H_c^d (see Sec. 5.2.5) that appears to be slightly smaller than H_c for the saturation loop, although again with overlapping error bars.

---

[1] Reference [99] finds $\beta_d = \beta$ for the RFIM on the Bethe lattice. The exponent relations of Table 4.1 give $X' = 0$.

Chapter 5

Subloops

Considering the critical point found in the saturation loop and demagnetization curve of the RFIM, it seems reasonable to expect that minor loops or subloops of the saturation loop would also display critical behavior. A myriad of possible subloops and associated field histories may be conceived, however herein they will be constrained to be nested, concentric symmetric subloops. Such subloops are obtained in simulations by increasing the field from saturation up to a desired reversal point, labeled $(H_{\max}, M_{\max})$, and then decreased to the symmetric point, $(-H_{\max}, -M_{\max})$. The field is then increased again, up to the next subloop starting point, and the process is repeated. If the spacing between subloops is reduced to zero then one recovers the exact demagnetization of Sec. 4.1. However, unlike the demagnetization curve, subloops are relatively insensitive to the inter subloop spacing ΔM. Although a finite ΔM imparts a small horizontal shift to the center, the shape remains nearly the same. Thus, in simulations, a small but finite ΔM is used. Such a set of nested subloops provides a simple tool for probing the critical behavior inside the saturation loop as it "fills" the area, in the limit $\Delta M \to 0$ (with a notable exception to this filling found in the next section). The method of first-order reversal curves (FORCs) [105], a different approach to quantifying the behavior of subloops, uses a similar idea of filling the saturation loop with subloops, but with asymmetric ones.

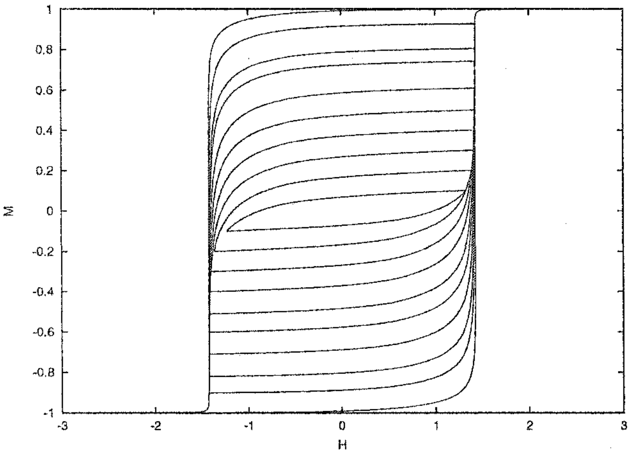

Figure 5.1: Concentric inner subloops above the critical disorder for a 240^3 system size. The saturation loop was run at a disorder of $R = 2.225J$ which is above the infinite system $R_c = 2.16J$. Subloops, on average, are spaced evenly in magnetization by $\Delta M = 0.1$ and appear similar to rescaled saturation loops at higher disorder as one moves further inward (to later histories).

5.1 Critical Transition

Measuring subloops of a saturation loop started with a disorder at or above the critical disorder results in a picture similar to that shown in Fig. 5.1. The saturation loop is relatively square although still smooth, but as one moves inwards to later histories the subloops begin to flatten out, reminiscent of a rescaled saturation loop at an effectively higher disorder. Indeed, pre-flipped spins not participating in a subloop may act as an added, possibly correlated "effective disorder." These pre-flipped spins are those that would have flipped as the field was increased above the upper reversal point of the subloop, or below the lower reversal point. Note that as the subloops are nested, the number of pre-flipped spins increases as one moves to deeper subloops.

To test this hypothesis, one may start the saturation loop at a disorder below the critical disorder R_c. If history does increase the effective disorder then one should be able to observe a transition from square loops to smooth loops as seen in the saturation curve. In Fig. 5.2 such a history is shown for a system with $R < R_c$. A transition from square to smooth loops is not evident. Instead of the field history producing a

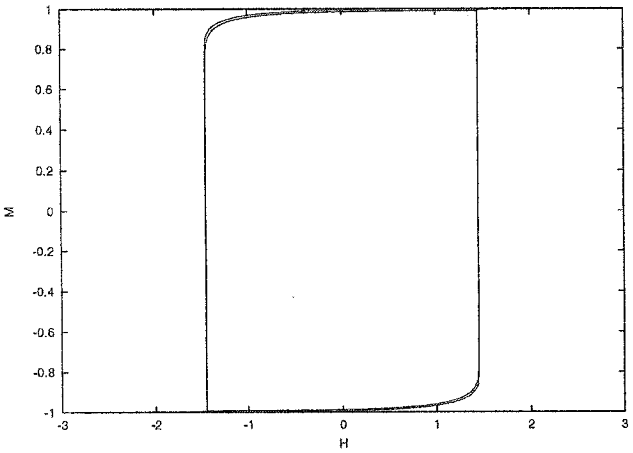

Figure 5.2: Concentric inner subloops below the critical disorder for a 240^3 system size. The saturation loop was run at a disorder of $R = 2.1J$ which is below the infinite system $R_c = 2.16J$. Only a few subloops are unique after which due to the large infinite avalanche below R_c, all later subloops are congruent.

set of subloops with an even spacing ΔM, after the first few subloops all later ones collapse onto a single "square" subloop. This subloop contains a single large system-spanning avalanche reminiscent of the jump in magnetization found in the saturation loop. A nonzero fraction of the system's spins are flipped in a single event. As one may not interrupt this avalanche to change the field direction, the states inside the irreducible subloop are not accessible through adiabatic histories that start from a saturated spin state. Thus it is impossible to tune the system through the phase transition [68; 100; 106], at least for the largest system sizes simulated ($L = 480^3$).

As the demagnetization curve is composed of the last avalanche of each subloop, this large spanning avalanche is the one responsible for the large jump in magnetization found in the demagnetization curve below R_c^d. As shown for the demagnetization curve, the size of this avalanche, and thus the size of the irreducible subloop, decreases as one moves closer to the critical disorder at which point it disappears. As noted in Ch. 4, it is possible that $R_c^d < R_c$. If such is the case, then for larger systems one would expect it to be possible to tune subloops through the critical transition at disorders with $R_c^d < R < R_c$.

5.2 Critical Scaling

Although a transition like that found in the saturation loop cannot be directly observed, its existence may be ascertained by examining the scaling behavior on one side of ("above") the critical point [5; 94]. Before this is possible, however, one must know what is meant by this critical point. Unlike the saturation loop and demagnetization curve, which had the system disorder as the tuning parameter, for the subloops one keeps the disorder fixed at the effective critical disorder itself. This effective critical disorder is system size dependent, so in the simulations the system is run at the effective critical disorder of the saturation loop $R_c(L)$ for the linear system size L with $R_c(L) \to R_c$ as $L \to \infty$. $R_c(L)$ is defined as the disorder at which the maximum number of system spanning avalanches in the saturation loop is observed [94].

As the reduced disorder is effectively zero and hence no longer relevant as a tuning parameter, a new tuning parameter to describe the history-induced scaling is defined[1], $f \equiv H_{\max_c} - H_{\max}$. This new parameter describes the distance from a subloop's maximum field $H_{\max}$ to the maximum field $H_{\max_c}$ of some critical subloop. Noting the critical behavior of the saturation loop and that the system is tuned to the critical disorder, one may be tempted to assume that the saturation loop *is* the critical subloop, as was suggested in an early analysis [68]. However, this is not the case. Instead, the critical subloop is found *inside* the saturation loop, in particular at the critical point of the demagnetization curve, (H_c^d, M_c^d, R_c^d), yielding $H_{\max_c} = H_c^d$. This is the point at which the last infinite avalanche appears in a subloop. In the thermodynamic limit, all subloops with $H_{\max} < H_{\max_c}$ are devoid of these infinite (system-spanning) avalanches.

Armed with this new tuning parameter, it now is possible to analyze the scaling of the various subloop quantities. In particular, scaling collapses of the loop-integrated avalanche size distribution (Sec. 5.2.1) and loop-integrated spin-flip correlation function (Sec. 5.2.2) will be examined along with the finite-size scaling of the second moments of the loop-integrated avalanche size distribution (Sec. 5.2.3) as well as the number of spanning avalanches (Sec. 5.2.4).

---

[1] Reference [68] used $\epsilon = (M_{\max_c} - M_{\max})/M_{\max}$ for the history "disorder". However, f provides a sounder scaling picture.

5.2.1 Integrated Avalanche Size Distribution

The loop-integrated avalanche size distribution, $D_f^{\text{int}}(S)$ was measured for subloops spaced by $\Delta M_{\text{max}} = 0.025$ in magnetization. Here, loop-integration refers to recording the avalanches along the entire subloop, including both the upper and lower portions. The resulting distributions are shown in Fig. 5.3. As with the saturation loop and demagnetization curve, the distributions display a decreasing cutoff size as one moves to deeper nested subloops, increasing the history-induced disorder. In analogy with Eqs. (3.2) and (4.1) the scaling of the loop-integrated avalanche size distribution is given by the form,

$$D_f^{\text{int}}(S, H_{\text{max}}) \sim S^{-(\tau+\sigma\beta\delta)_f} \mathcal{D}_f^{\text{int}}(S^{\sigma_f} f). \tag{5.1}$$

The collapse resulting from this scaling form is given in the inset of Fig. 5.3, with the resulting exponents listed in Table 5.1. Only subloops void of spanning avalanches were used in the collapse, in order to remove the effects of the finite system size, equal to 480^3 spins. The power-law exponent $(\tau + \sigma\beta\delta)_f$ was found to be identical, within error, to the value for the saturation loop. On the other hand σ_f, governing the size cutoff, was found to be much smaller than the saturation loop counterpart, with only a slight overlap in the error estimates. These results are consistent with the exponent relations found in Sec. 7.2 and listed in Table 4.1. Unlike in the case of demagnetization, the scaling function for the subloop avalanche size distribution is much broader than that of the saturation loop. This can be seen in the inset of Fig. 5.3 where the saturation loop scaling function is drawn with a dotted line.

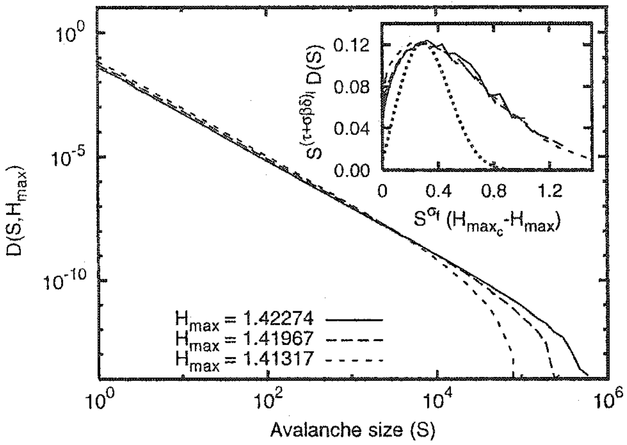

Figure 5.3: Integrated avalanche size distributions for 480^3 systems at $R = 2.198J$ and averaged over 20 random seeds. Curves are given for subloops starting at values of $H_{\text{max}} = 1.42274J$, $1.41967J$, and $1.41317J$. The inset contains a collapse of the three respective distributions. The dotted curve in the inset is the scaling function $\bar{\mathcal{D}}_{+}^{\text{int}}$ [94] for the saturation loop and has been scaled to be on the order of the subloop curves. The collapse yields the exponents $(\tau + \sigma\beta\delta)_f = 2.01 \pm 0.10$ and $1/\sigma_f = 2.3 \pm 0.5$ with $H_{\text{max}_c} = 1.427J$.

5.2.2 Integrated Spin-Flip Correlation Function

The loop-integrated spin-flip correlation function $G_f^{\text{int}}(x)$ was also measured for the same subloops as the avalanche size distribution. The resulting functions are shown in Fig. 5.4. Again one finds that as the history-induced disorder is increased, the correlation length decreases in the system. In analogy to Eqs. (3.3) and (4.2) one arrives at the scaling ansatz

$$G_f^{\text{int}}(x, H_{\text{max}}) \sim x^{-(d+\beta_f/\nu_f)} \mathcal{G}_f^{\text{int}}(x f^{\nu_f}) \qquad (5.2)$$

for the correlation function. Collapsing the correlation functions using this form results in the picture shown in the inset of Fig. 5.4 with the resulting exponent listed in Table 5.1. As for the avalanche size distribution, the power-law exponent $d+\beta_f/\nu_f$ is identical, within error, to the saturation loop exponent, whereas the correlation length exponent ν_f is found to be larger. These values are also consistent with the relations found in Table 4.1.

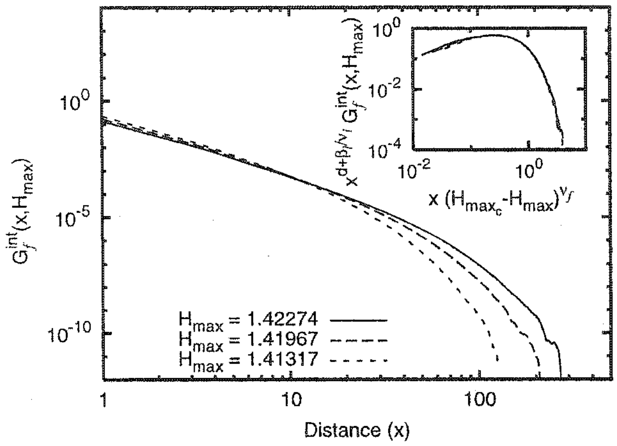

Figure 5.4: Integrated spin-flip correlation functions for 480^3 systems at $R = 2.198J$ and averaged over 20 random seeds. Curves are given for subloops starting at values of $H_{\text{max}} = 1.42274J$, $1.41967J$, and $1.41317J$. The inset contains a collapse of the three respective distributions, yielding $d + \beta_f/\nu_f = 3.0 \pm 0.2$ and $1/\nu_f = 1.28 \pm 0.40$ with $H_{\text{max}_c} = 1.427J$.

5.2.3 Second Moments of Integrated Avalanche Size Distribution

The second moment of the loop-integrated avalanche size distribution $\langle S^2\rangle_f^{\text{int}}(L, H_{\text{max}})$ was measured for subloops over a range of system sizes from $L = 80$ to $L = 480$. The second moments are normalized by the average avalanche size $\langle S\rangle$ and the resulting curves are shown in Fig. 5.5. They also behave similarly to the saturation loop, with a peak occurring near the critical point that increases in magnitude for larger systems. So, in analogy with Eqs. (3.6) and (4.4) one obtains the following scaling form for the second moments:

$$\langle S^2\rangle_f^{\text{int}}(L, H_{\text{max}}) \sim L^{\rho_f} \mathcal{S}_f^2(f L^{1/\nu_f}), \tag{5.3}$$

where $\rho_f = -(\tau_f + \sigma_f\beta_f\delta_f - 3)/\sigma_f\nu_f$. The collapse resulting from this scaling ansatz is shown in the inset of Fig. 5.5, with the resulting exponents given in Table 5.1. As each system was run at the effective critical disorder, $R_c(L)$, a system size dependent $H_{\text{max}_c}(L)$ was required in the collapse. Here, ρ_f was found to be slightly smaller than the saturation loop counterpart, although with overlapping error estimates. The

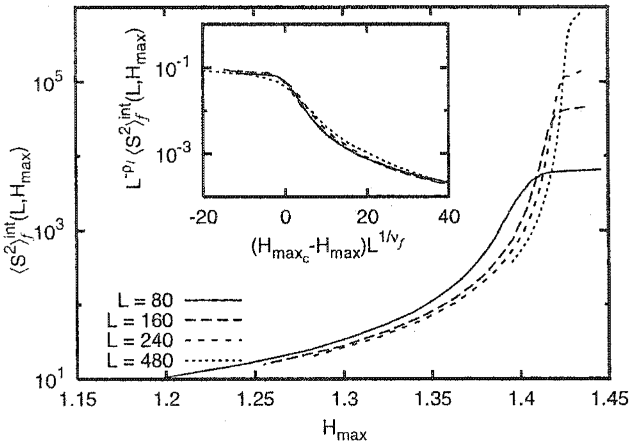

Figure 5.5: Second moments of the integrated avalanche size distribution for system sizes of 480^3, 240^3, 160^3, and 80^3 (right to left) averaged over 40, 40, 60, and 120 random seeds respectively. Each system was started at the effective critical disorder ($R = 2.198J$, $2.225J$, $2.250J$, and $2.308J$ respectively.) Second moments were taken on concentric subloops spaced $\Delta M = 0.025$ apart in magnetization. The inset contains a collapse of the four curves. Used in the collapse was $f = H_{\mathrm{max}_c}(L) - H_{\mathrm{max}}$ with $H_{\mathrm{max}_c}(L) = 1.427J$, $1.422J$, $1.417J$, and $1.405J$ respectively. The collapse yields the exponents $\rho_f = 2.6 \pm 0.40$ and $1/\nu_f = 1.28 \pm 0.40$.

value of ν_f was kept consistent with that obtained from the collapse of the correlation function.

5.2.4 Number of Spanning Avalanches

Lastly, the number of spanning avalanches in a subloop $N_f^{\mathrm{int}}(L, H_{\mathrm{max}})$ was measured on the same systems as the second moments of the avalanche size distribution. The resultant curves are shown in Fig. 5.6. The spanning avalanches do not exhibit such a close resemblance to the saturation loop as the other quantities did. Although they do show a peak that increases with system size, the maximum occurs at the saturation loop[2] $H_{\mathrm{max}} \to \infty$, instead of at the critical subloop $H_{\mathrm{max}} = H_{\mathrm{max}_c}$, as one would expect. Nevertheless, in accordance with Eqs. (3.4) and (4.3) one may try the

---

[2] Early assumptions [68] identifying the critical subloop with the saturation loop were partially based on this fact.

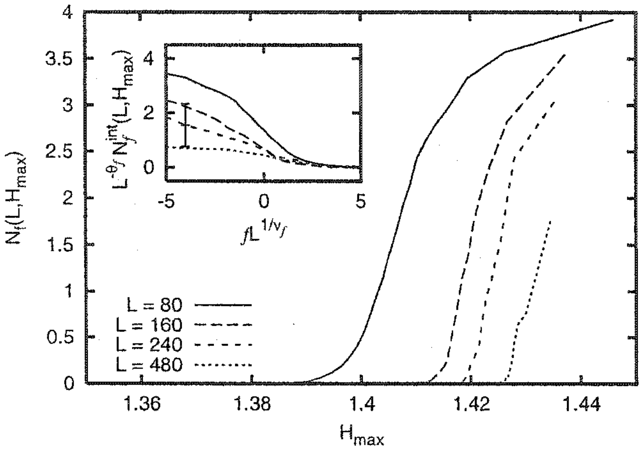

Figure 5.6: Number of spanning avalanches for system sizes of 480^3, 240^3, 160^3, and 80^3 (right to left) averaged over 40, 40, 60, and 120 random seeds respectively. Each system was started at the effective critical disorder ($R = 2.198J$, $2.225J$, $2.250J$, and $2.308J$ respectively.) Spanning avalanches were counted on concentric subloops spaced $\Delta M = 0.025$ apart in magnetization. The inset contains a collapse of the four curves with a maximum characteristic statistical error bar show for the $L = 240$ curve. Used in the collapse was $f = H_{\text{max}_c}(L) - H_{\text{max}}$ with $H_{\text{max}_c}(L) = 1.428J$, $1.422J$, $1.417J$, and $1.405J$ respectively. In the collapse exponents were set to the following values, $\theta_f = 0$ and $1/\nu_f = 1.28$.

following scaling form for the spanning avalanches:

$$N_f^{\text{int}}(L, H_{\text{max}}) \sim L^{\theta_f} \mathcal{N}_f^{\text{int}}(L^{1/\nu_f} f). \tag{5.4}$$

With this scaling form, the spanning avalanches do not collapse well, as shown in the inset of Fig. 5.6. The value of ν_f was set to that obtained from the previous collapses, and $\theta_f = 0$ was set. The curves collapse reasonably well below (inside) the critical subloop, that is for $f > 0$. Above the critical subloop, however, they do not collapse for any reasonable exponents, although if one allows $\theta_f < 0$ it is almost possible to obtain a collapse. It appears as though two overlapping behaviors are present, with a crossover regime from the desired behavior due to being near the critical subloop, given by θ_f, to a decay of "extra" spanning avalanches found in the saturation loop. The reversed separation of the curves by system size, with the largest system now having a smaller number of spanning avalanches, seems to indicate that the range in H_{max} over which this decay occurs decreases with increasing system size.

Unfortunately, it is unclear how to properly separate the behaviors in the crossover regime, but it will likely require much larger systems than currently are feasible to simulate. Adding to the difficulty, the numerical data is plagued by large statistical errors along the entire curve. An example error bar is shown for the 240^3 system in the inset of Fig. 5.6. The other error bars are typically smaller than this one. Although they do decrease as one moves to inward subloops, the relative error, given by $\sigma_N^2/\langle N \rangle$ where σ_N^2 is the variance of the number of spanning avalanches, does not decrease, due the limit $\langle N \rangle \to 0$.

5.2.5 Scaling Summary

For the collapses performed on quantities measured over concentric subloops, exponents were obtained that remained consistent with the relations of Table 4.1. Unlike the case of demagnetization, for the history-induced scaling the exponents governing the cutoffs, σ_f and ν_f were found to be different from their saturation and demagnetization counterparts. This indicates that the effective disorder, induced via the introduction of history, is different from the quenched, random disorder of the system. The effective disorder is introduced into the system by the pre-flipped spins that remain at the start of a given subloop. One would expect identical values for the cutoff exponents if these spins were randomly distributed about the lattice, thus preserving the uncorrelated, random nature of the system's disorder. However, this is not the case, as avalanches have left pockets of unflipped or pre-flipped spins with sizes related to the system's correlation length. So the difference in exponents is not surprising, as the history-disorder is likely a correlated disorder as opposed to the uncorrelated, quenched disorder. Furthermore, the scaling function for the history-induced scaling of the avalanche size distribution was found to be different from both that of the demagnetization curve and the saturation hysteresis loop, thus strengthening the case for two types of disorder. It should be noted that the exponents σ_f and ν_f respectively play similar roles as $\sigma_l \beta_l \delta_l$ and $\nu_l / \beta_l \delta_l$, as all four are physically connected to the scaling of a field value. Although the exponent values are slightly different, they are consistent, to within the quoted error bars. The possible ramifications of this fact are explored further in Sec. 7.2.3.

For the finite-size scaling collapses, the values of $H_{\text{max}_c}(L)$ required adjustment, due to the variations in the system disorders used. One may extrapolate the values to infinite system size via the power-law $(H_c^d - H_{\text{max}_c}(L)) \sim L^{-1/\nu_d}$ [107]. A data regression yields the best-fit value of $H_c^d = 1.4346 \pm 0.0013$, which is nearly identical to the value from the saturation loop, $H_c = 1.435 \pm 0.004$ [94]. The resulting best-fit power law is $1/\nu_d = 0.765 \pm 0.062$, which falls well within the estimated error for the exponent ν_d (see Table 5.1). It should be noted that the value of H_c for the saturation loop was obtained from collapses of avalanche size distributions binned in the field H from the largest simulated systems, which were an order of magnitude larger than those simulated here [94; 108].

Although the extrapolated estimate of H_c^d is not discernibly different from H_c, one cannot rule out the possibility that it does differ slightly but that the difference cannot be seen, due to the methods used to obtain the estimates of $H_{\text{max}_c}(L)$. The collapse for the correlation function and the second moments of the avalanche size distribution fix the required value of ν_f, as changing this exponent causes one function to have a refined collapse whereas the other becomes worse. As the power-law exponent for the correlation function is very insensitive to changes of L or $H_{\text{max}_c}(L)$, once a reasonable value of ν_f was determined one could refine the value of $H_{\text{max}_c}(L)$ to obtain the best collapse of the correlation function and avalanche size distribution. However, this was only possible for the two largest systems, due to the encroachment of spanning avalanches deep into the nested subloops. For the smaller systems, subloops that were void of spanning avalanches appeared to be out of the scaling regime and did not collapse well. Thus, their values of $H_{\text{max}_c}(L)$ were obtained by refining the collapse

Table 5.1: Universal critical exponents from scaling collapses in three dimensions for the demagnetization curve, history-induced disorder in subloops, and the random disorder of the saturation hysteresis loop. The exponent β/ν was not directly measured for the case of history-induced disorder.

Exponent	Demagnetization	History-Induced	Saturation[a]
$\tau + \sigma\beta\delta$	2.10 ± 0.05	2.01 ± 0.10	2.03 ± 0.03
$1/\sigma$	4.1 ± 0.4	2.3 ± 0.5	4.2 ± 0.3
$d + \beta/\nu$	3.1 ± 0.2	3.0 ± 0.2	3.07 ± 0.30
$1/\nu$	0.71 ± 0.10	1.28 ± 0.4	0.71 ± 0.09
θ	0.01 ± 0.01	0.0[b]	0.015 ± 0.015
ρ	2.7 ± 0.2	2.6 ± 0.4	2.90 ± 0.16
β/ν	0.03 ± 0.02		0.025 ± 0.020

---

[a] See Refs. [94; 104].

[b] The value of θ was set to zero in the collapse of spanning avalanches for subloops (see Sec. 5.2.4).

of the second moments of the avalanche size distribution. As these measurements are less reliable, they leave open the possibility that H_c^d could be different, and most likely less than H_c. If H_c^d were smaller then it would also reinforce the possibility that R_c^d is slightly smaller than R_c, as was hinted at in Sec. 4.3.6. To more suitably answer the question, larger systems would have to be analyzed.

Chapter 6

Long Range Forces

The previous chapters have focused on the case where long range forces are negligible. Now, however, J_{LR} in Eq. (3.1) is given a positive value to model the case where these anti-ferromagnetic forces, due to dipole fields for example, are important. To remain consistent with previous studies of the saturation loop for this case [90], the parameters are set as follows: $J_{LR} = 0.25J$ and $R = 1.8J$. These values were chosen because soft magnets are believed to lie below the critical disorder of the short range interface depinning model [92]. However, in general the critical behavior is the same over a large parameter range, although the onset avalanche as well as the size and slope of the linear portion will change with J_{LR} and $R < R_c$. Other materials, such as hard perpendicular thin films [70; 72], may also lie in this range.

6.1 Concentric, Symmetric Subloops

Concentric, symmetric subloops were measured for the RFIM with long range (LR) anti-ferromagnetic forces. The resulting magnetization curves are shown in Fig. 6.1. The subloops were spaced by $\Delta M = 0.1$ in magnetization. Unlike the case of Ch. 5, here the subloops all have a linear portion coincident with the saturation loop. As one moves inwards to smaller loops, the only change is a decrease in the length of the

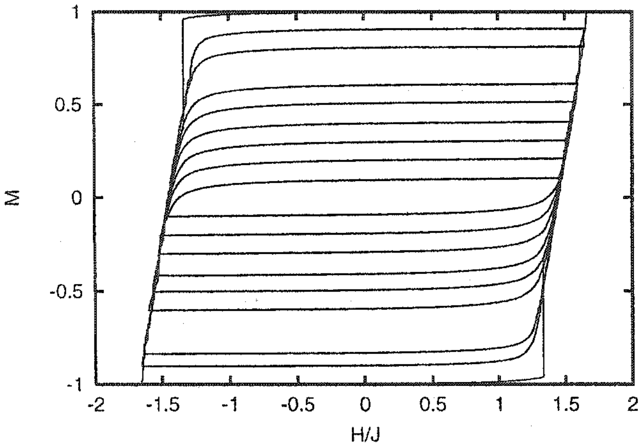

Figure 6.1: Saturation loop and concentric subloops with long range forces for a 100^3 system at a disorder of $R = 1.8J$ with $J_{LR} = 0.25J$. Subloops all display the same linear behavior, only differing in the length of the linear regime.

linear portion. Effectively, one is simply pushing a domain wall through the system, with smaller subloops corresponding to only moving it a shorter distance. For the smallest subloops, however, this picture breaks down, as the field is reversed before the domain wall depins across the entire system. Here one is relaxing the wall around the last pinned position. These subloops do show a behavior reminiscent of those in Ch. 5. However, due to the very small size of the subloops it is difficult to draw any clear conclusions.

The avalanche size distribution was measured for subloops, as shown in Fig. 6.1. The resulting curves for the linear portion of the subloops are shown in Fig. 6.2. To ensure that only the linear portion was included, the distribution was computed from data taken only above the coercive field, at which $M = 0$. As seen in Fig. 6.2, the curve for each of the subloops falls on the same power-law as the saturation loop without the need for any type of rescaling. This reaffirms that in the linear region one is simply pushing a domain wall through the system.

In Sec. 2.2 noise measurements on subloops for a soft ferromagnet were described. In that case, the avalanche size distributions were compiled over a region that was not strictly in the linear regime. Thus for a more direct comparison, it is also of interest to

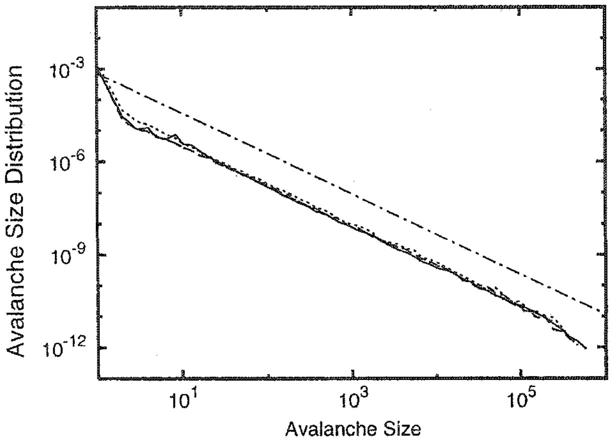

Figure 6.2: Avalanche size distributions with long range forces in a 240^3 system at a disorder of $R = 1.8J$ with $J_{LR} = 0.25J$ for subloops with $M_{max} = 0.82$, 0.72, and 0.53 averaged over 10 random configurations. The distributions were computed in the linear regime above the coercive field of each subloop. The curve for each subloop (dashed lines) fall upon the saturation loop curve (solid line) without performing any rescaling. The offset dash-dot line shows a power law of -1.3.

examine the integrated avalanche size distribution for the subloops of the RFIM with LR forces. In Fig. 6.3 the integrated avalanche size distribution is shown for subloops whose size is roughly equal to those measured in the experiment of Sec. 2.2 (Fig. 2.2). Unlike Fig. 2.2 the distributions for the subloops only fall on top of each other for large avalanches, although their slopes are the same for small avalanche sizes. The problem arises because the loop-integrated size distribution is the addition of two power-laws, one for the avalanches of the linear regime (with exponent -1.3) and another for the avalanches of the nonlinear regime (with exponent -1.7). The loop-integrated exponent is thus somewhat misleadingly named, as it really is connected to this latter size distribution, which involves integrating a subloop only up to the depinning field. However, a careful analysis still allows one to extract its value from the loop-integrated curves of Fig. 6.3. In particular, the vertical shift of the curves is due to the normalization of the distributions being dominated by the avalanches of the linear regime. The curves were normalized by the size of each subloop, proportional to the number of avalanches present. As each subloop has a different proportion of

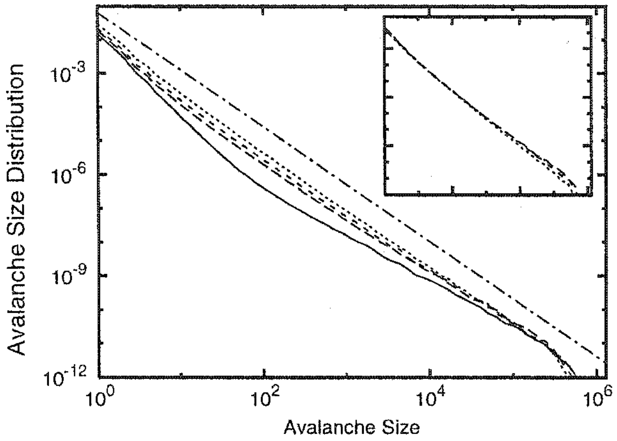

Figure 6.3: Integrated avalanche size distributions with long range forces for subloops of a 240^3 system at a disorder of $R = 1.8J$ with $J_{LR} = 0.25J$ averaged over 10 random configurations. The saturation loop curve is shown with a solid line. Distributions for subloops with $M_{max} = 0.82$, 0.72, and 0.53, which correspond roughly to the sizes of Fig. 2.2, are shown with dashed lines. The subloop distributions have been normalized by the subloop size, M_{max}. The subloop curves all have the same slope but only fall upon each other for large avalanche sizes. The offset dashed-dot line shows an integrated power law of -1.7. The inset contains a plot with identical ranges except showing only the subloop curves, now normalized by the relative size of the linear regime. Now the curves fall upon each other for small avalanche sizes without performing any rescaling.

the linear regime in relation to the nonlinear regime, this causes the distribution of avalanches in the nonlinear regime to be weighted differently in each subloop. The solution, then, is to include an additional normalization factor proportional to the relative size of the linear portion of each subloop. The result is seen in the inset of Fig. 6.3. The subloop distributions now fall on top of each other for small avalanche sizes, which correspond to the nonlinear regime. The integrated power law may be measured in this region. The point where the curves start to diverge, $S \approx 10^3$, denotes the beginning of the crossover regime between the power-laws for the distributions of the linear and nonlinear behaviors. Whereas the subloops' distributions do coincide with each other, the distribution for the saturation loop clearly does not. This arises due to the nucleation of a domain wall during the loop, as opposed to the reversal of the existing domain wall found in the subloops. The saturation loop distribution still has a slight similarity to those of the subloops, as it is the addition of two power-law distributions, one for the loop integrated exponent of the short range model, $\tau + \sigma\beta\delta = 2.03$, and one for the long range model's linear regime, $\tau = 1.3$. The former comes from integrating up to the onset avalanche (see Sec. 3.2) and the latter from the integration of the linear region occurring after the onset avalanche.

The measured loop-integrated power law, -1.7 ± 0.2, is larger in magnitude than the power law of the linear regime, -1.3. The same general trend of a larger loop-integrated power law is also found in the experimental noise measurement of Sec. 2.2. The actual value cannot be directly compared, however, as the experiment did not measure entire subloops and, more importantly, because the two systems lie in different universality classes. The experiment has effective infinite range ferromagnetic interactions along the domain walls (see Sec. 2.2), whereas the simulations only have short range ferromagnetic interactions. Adding stress to the experimental sample results in the latter short range forces [91], and so such an experiment would then be directly comparable to the model. Unfortunately, an experimental setup that

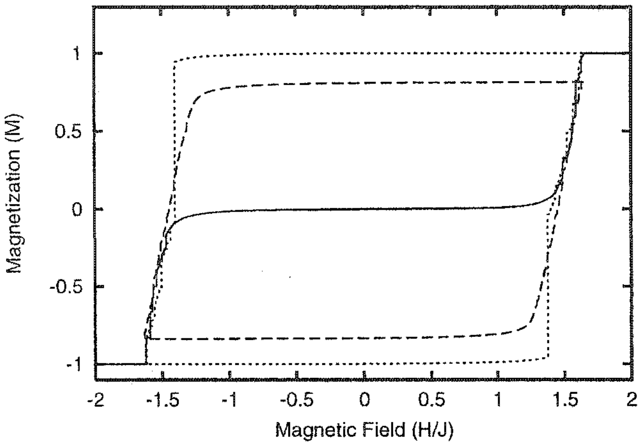

Figure 6.4: Demagnetization curve with long range forces for a 100^3 system at a disorder of $R = 1.8J$ with $J_{LR} = 0.25J$. The saturation loop (dotted line) and a subloop with $M_{max} = 0.8$ (dashed line) are shown for reference. The demagnetization curve exhibits two linear regions, both coincident with the respective upper or lower branch of the saturation loop and subloop.

included stress was unavailable.

6.2 Demagnetization Curve

The demagnetization algorithms of Sec. 4.1 may also be applied to the RFIM with LR forces. The key difference with LR forces is that the demagnetization curve drawn out as the field is increased or decreased from the demagnetized state is no longer identical to the curve composed of the last avalanches of each subloop traversed in the demagnetization process. This is due to the loss of exact return-point memory upon introduction of the LR anti-ferromagnetic fields [5]. However, one may still uniquely define the demagnetized state obtained from a particular algorithm, such as exact demagnetization, due to the deterministic behavior of the model. Performing a given field history will always result in the same final state for a particular realization of the quenched disorder.

A sample demagnetization curve for the RFIM with LR forces is shown in Fig. 6.4. It was obtained using an inexact demagnetization with step size $\Delta M \approx 0.005$. Similar

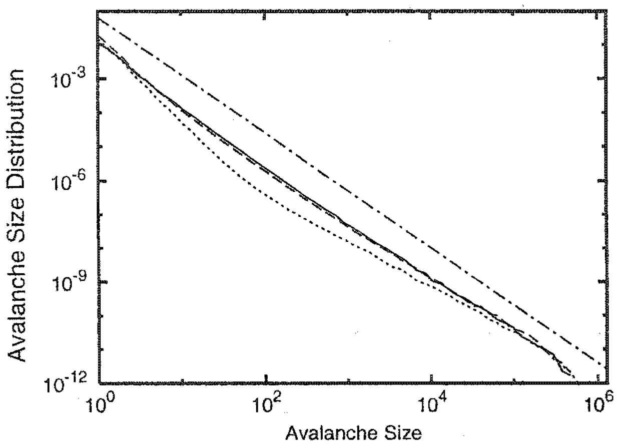

Figure 6.5: Integrated avalanche size distributions with long range forces for the demagnetization curve of a 240^3 system at a disorder of $R = 1.8J$ with $J_{LR} = 0.25J$ averaged over 10 random configurations. The demagnetization curve (solid line) appears nearly identical to the $M_{max} = 0.82$ curve (dashed line) while the saturation loop curve (dotted line) does not. The loop integrated power law of -1.7 is shown as an offset dash-dot line.

to the subloops, both the upper and lower portions of the demagnetization curve contain a linear region that coincides with the saturation loop. Effectively, in the demagnetization process one has pushed a domain wall back and forth until it lies in the center of the system. In tracing out the demagnetization curve one simply begins to move the domain wall again in the desired direction, thus again obtaining the linear magnetization behavior.

Noting the similarities between the subloops and saturation loop, one should expect that the avalanche size distribution will also behave similarly. In Fig. 6.5 the integrated avalanche size distribution is shown for the demagnetization curve as well as for the $M_{max} = 0.82$ subloop. Not surprisingly, the demagnetization and subloop curves appear roughly identical, reaffirming the behavior described above. As in Fig. 6.3, the saturation loop does not agree, due to the presence of the onset avalanche.

Chapter 7

Scaling Considerations

In previous analyses of the scaling of various saturation loop quantities, such as magnetization curves and their derivatives, it was shown that the correct scaling axes did not correspond to the pure tuning parameters r and h [108]. Instead, the scaling axes were "tilted" in the (r, h) plane, resulting in the effective scaling parameters $r' = r + Ah$ and $h' = h + Br$, where A and B were nonuniversal constants [94]. Adding history to the system, as done in Chs. 4 and 5 by performing concentric symmetric subloops, introduces a new history tuning parameter f into the system. In general, one may assume that the scaling axes in the (r, h, f) space are also 'tilted" *out of* the (r, h) plane, thus requiring new effective scaling axes. Hence, the new scaling parameters will be

$$r' \equiv r + A^h h + A^f f, \tag{7.1}$$

$$h' \equiv h + B^r r + B^f f, \tag{7.2}$$

$$f' \equiv f + C^h h + C^r r, \tag{7.3}$$

where the superscript on the nonuniversal constants denotes the pure parameter it multiplies. These parameters may also be given subscripts as described in Sec. 3.4. Note that, depending on the type of rotation out of the (r, h) plane, it is possible for A^f or B^f to vanish. In the following sections, the effect of these tilted scaling variables will be examined.

7.1 Corrections to Scaling

In a typical scaling collapse, as was performed in the previous chapters, the pure tuning parameter is used as part of the scaling variables, ignoring the tilted scaling axes of Eqs. (7.1-7.3). To justify this, the importance of the corrections to scaling caused by the tilted scaling axes must be examined. In the saturation loop, the tilted axes were found to be negligible for almost all the quantities that were measured, except for the magnetization curves and the binned avalanche size distribution [108]. In the latter case, the corrections were only important for relatively large values of the scaling parameter. Note that the magnetization curves and binned avalanche size distribution were not analyzed for the demagnetization curve or for the subloops.

As the demagnetization curve follows the same scaling forms as the saturation loop, and as the demagnetization exponents are identical, to within error bars, to the saturation loop, due to the very small (possibly zero) correction factor X', the arguments in Ref. [108] apply and the corrections to scaling are unimportant for the collapses performed in Ch. 4. For the history-induced disorder collapses, the situation is different. Whereas the exponents, namely those involved with the size cutoffs, are significantly different from their saturation loop counterparts, more importantly the manner in which the integration of the quantities was performed is different. For the saturation loop, most quantities were integrated over the entire range of H values, both above and below the critical point H_c. On the other hand, the subloops are integrated over only their finite range of H values, between $\pm H_{\mathrm{max}}$. In addition, as H_{max} usually occurs at the steepest point of the subloop (for $f > 0$) the integration covers only one side of the critical point. Due to these issues, a more careful look at the possible corrections from Eqs. (7.1-7.3) for the subloops is required.

Examining the avalanche size distribution first, one starts with the scaling form for the avalanche size distribution at given values of S, f, h, and r, now using the tilted scaling axes:

$$D_f(S,f,h,r) \sim S^{-\tau_f}\mathcal{D}_f(S^{(\sigma\beta\delta)_f}h', S^{\sigma_f}f', S^{\sigma_l}r'). \tag{7.4}$$

For the subloops, $r = r_d$ and $h = h_d$ but the subscripts will be suppressed to remove clutter. As the subloops are obtained at the critical disorder, or more accurately the effective critical disorder for the demagnetization curve, one lets $R \to R_c^d$. As the effective critical disorder is used, the finite-size effects will be ignored. Following the lead of Ref. [108], Eq. (7.4) therefore becomes

$$\begin{aligned} D_f(S,f,h,0) &\sim S^{-\tau_f}\mathcal{D}_f(S^{(\sigma\beta\delta)_f}h', S^{\sigma_f}f', S^{\sigma_l}(A_d^h h + A_d^f f)) \\ &\approx S^{-\tau_f}\big[\mathcal{D}_f(S^{(\sigma\beta\delta)_f}h', S^{\sigma_f}f', 0) \\ &\qquad + S^{\sigma_l}(A_d^h h + A_d^f f)\mathcal{D}_f^{(3)}(S^{(\sigma\beta\delta)_f}h', S^{\sigma_f}f', 0)\big], \end{aligned} \tag{7.5}$$

where $\mathcal{D}_f^{(3)}$ denotes the derivative of $\mathcal{D}_f$ with respect to the third variable. This gives the corrections for the binned avalanche size distribution for subloops. Whereas this quantity was not analyzed in Ch. 5, it is nevertheless worth examining the size of the corrections. In particular, the correction involving f will become important when $S^{\sigma_l}f > 1$ (equivalently $S > f^{-1/\sigma_l}$). In terms of the scaling variable, this is when $S^{\sigma_f}f > f^{-\sigma_f/\sigma_l}f = f^{1-\beta_d\delta_d}$. Here the exponent relations of Table 4.1 were used. Interestingly, the final expression is identical to that obtained for the saturation loop [108] with the substitution of f for h and demagnetization exponents for their saturation loop counterparts. For the values of f used in Ch. 5 ($f < 0.02$) this correction becomes on the order of one for values of the scaling variable $S^{\sigma_f}f \approx 10$. This is above the range used to collapse the data, and so the correction is negligible and will be dropped in the following.

The integrated avalanche size distribution, $D_f^{\text{int}}(S, f')$ is obtained by integrating the binned avalanche size distribution, given by Eq. (7.5), over the given subloop.

This means integrating over the field from $-H_{\max}$ to $+H_{\max}$:

$$\begin{aligned} D_f^{\mathrm{int}}(S,f') &= \int_{-H_{\max}}^{H_{\max}} dH D_f(S,f,h,0) \\ &\sim \int_{-H_{\max}}^{H_{\max}} dH S^{-\tau_f}\big[\mathcal{D}_f(S^{(\sigma\beta\delta)_f}h', S^{\sigma_f}f',0) \\ &\qquad + S^{\sigma_l}A_d^h h\mathcal{D}_f^{(3)}(S^{(\sigma\beta\delta)_f}h', S^{\sigma_f}f',0)\big]. \end{aligned} \tag{7.6}$$

Now $h' = h + B_d^f f$ as $r = 0$. Thus, one makes the substitution $u = S^{(\sigma\beta\delta)_f}(h + B_d^f f)$ in the above integral. This gives,

$$D_f^{\mathrm{int}}(S,f') \sim \int_{S^{(\sigma\beta\delta)_f}(-H_{\max}-H_{\max_c}+B_d^f f)}^{S^{(\sigma\beta\delta)_f}(H_{\max}-H_{\max_c}+B_d^f f)} du S^{-(\tau+\sigma\beta\delta)_f}\big[\mathcal{D}_f(u,S^{\sigma_f}f',0) + S^{\sigma_l-(\sigma\beta\delta)_f}A_d^h u\mathcal{D}_f^{(3)}(u,S^{\sigma_f}f',0)\big], \tag{7.7}$$

where $H_c^d = H_{\max_c}$ was used. Now, the upper limit starts at $H = H_{\max}$. Because subloops with $f > 0$ are of interest, this corresponds to the point where $h' = 0$. Therefore the upper limit vanishes[1]. Using this fact, the lower limit may also be rewritten as $S^{(\sigma\beta\delta)_f}(-2H_{\max})$. For the following analysis it is worth recasting the lower limit into yet another form. In particular, consider the case where instead of integrating all the way to $-H_{\max}$ one stops at some H_l. Then the lower limit becomes $S^{(\sigma\beta\delta)_f}(H_l - H_{\max})$.

Redefining the lower limit in this manner allows one to examine the behavior of the integral in Eq. (7.7) conditioned on how far along the loop one integrates. To that end, the integral in Eq. (7.7) is a function of two variables, $S^{(\sigma\beta\delta)_f}(H_l - H_{\max})$ and $S^{\sigma_f}f$. Hence one may write,

$$\begin{aligned} D_f^{\mathrm{int}}(S,f') &\sim S^{-(\tau+\sigma\beta\delta)_f}\big[\tilde{\mathcal{D}}_f(S^{(\sigma\beta\delta)_f}(H_l - H_{\max}), S^{\sigma_f}f) \\ &\qquad + S^{\sigma_l-(\sigma\beta\delta)_f}\tilde{\mathcal{D}}_f^{(3)}(S^{(\sigma\beta\delta)_f}(H_l - H_{\max}), S^{\sigma_f}f)\big]. \end{aligned} \tag{7.8}$$

Here $\tilde{\mathcal{D}}_f(x,y) \equiv \int_x^0 du\mathcal{D}_f(u,y,0)$. The convergence of this integral in Eq. (7.7) for any H_l is a reasonable assumption, as the scaling functions generally decay exponentially for large values of their parameters [108]. First, examining the behavior of the corrections arising from integrating over most or all of the loop, so that $H_l - H_{\mathrm{max}}$ is large, one expands the terms in Eq. (7.8) about $1/S^{(\sigma\beta\delta)_f}(H_l - H_{\mathrm{max}}) = 0$. This gives

---

[1] As an aside, this indicates that $B_d^f \approx 1.0$ although higher order corrections could change this slightly. Additionally, B_d^f has not been measured.

$$\begin{aligned} D_f^{\mathrm{int}}(S, f') \;\sim\; & S^{-(\tau+\sigma\beta\delta)_f}\Big[\tilde{\mathcal{D}}_f(-\infty, S^{\sigma_f} f) + \frac{S^{-(\sigma\beta\delta)_f}}{(H_l - H_{\mathrm{max}})}\tilde{\mathcal{D}}_f^{(1)}(-\infty, S^{\sigma_f} f) \\ & + S^{\sigma_l-(\sigma\beta\delta)_f}\Big(\tilde{\mathcal{D}}_f^{(3)}(-\infty, S^{\sigma_f} f) + \frac{S^{-(\sigma\beta\delta)_f}}{(H_l - H_{\mathrm{max}})}\tilde{\mathcal{D}}_f^{(3)(1)}(-\infty, S^{\sigma_f} f)\Big)\Big]. \quad (7.9) \end{aligned}$$

As $\sigma_l - (\sigma\beta\delta)_f < 0$, the third term is subdominant and only adds corrections for small avalanches. For the second and fourth term of Eq. (7.9) a similar analysis as for Eq. (7.5) is applied. Namely, one has $S^{-(\sigma\beta\delta)_f}(H_l - H_{\mathrm{max}})^{-1} > 1$ when $S < (H_l - H_{\mathrm{max}})^{-1/(\sigma\beta\delta)_f}$. Thus corrections are important for $S^{\sigma_f} f < (H_l - H_{\mathrm{max}})^{-1/(\beta\delta)_f} f$. Considering the integrated avalanche size distribution analyzed in Ch. 5, one has $H_l = -H_{\mathrm{max}}$. Combined with the values of f used and as $(\beta\delta)_f \approx 0.73$ this inequality will only be satisfied for very small values of the scaling parameter. This is not surprising, as small scaling parameters correspond to the small avalanches in the system because f does not vary widely in magnitude between subloops. By cutting off the integral slightly early, one is simply leaving out the smallest avalanches, which occur in the tail of the loops. All three corrections apply only for the range of small scaling parameters, thus confirming that the first term is dominant and that the scaling form used in Ch. 5, Eq. (5.1), is correct. However, the corrections may play a role in the poor collapse of the smallest subloop seen for the smallest values of the scaling parameter in the inset of Fig. 5.3.

The case in which one integrates Eq. (7.7) over only a small portion of the subloop is also informative. In this case H_l is close to H_{max}, so that $H_l - H_{\mathrm{max}}$ is small. Therefore, instead of expanding Eq. (7.8) about $1/S^{(\sigma\beta\delta)_f}(H_l - H_{\mathrm{max}}) = 0$, as done for the previous case, it is expanded about $S^{(\sigma\beta\delta)_f}(H_l - H_{\mathrm{max}}) = 0$. This gives,

$$\begin{aligned} D_f^{\mathrm{int}}(S, f') \;\sim\; & S^{-(\tau+\sigma\beta\delta)_f}[\tilde{\mathcal{D}}_f(0, S^{\sigma_f} f) + S^{(\sigma\beta\delta)_f}(H_l - H_{\mathrm{max}})\tilde{\mathcal{D}}_f^{(1)}(0, S^{\sigma_f} f) \\ & + S^{\sigma_l-(\sigma\beta\delta)_f}\tilde{\mathcal{D}}_f^{(3)}(0, S^{\sigma_f} f) + S^{\sigma_l}(H_l - H_{\mathrm{max}})\tilde{\mathcal{D}}_f^{(3)(1)}(0, S^{\sigma_f} f)]. (7.10) \end{aligned}$$

Now the first and third terms vanish. Taking the derivatives of the second and fourth terms simply returns one to the forms found in the integrand of Eq. (7.7). The factor $S^{(\sigma\beta\delta)_f}$ cancels with the leading power-law, resulting in a new leading power-law of S^{τ_f}. Together the result is,

$$\begin{aligned}
\lim_{H_l \to H_{\text{max}}} D_f^{\text{int}}(S, f') &\sim S^{\tau_f}[\mathcal{D}_f(S^{(\sigma\beta\delta)_f}(H_l - H_{\text{max}}), S^{\sigma_f} f', 0) \\
&\quad + S^{\sigma_l} A_d^h(H_l - H_{\text{max}})\mathcal{D}_f(S^{(\sigma\beta\delta)_f}(H_l - H_{\text{max}}), S^{\sigma_f} f', 0)] \\
&= S^{\tau_f}\mathcal{D}_f(0, S^{\sigma_f} f', 0). \qquad (7.11)
\end{aligned}$$

The above equation is the exact form, including corrections, for the binned avalanche size distribution, Eq. (7.5), at $h' = 0$. This makes sense, as for $H_l \to H_{\text{max}}$ one integrates over only a very small window near the start of the subloop. Hence one does not really have an integrated avalanche size distribution but a binned avalanche size distribution at $h' = 0$.

Calculating the corrections to scaling for the other quantities, like the integrated spin-flip correlation function and the finite size quantities, plays out in a similar manner to the avalanche size distribution. The only difference is that the size S is replaced by the distance x or system size L and the corresponding power law exponents are changed, and σ becomes $1/\nu$. The final result remains the same, however: the corrections are negligible except for very small x and L.

7.2 Exponent Relations

In the scaling analysis of the demagnetization curve (Ch. 4) and concentric, symmetric subloops (Ch. 5), three sets of critical exponents were introduced to describe the demagnetization curve, critical subloop, and history-induced disorder. These exponents are not all independent, however. In the following, relations governing their interdependencies will be derived, and it will be shown that all three sets depend only on the exponents of the critical subloop, together with one extra exponent which describes the history-induced disorder. It is worth noting that numerical simulations indicate that exponents of the critical subloop and the saturation loop are equal, to within error bars, although no exponent relations known so far impose the equality. Due to this apparent equality, in the discussions of Chs. 4 and 5 comparisons often refer to the exponents measured for the saturation loop.

The relations between the exponents will be derived first for history-induced scaling and then for the demagnetization curve. As many relations are repetitive, for quick reference all the independent relations are listed in Table 4.1.

7.2.1 Relations from History-Induced Scaling

To investigate the history-induced scaling, simulations were run for systems at the effective critical disorder, and the desired quantities were integrated over the entire subloop. Thus, the scaling forms depended only on the parameter f plus the measured quantity. Now, the critical subloop is found at the critical disorder with $f = 0$. At this point the tuning parameters vanish, so the quantities scale as simple power laws. Hence, to relate the history-induced scaling to the critical subloop one simply compares the two scaling forms as $f \to 0$ in the history-induced scaling form. For the loop integrated avalanche size distribution $D_f^{\text{int}}(S, f)$ this comparison appears as follows:

$$\begin{aligned} \lim_{f\to 0} D_f^{\text{int}}(S,f) \sim \lim_{f\to 0} S^{-(\tau+\sigma\beta\delta)_f}\mathcal{D}_f^{\text{int}}(S^{\sigma_f} f) &\sim S^{-(\tau+\sigma\beta\delta)_f} \\ &\sim S^{-(\tau+\sigma\beta\delta)_l}. \end{aligned} \tag{7.12}$$

From this one obtains the relation $(\tau + \sigma\beta\delta)_f = (\tau + \sigma\beta\delta)_l$. An argument similar to that used in Eq. (7.12) may be applied to the other history-induced scaling forms. This results in the relations $\beta_f/\nu_f = \beta_l/\nu_l$ from the correlation function, $\theta_f = \theta_l$ from the number of spanning avalanches, and $\rho_f = \rho_l$ from the second moments of the avalanche size distribution. The last relation may be simplified to the form

$\sigma_f \nu_f = \sigma_l \nu_l$.

7.2.2 Relations from Demagnetization Curve

The demagnetization curve is not as simply related to the critical subloop as the history-induced scaling. However, a careful observation allows one to connect the demagnetization curve with the history-induced scaling of the subloops. That is done by realizing that the demagnetization curve itself is composed of the last avalanche along the concentric subloops traced out during the demagnetization process. This assumes that the demagnetization is exact, as defined in Ch. 4, and that the system exhibits return-point memory. The second observation is that for $f > 0$ subloops are steepest at their endpoints, where $h' = 0$. Hence, one may construct the scaling forms for the demagnetization curve, as at $h' = 0$ the forms for the history-induced scaling of the subloops and the demagnetization curve must be identical.

For the avalanche size distribution this construction appears as follows. First one equates the two scaling forms at $h' = 0$:

$$D_d(S, H, R) \sim D(S, H, R, H_{\max})|_{h'=0}, \tag{7.13}$$

where the left-hand side is the scaling form for the demagnetization curve and the right-hand side is the general scaling form for the avalanche size distribution at the field H along the subloop with maximum field $H_{\max}$. This may be written equivalently as

$$S^{-\tau_d}\mathcal{D}_d(S^{\sigma_d\beta_d\delta_d}h'_d, S^{\sigma_d}r) \sim S^{-\tau_l}\mathcal{D}_l(0, S^{\sigma_l}r, S^{\sigma_f}f), \tag{7.14}$$

where $h'_d = h_d + B^r_d r$ and h_d implies the use of H^d_c instead of H_c. Notice that from Eq. (7.1), $h' = 0$ implies $f = -(h_d + B^r_d r)/B^f_d$, so that both sides have the same functional dependence. At this point, the form for the avalanche size distribution at field H has been obtained, and one may read off the exponent relations $\tau_d = \tau_l$, $B^r_d = B^r_l$, $\sigma_d\beta_d\delta_d = \sigma_f$, and $\sigma_d = \sigma_l$.

The integrated avalanche size distribution for the demagnetization curve is obtained by now integrating over the field h'_d in Eq. (7.14). This is equivalent to integrating over f on the right hand side of Eq. (7.14) and yields,

$$\begin{aligned} D_d^{\text{int}}(S,R) \sim \int dh'_d S^{-\tau_d} \mathcal{D}_d(S^{\sigma_d\beta_d\delta_d} h'_d, S^{\sigma_d} r) &\sim \int_0^{H_{\text{max}_c}} df\, S^{-\tau_l} \mathcal{D}_l(0, S^{\sigma_l} r, S^{\sigma_f} f) \\ S^{-(\tau_d+\sigma_d\beta_d\delta_d)} \mathcal{D}_d^{\text{int}}(S^{\sigma_d} r) &\sim S^{-(\tau_l+\sigma_f)} \mathcal{D}_l^{\text{int}}(S^{\sigma_l} r). \end{aligned} \tag{7.15}$$

In performing the integration only on one side of the critical point, where Eq. (7.13) holds, it is assumed that the scaling behavior on the opposite side, $f < 0$ is identical. From Eq. (7.15) one may read off several more exponent relations. However, none are independent of those already found from Eq. (7.14).

The other quantities measured for the demagnetization curve may have a similar procedure applied to them. It is instructive to examine the spin-flip correlation function in particular. Repeating the steps given in Eqs. (7.13) and (7.14) one obtains,

$$G_d(x,H,R) \sim G(x,H,R,H_{\text{max}})|_{h'=0}, \tag{7.16}$$

$$x^{-(d-2+\eta_d)} \mathcal{G}_d(x/\xi_d(r,h)) \sim x^{-(d-2+\eta_l)} \mathcal{G}_l(x/\xi_l(0, r^{-\sigma_l/\sigma_f} f)), \tag{7.17}$$

where the correlation length scales as $\xi_l(r,h,f) \sim r^{-\nu_l} \mathcal{Y}(h'/r^{\beta_l\delta_l}, r^{-\sigma_l/\sigma_f} f)$. Then integrating as in Eq. (7.15) to find G_d^{int} gives

$$\begin{aligned} &G_d^{\text{int}}(x,R) \sim \\ &\int dh'_d x^{-(d-2+\eta_d)} \mathcal{G}_d(x r^{\nu_d}/\mathcal{Y}(h'_d/r^{\beta_d\delta_d}) \sim \int_0^{H_{\text{max}_c}} df\, S^{-(d-2+\eta_l)} \mathcal{G}_l(x r^{\nu_l}/\mathcal{Y}(0, r^{-\sigma_l/\sigma_f})) \\ &x^{-(d-2+\eta_d+\beta_d\delta_d/\nu_d)} \mathcal{G}_d^{\text{int}}(x r^{\nu_d}) \sim x^{-(d-2+\eta_l+1/\nu_f)} \mathcal{G}_l^{\text{int}}(x r^{\nu_l}). \end{aligned} \tag{7.18}$$

From Eq. (7.16) one finds $\eta_l = \eta_d$ and from Eq. (7.18) the relations $\nu_l = \nu_d$ and $\beta_d\delta_d/\nu_d = 1/\nu_f$ are obtained.

Using the exponent relation $(2-\eta)\nu = \beta\delta - \beta$ (see Ref. [9]) the power-law for the demagnetization curve correlation function may be simplified to

$$-(d + \beta_d/\nu_d) = -(d + \beta_l/\nu_l - \beta_l\delta_l/\nu_l + \beta_d\delta_d/\nu_d).$$

From this form it is clear that the value of β_d/ν_d may be expressed by the corresponding loop exponent plus a correction term, giving $\beta_d/\nu_d = \beta_l/\nu_l - X'$, where the correction factor is $X' = \beta_l\delta_l/\nu_l - \beta_d\delta_d/\nu_d$. In fact, it is possible to express all the demagnetization quantities as the corresponding critical subloop exponent plus a function of the critical subloop exponents times X'. The appropriate relations in Table 4.1 thus are expressed using X'.

7.2.3 Unconstrained Exponents

At this point, all independent exponent relations have been determined from the examination of the history-induced and demagnetization scaling forms' relation to the critical subloop. Assuming that the exponent relations determined for the saturation loop [9] also apply to the critical subloop, the critical subloop contains four independent exponents. In the above analysis, none of these have been constrained. The exponents for the history-induced scaling were related to the critical subloop and left one new exponent unconstrained. One does have a choice of which exponent to denote as the "new" one, and due to the ease of measurement of the avalanche size distribution, σ_f was chosen. From the results of the previous paragraph one finds that all the demagnetization curve exponents are constrained by the critical subloop exponents and X'. Noting the relation $\beta_d\delta_d = \sigma_f/\sigma_l$, which may be obtained from the first, third, and fifth equations of Table 4.1, it is clear that $X' = (\beta_l\delta_l - \sigma_f/\sigma_l)/\sigma_l$ depends only on the critical subloop exponents plus the history induced exponent σ_f. Thus there are no new exponents from the demagnetization curve. Furthermore, the value of X' measured in the collapses of Ch. 4, although small, is still consistent with zero. If X' does vanish then one would have the additional relation $\sigma_f = \sigma_l\beta_l\delta_l$, and there would be no new exponents. The measured exponents, although slightly different, do have overlapping error bars and so are consistent with this relation. Physically the relation makes sense, as both exponents are used in connection with the tuning of a field value. It should be noted, however, that the underlying field values have very different meanings. As an example, the field H, connected to $\sigma_l \beta_l \delta_l$, is used in describing the binned avalanche size distribution at that particular field. On the other hand, σ_f is connected to the field H_{max}, which describes quantities that have been integrated over the entire range of H fields for a given subloop.

Chapter 8

Introduction to Population Biology

As mentioned in Ch. 1 there has been a limited focus on the growth of bacteria in inhomogeneous or disordered environments. Typically, inhomogeneity of the growth falls into either disordered growth with spatially random growth rates or an "oasis" problem, where a favorable region for growth is surrounded by a "desert" of negative growth rates. The latter case has been analyzed and found to exhibit an extinction transition as the convection velocity increases [109]. Essentially, the droplet of bacteria is blown, or forced, off the oasis. Numerical simulations have successfully tested this transition in two dimensions [110]. The transition has also been experimentally tested in one dimension [111]. The experimental setup consisted of a channel illuminated with UV light and covered by a small shield which provided an oasis by preventing the death of the bacteria via the UV light. Such a system may model blood flow past a localized infection [111]. A qualitatively similar extinction transition was found and compared with one dimensional simulations [111]. Another, earlier, experiment used a different system geometry: a rotating petri dish. In this case a sector of the dish was shielded from UV light to provide an oasis that had an effective convection velocity that increased with distance from the center. This resulted in similar qualitative behavior, in that past a certain velocity the bacteria could no longer keep up with the moving oasis [112]. The predictions for the extinction transition were reanalyzed for this wedge geometry and found to no longer be simply related to the stationary system [113].

A second way of introducing inhomogeneity into a system is through the inclusion of spatial randomness. This may occur in growth rates [114], diffusion constants, or even convection velocities (modeling turbulence) [115]. Little work in the field of biology has examined such situations. However, the underlying principles are connected to a wide range of other areas, as will be described further below. The use of a reaction-diffusion equation to model the behavior of bacteria makes the connections possible. Whereas in general one could have a very complicated reaction-diffusion equation involving a large number of species and diffusion constants [7], for simplicity the analysis following in Chs. 9 and 10 will examine the spreading of a single species in the highly advective regime of a spatially inhomogeneous growth environment. The appropriate equation takes the form

$$\partial_t c(\vec{x},t) = D\nabla^2 c(\vec{x},t) - \vec{v}\cdot\nabla c(\vec{x},t) + [a + U(\vec{x})]c(\vec{x},t) - bc^2(\vec{x},t), \qquad (8.1)$$

where $c(\vec{x},t)$ is the concentration at position $\vec{x}$ and time t. The first term on the right hand side of Eq. (8.1) gives diffusion, the second term provides a uniform advection, and the last two terms provide Fisher-type growth and death terms with spatially random growth rates, $U(\vec{x})$. The term "Fisher" comes from a particular limit of Eq. (8.1). For $v = 0$, $U(\vec{x}) = 0$, $a = b$, and one spatial dimension, the so-called Fisher equation is obtained [116].This equation is also commonly known as the KPP equation [117]. The Fisher equation has been widely used in modeling population growth in homogeneous environments [7]. The growth term $ac(\vec{x},t)$ produces exponential growth, which is cut off by the death term $bc^2(\vec{x},t)$ at the system's carrying capacity a/b. The equation allows traveling-wave solutions, such as shown in Fig. 8.1, which are termed Fisher waves. The velocity of propagation is dependent on the initial condition, but has a minimum, termed the Fisher velocity $v_F = 2(aD)^{1/2}$. This minimum velocity occurs when the initial condition decays faster than exponentially

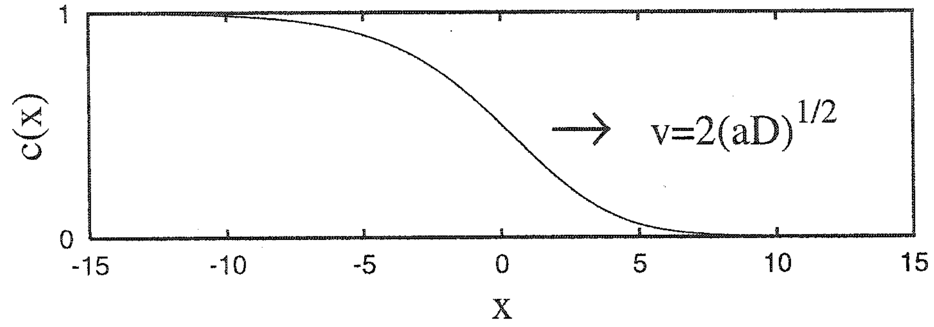

Figure 8.1: Fisher wave in one dimension with $a/b = 1$. The wave travels to the right at the Fisher velocity $v_F = 2(aD)^{1/2}$.

for large distances [7]. An equation similar to Eq. (8.1) may be used to model the wave front in a chemical reaction. Interestingly, by including internal noise in the system through a Langevin approach, two-dimensional simulations of the resulting wave front found propagation speeds up to 25% faster than the minimum Fisher velocity. This occurred even though the initial conditions were consistent with the minimum velocity absent any randomness [118].

Inspired by the problem of vortex pinning in superconductors [119], which obeys an equation similar to Eq. (8.1), a renormalization-group approach was used in examining the behavior of Eq. (8.1). In particular the behavior about both the unstable $c(\vec{x}) = 0$ solution and the stable $c(\vec{x}) = a/b$ solution was included [114]. For the former case, one may assume that $c(\vec{x}, t)$ is small enough that the nonlinear term in Eq. (8.1) may be neglected. The disorder averaged concentration profile is then predicted to have super-diffusive growth in the directions perpendicular to the convection velocity, with a width proportional to t^α, with $\alpha = 2/3$ in two dimensions [114]. In Ch. 10 this prediction will be tested numerically, along with the effects of including the nonlinear death term, which initial simulations have shown lead to isotropic spreading for short times [110].

8.1 Large Velocity Simplification

First however, it is worth examining a simplification of Eq. (8.1) proposed in Ref. [114] that will be examined in more detail in Ch. 9. In particular, the simplification examines the case of linear growth with convection so strong that the population is delocalized. This means that the convection velocity is large enough that even a population residing in the most favorable area for growth will be "blown off" of that region, leaving no concentration behind. In terms of the parameters, one must have $v \gg D/\xi_0$, where ξ_0 is the localization length of the fastest growing mode in the system [114]. The substitution,

$$c(x, \vec{r}_\perp, t) = \frac{1}{\sqrt{4\pi D t}} exp\left(at - \frac{(x-vt)^2}{4Dt}\right) W(x, \vec{r}_\perp), \tag{8.2}$$

assumes that the concentration is given by exponential growth plus normal diffusion in the x direction, which is also taken to be the direction of v, with the directions perpendicular to v denoted as $\vec{r}_\perp$ [114]. Inserting Eq. (8.2) in Eq. (8.1) and taking the limit of large x and t, the following simplified equation is obtained:

$$v\partial_x W(x, \vec{r}_\perp) = D\nabla_\perp^2 W(x, \vec{r}_\perp) + U(x, \vec{r}_\perp) W(x, \vec{r}_\perp). \tag{8.3}$$

Here, $W(x, \vec{r}_\perp)$ describes the behavior of the concentration profile in the directions perpendicular to the convection velocity $\vec{r}_\perp$ a distance x from the initial condition, which is taken to be a Dirac delta function [114].

If one considers the coordinate x as playing the role of time, as Eq. (8.3) is really looking at the concentration cross section at position $x = vt$, then Eq. (8.3) takes the form of an imaginary-time Schrödinger equation with a potential dependent on both the space and time variables. This equation has been studied extensively [120] and the width of the profile W is predicted to grow with a super-diffusive exponent equal to 2/3 for (1+1) dimensions [121]. This should be expected, as this case coincides with the linear, two-dimensional spreading case of Eq. (8.1) which has an identical prediction.

One important concept arising for the simplified equation, although also present in Eq. (8.1), is the idea of optimal paths. For a particular position at the "time" x, the local bacteria will have traveled along a path of optimal growth rates. The relative concentration strength will depend on which of these optimal paths traversed the most favorable growth rates, and the strongest will exponentially dominate the other possible paths [114]. A similar idea may be found in the field of directed polymers [120], which are described by an equation similar to Eq. (8.3).

Chapter 9

One-Dimensional Spreading

In Sec. 8.1 a simplification of the full reaction-diffusion equation, Eq. (8.1), in the limit of large velocities and long times was introduced. By studying this simplified equation, one may obtain a better understanding of the behavior of the full equation. The simplified equation, Eq. (8.3), separates the direction parallel to the convection velocity from the directions perpendicular to that velocity. This parallel direction behaves like a temporal variable in the simplified equation, relating to the fact that for a given value of the parallel direction, x, the simplified equation is describing the perpendicular cross section at the time $t = x/v$. In light of this connection, Eq. (8.3) will be transformed into a more familiar form by renaming the variables $x \to t$ and $\vec{r}_\perp \to \vec{x}$, giving

$$v\partial_t W(\vec{x}, t) = D\nabla^2 W(\vec{x}, t) + U(\vec{x}, t)W(\vec{x}, t). \tag{9.1}$$

In particular, one is interested in the situation where an initial concentration profile $W(0, \vec{x})$ is given and whose evolution is described by Eq. (9.1) for times $t > 0$. To investigate this case, the behavior of Eq. (9.1) will first be examined using perturbation theory (Sec. 9.1) and then the one-dimensional case will be examined numerically (Sec. 9.2).

9.1 Perturbation Expansion

Due to the variation in environmental growth factors such as food, modeled by the random growth term $U(\vec{x},t)$ in Eq. (9.1), the average long-time behavior of initial concentration profiles evolving under Eq. (9.1) will not exhibit simple diffusion. However, for short times, before the random term has been explored, the system will exhibit simple diffusion. Thus one would like to obtain a crossover time between these two behaviors. To this end, a simple perturbation expansion of Eq. (9.1) may be performed.

In the spirit of Ref. [122] one first applies a Fourier-Laplace transform to Eq. (9.1). This transform is defined as

$$\widehat{W}(\vec{k},\omega) = \int_0^\infty dt e^{-\omega t}\widetilde{W}(\vec{k},t), \qquad \widetilde{W}(\vec{k},t) = \int_{-\infty}^\infty d^d x e^{-i\vec{k}\cdot\vec{x}} W(\vec{x},t), \tag{9.2}$$

where $\widetilde{W}(k,t)$ represents the Fourier transformed $W(x,t)$ and $\widehat{W}(k,\omega)$ is the full Fourier-Laplace transformed $W(x,t)$. Applying the transformation of Eq. (9.2) to the simplified equation, Eq. (9.1), gives

$$\widehat{W}(k,\omega) = vG_0(k,\omega)\widetilde{W}(k,0) + G_0(k,\omega)\int_{-\infty}^\infty \frac{d^d q}{(2\pi)^d}\int_0^\infty dt e^{-\omega t}\widetilde{U}(q,t)\widetilde{W}(k-q,t), \tag{9.3}$$

where $G_0(k,\omega) = (v\omega + Dk^2)^{-1}$ is the free propagator. To obtain $\widehat{W}(k,\omega)$ on the right hand side of Eq. (9.3), the second term is rewritten using,

$$\widetilde{U}(q,t)\widetilde{W}(k-q,t) = \int_{a-i\infty}^{a+i\infty} \frac{d\Omega_a}{2\pi i}\widehat{U}(q,\Omega_a)\int_{b-i\infty}^{b+i\infty} \frac{d\Omega_b}{2\pi i}\widehat{W}(k-q,\Omega_b), \tag{9.4}$$

where the Bromwich integral giving the inverse Laplace transform was used. Note that $\widetilde{U}(q,t)$ has no exponential growth, so any $a > 0$ is sufficient. However, as the disorder causes enhanced growth [114], b must be chosen greater than the growth constant associated with $\widetilde{W}(k-q,t)$. Finally, combining Eqs. (9.3) and (9.4) gives

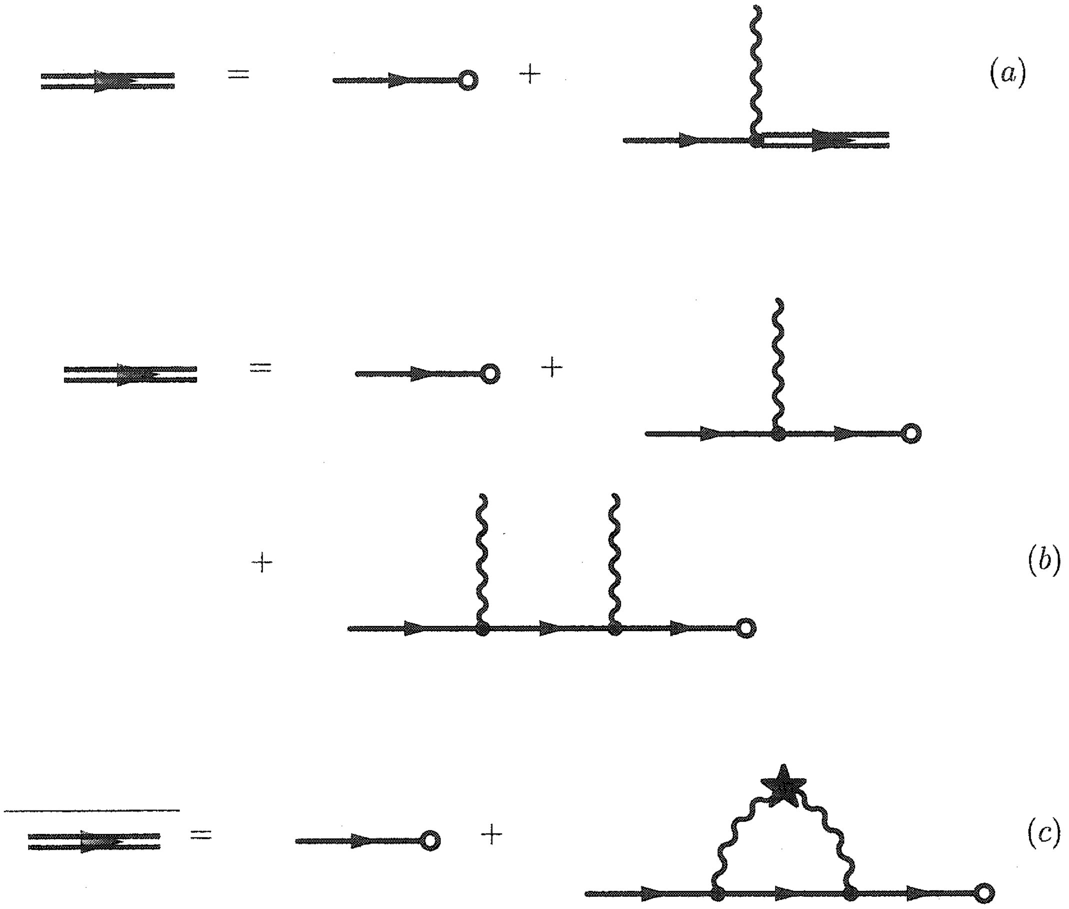

Figure 9.1: Diagrammatic representation of the Fourier-Laplace transformed, simplified equation, Eq. (9.5). Part (a) gives the exact equation while part (b) displays the perturbation series to second order. Part (c) gives the disorder averaged perturbation series to one loop order.

the equation of interest:

$$\begin{aligned}\widehat{W}(k,\omega) &= vG_0(k,\omega)\widetilde{W}(k,0)\\ &\quad + G_0(k,\omega)\int d^dq\int dt\int d\Omega_a\int d\Omega_b\; e^{-(\omega-(\Omega_a+\Omega_b))t}\,\widehat{U}(q,\Omega_a)\widehat{W}(k-q,\Omega_b),\end{aligned} \qquad (9.5)$$

with the abbreviations $\int d^dq \equiv \int_{-\infty}^{\infty}\frac{d^dq}{(2\pi)^d}$, $\int dt \equiv \int_0^{\infty} dt$, and $\int d\Omega_y \equiv \int_{y-i\infty}^{y+i\infty}\frac{d\Omega_y}{2\pi i}$ where $y = a$ or b.

A graphical representation of Eq. (9.5) is shown in Fig. 9.1(a). By recursively replacing $\widehat{W}$ on the right hand side of Eq. (9.5) with the equation itself, one obtains a perturbation expansion for $\widehat{W}$, shown to second order in Fig. 9.1(b). The disorder-averaged behavior is of interest, so the random growth rates $\widehat{U}$ must be averaged over. For a uniform distribution of width Δ, the correlator is

$$\overline{U(\vec{x},t)U(\vec{x},t)} = \frac{\Delta^2}{12} l_x^d l_t \delta^d(x)\delta(t), \tag{9.6}$$

where the overbar denotes the disorder average, l_x is the lattice length in the spatial directions, and l_t is the lattice length in the temporal direction. Applying the Fourier-Laplace transform gives

$$\overline{\widehat{U}(\vec{q},\Omega)\widehat{U}(\vec{q}',\Omega')} = (2\pi)^d \frac{\Delta^2}{12} l_x^d l_t \delta^d(\vec{q}-\vec{q}')\frac{1}{\Omega+\Omega'}. \tag{9.7}$$

As $\overline{U} = 0$, upon taking the disorder average of the perturbation expansion shown in Fig. 9.1(b), only the even-in-$\widehat{U}$ terms survive, with loops created from pairs of $\widehat{U}$ interactions. In Fig. 9.1(c) this result is shown to one-loop order.

In order to determine the renormalized disorder-averaged propagator $G_R(\vec{k},\omega)$, defined by the equation $\langle\widehat{W}(\vec{k},\omega)\rangle_U \equiv vG_R(\vec{k},\omega)\widetilde{W}(\vec{k},0)$, to one-loop order, the following integrals must be calculated. Following the second term in Fig. 9.1(c) one writes the integrals

$$\begin{aligned} &v\widetilde{W}(\vec{k},0)(2\pi)^d\frac{\Delta^2}{12}l_x^d l_t G_0(k,\omega)\int d^dq\int dt\int d\Omega_a\int d\Omega_b\ e^{-(\omega-(\Omega_a+\Omega_b))t}G_0(\vec{k}-\vec{q},\Omega_b) \\ &\times\int d^dq'\int dt'\int d\Omega_a'\int d\Omega_b'\ e^{-(\omega'-(\Omega_a'+\Omega_b'))t'}G_0(\vec{k}-\vec{q}-\vec{q}',\Omega_b')\frac{\delta^d(\vec{q}-\vec{q}')}{\Omega_a+\Omega_a'}. \end{aligned} \tag{9.8}$$

The $\int d^dq'$ is easily done and gives a $G_0(\vec{k},\Omega_b')$ factor. As G_0 represents pure diffusion, which has no exponential growth, for any $b > 0$ one has $\int d\Omega_b'\ e^{\Omega_b't'}G_0(\vec{k},\Omega_b') = \widetilde{G}_0(\vec{k},t')$. The Ω_a' integral is also simple, giving $\int d\Omega_a'\frac{e^{\Omega_a't'}}{\Omega_a+\Omega_a'} = e^{-\Omega_a t'}/2$. Then the t' integral is $\int dt'\ e^{-(\Omega_a+\Omega_b)t'}\widetilde{G}_0(\vec{k},t') = G_0(\vec{k},\Omega_a+\Omega_b)$. This completes the primed integrals, reducing Eq. (9.8) to

$$v\widetilde{W}(\vec{k},0)\frac{\Delta^2}{24}l_x^d l_t G_0(k,\omega)\int d^dq\int dt\int d\Omega_a\int d\Omega_b\ e^{-(\omega-(\Omega_a+\Omega_b))t}G_0(\vec{k}-\vec{q},\Omega_b)G_0(\vec{k},\Omega_a+\Omega_b). \tag{9.9}$$

The Ω_a integral gives $\int d\Omega_a e^{\Omega_a+\Omega_b)t} G_0(\vec{k}, \Omega_a + \Omega_b) = \widetilde{G}_0(\vec{k}, t)$ and then the t integral is $\int dte^{-\omega t}\widetilde{G}_0(\vec{k}, t) = G_0(k, \omega)$. This leaves the Ω_b integral, which may be evaluated via parameterization

$$\int d\Omega_b G_0(\vec{k} - \vec{q}, \Omega_b) = \int_{b-i\infty}^{b+i\infty} \frac{d\Omega_b}{2\pi i} \frac{1}{v\Omega_v + D(\vec{k} - \vec{q})^2} = \frac{1}{2v}. \tag{9.10}$$

Note that in the above integral $b > 0$ and the pole is in the left-half plane. Inserting these results back into Eq. (9.9) gives

$$\widetilde{W}(\vec{k}, 0) \frac{\Delta^2}{48} l_x^d l_t G_0^2(k, \omega) \int d^d q. \tag{9.11}$$

To cut off the divergence of the q integral, an upper cutoff proportional to the inverse lattice length is imposed, $q_{\max} = 2\pi / l_0$. Finally, this gives for the one-loop correction:

$$\widetilde{W}(\vec{k}, 0) \frac{S_d \Delta^2 l_t}{48d} G_0^2(k, \omega), \tag{9.12}$$

where S_d is the surface area of a d-dimensional sphere of unit radius.

9.1.1 Diffusion Crossover Time

To determine the effect of the disorder on the diffusion of the system, one must now calculate the correction to the diffusion constant. Using Eq. (9.12) from above, the renormalized propagator to one-loop order is

$$G_R(\vec{k}, \omega) = G_0(\vec{k}, \omega) + \frac{S_d \Delta^2 l_t}{48dv} G_0^2(k, \omega). \tag{9.13}$$

Expanding $G_0(\vec{k}, \omega)$ and $G_R(\vec{k}, \omega)$ for $k \to 0$ gives

$$\frac{1}{v\omega} - \frac{D_R k^2}{(v\omega)^2} = \frac{1}{v\omega} - \frac{Dk^2}{(v\omega)^2} + \frac{S_d \Delta^2 l_t}{48dv} \left(\frac{1}{(v\omega)^2} - \frac{2Dk^2}{(v\omega)^3} \right) + O(k^4). \tag{9.14}$$

From this equation one may read of the value for D_R:

$$D_R = D \left(1 + \frac{S_d \Delta^2 l_t}{24dv^2\omega} \right). \tag{9.15}$$

When the second term on the right side of Eq. (9.15) becomes on the order of one then the case of pure diffusion is no longer the dominant term. The crossover time is proportional to the value of $1/\omega$ at this point. From Eq. (9.15) the crossover time T is given by,

$$T = \frac{48\pi d v^2}{S_d l_t \Delta^2} \tag{9.16}$$

The crossover time depends on both the velocity of the flow as well as the width of the distribution of random growth rates. When the velocity increases, the system is pushed through the random environment before it has time to experience the fluctuations, seeing an effective average environment. Hence it makes sense that T is increased by higher velocities. On the other hand, increasing the width of the random distribution of growth rates creates optimal paths in the system that have larger effective growth rates. This causes pure diffusion to break down earlier, hence the inverse dependence with the crossover time. A further analysis of these two competing behaviors is given in Sec. 9.2.4.

9.2 Numerics

In order to test the predictions of super-diffusive behavior introduced in Sec. 8.1, as well as the behavior of the crossover time computed in Sec. 9.1, Eq. (9.1) was simulated numerically in one spatial dimension, x. This corresponds to the case of two-dimensional spreading in the full linear equation [Eq. (8.1) with $b = 0$]. Specifics of the numerical simulation implementation may be found in App. B. To understand the behavior of Eq. (9.1) the effect of the disorder on concentration profiles will first be examined (Sec. 9.2.1), followed by analysis of the increased growth rate (Sec. 9.2.2), the effective rate of diffusion (Sec. 9.2.3), and finally the behavior of the crossover time (Sec. 9.2.4).

9.2.1 Concentration Profiles

The simulations were started with an initial concentration profile that was a Gaussian with unit variance. This condition was used to mimic the inoculation of a medium with an initial bacterial sample. With no disorder in the environment, and hence no disorder in the growth rates, the initial concentration profile would simply spread out diffusively, keeping the shape of a Gaussian but with an increasing variance. With disorder, however, the Gaussian shape is destroyed, due to particularly favorable paths on which the bacteria may grow.

In Fig. 9.2 normalized concentration profiles for a single realization of the random growth rates are shown for various times t after the start of the simulation, along with the purely diffusive case. For relatively short times, the two profiles look roughly identical. As time increases, the disordered profile starts to deviate from the pure diffusion case by developing spikes. These regions correspond to the ends of a path in (x,t) space that had particularly favorable growth rates, and thus resulted in a much larger population of bacteria than would be expected from a homogeneous environment. For long times, these paths may end with increasing distance from the original starting position, effectively shifting the mean position of the concentration from the starting position. There may also be several competing paths that have nearly the same effective growth rate, resulting in several concentration spikes in the profile. These behaviors do not occur in the homogeneous case, as the spreading Gaussian profile always remains centered on the starting point and symmetric about that point.

For any particular realization of the disorder, from Fig. 9.2 it is clear that the profile at a given time deviates from the case of pure diffusion. However, it is not true that such a realization will exhibit the super-diffusive behavior predicted in Sec. 8.1. Defining the width of a given concentration profile as one standard deviation with respect to the mean of the profile, one finds that in almost all cases the width of

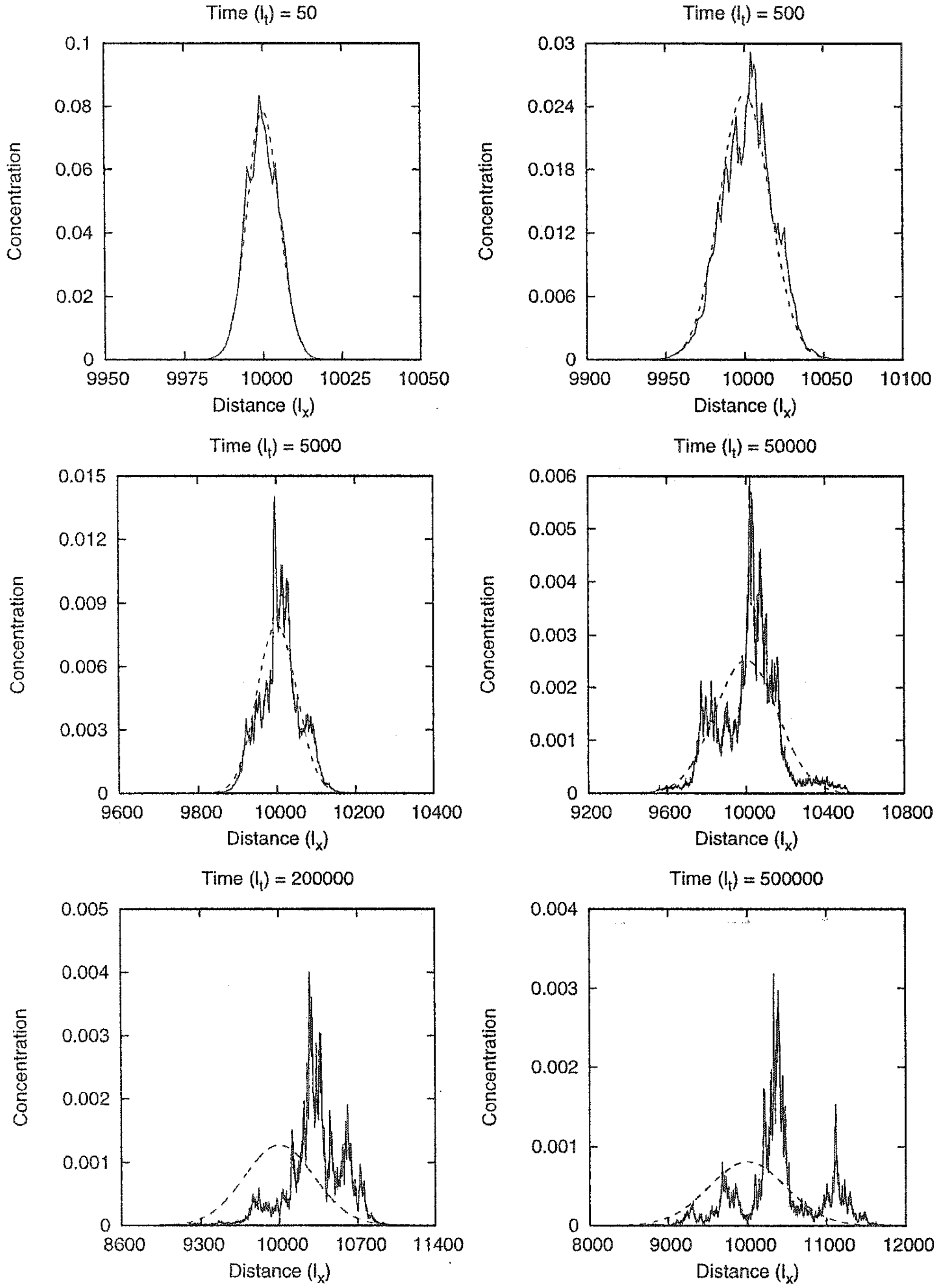

Figure 9.2: Concentration profiles for one-dimensional spreading according to Eq. (9.1), normalized by the total population. A Gaussian of variance one was used as the initial profile. The solid lines are profiles for a disordered environment with $v = 4.0$ and $\Delta = 1.0$. As time increases, spikes and asymmetries develop in the profiles, deviating from the purely diffusive case (dashed lines).

one realization grows either diffusively or sub-diffusively. The particular mode of spreading is governed by the behavior of the current dominant optimal path, which contains the majority of the profile's concentration. If this path is no longer experiencing above average growth rates then it effectively acts as if it is undergoing simple diffusion, resulting in a width that grows at about the diffusive rate. On the other hand, if the path is experiencing above average growth rates then it is growing exponentially faster than the other paths in the system. Therefore, after normalization the optimal path has acquired a greater percentage of the total population, causing a more sharply peaked spike in the concentration profile. This results in a narrower peak than would be obtained with pure diffusion, corresponding to growth that is sub-diffusive.

In light of the above behavior it becomes clear why the prediction for super-diffusive behavior is only for the disorder-averaged profiles and not for a single disorder realization. Large spikes in concentration may occur far from the mean of a profile undergoing pure diffusion. Upon averaging a large number of such profiles together, the concentration shifts away from the center of the average profile, resulting in super-diffusive spreading. To see the case clearly, Fig. 9.3 shows concentration profiles for times similar to those shown in Fig. 9.2 that have been averaged over 1000 disorder realizations. As in the single disorder realization profiles, for short times there is virtually no difference between the disordered case and the purely diffusive case. However, for long times the disorder-averaged profiles clearly begin to spread more quickly than the corresponding diffusive profiles. Further analysis of this spreading may be found in Secs. 9.2.3 and 9.2.4.

9.2.2 Anomalous Growth

The concentration profiles shown in Figs. 9.2 and 9.3 for the disordered systems were normalized in order to have a clear comparison to the case of pure diffusion. In

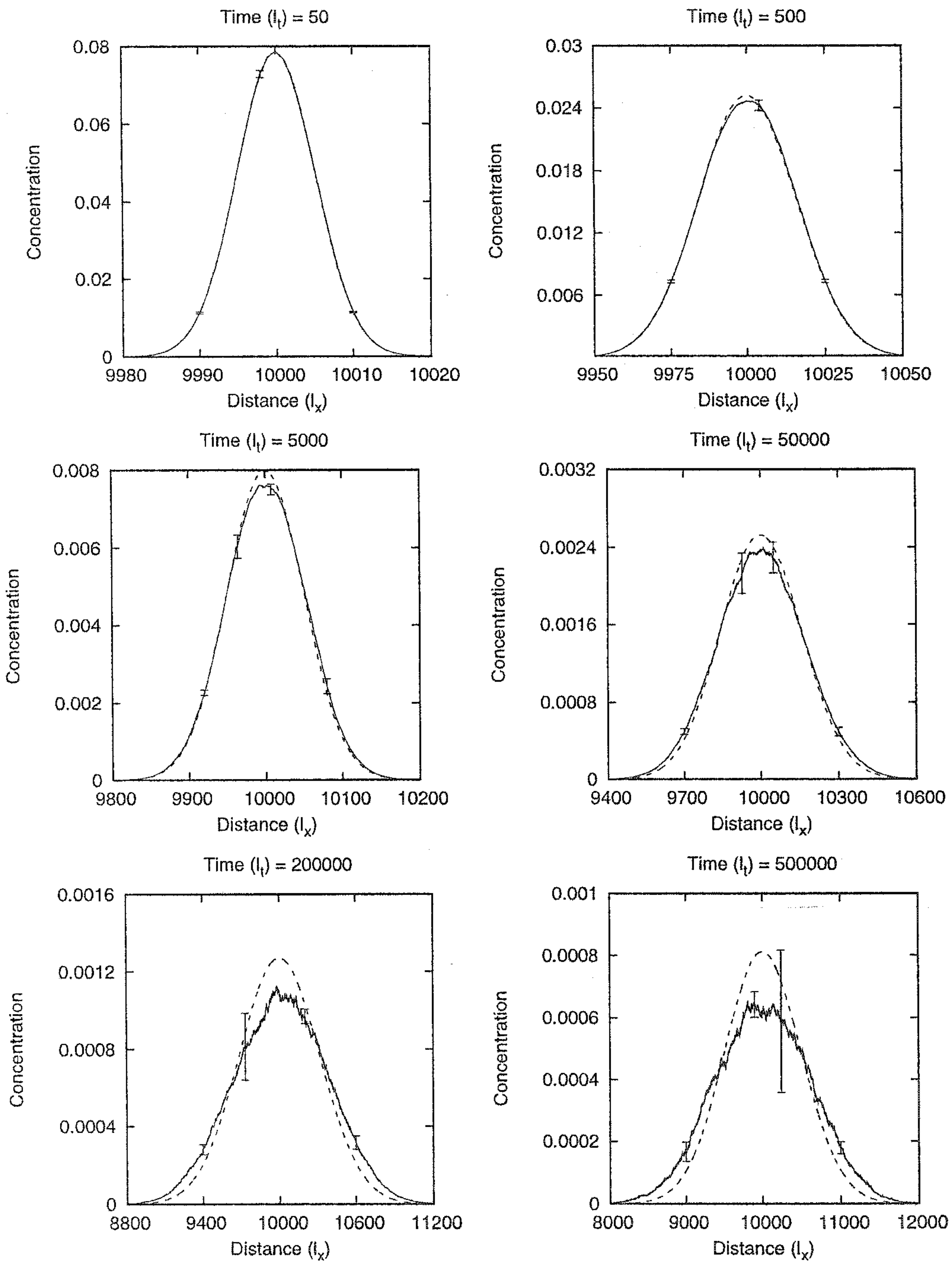

Figure 9.3: Average concentration profiles for one-dimensional spreading according to Eq. (9.1), normalized by the total population and averaged over 1000 random configurations. A Gaussian of unit variance was used as the initial profile. The solid lines are the average profiles for disordered environments with $v = 4.0$ and $\Delta = 1.0$ with a maximal and several characteristic error bars shown. As time increases, the profiles spread faster than the purely diffusive case (dashed lines).

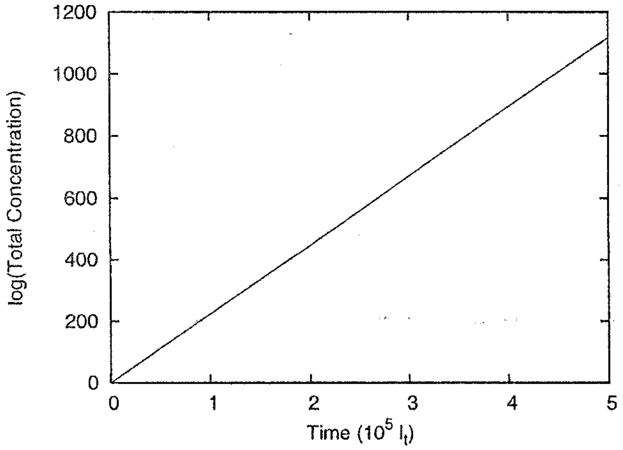

Figure 9.4: Total population vs. time for a disordered environment with $v = 4.0$ and $\Delta = 1.0$. The total population displays a linear behavior on the log scale, so the population grows exponentially in time. The growth factor, given by the slope of the line, is $0.00223/l_t$.

this latter case, starting with a profile of total concentration one results in the same total concentration for all later times, as there is no growth term in Eq. (9.1) for $U(\vec{x}, t) = 0$. When disorder is included, this simple picture breaks down. Although U has a zero average, the fluctuations in the growth factors lead to anomalous growth. In Fig. 9.4 the total concentration is shown as a function of time for a system with $\Delta = 1$ and $v = 4$. A log scale is used, so the resulting linear curve indicates that the total population is growing exponentially in time. The slope of the curve, $0.00223/l_t$, is the effective growth factor. Although this growth factor is indeed very small, it still has a very profound effect. At the longest times, $t = 500000 l_t$, the total population (unnormalized) becomes on the order of e^{1100}. Physically, the total population and the bacterial density must remain bounded. The problem here is that the nonlinear death (or competition) term has been dropped in the simplified equation, Eq. (9.1). The effect of including this nonlinear death term is discussed further in Sec. 10.2.

A simple argument for the appearance of this anomalous growth lies in the asymmetry between the growth and death processes. In particular, consider a small concentration of bacteria present in a favorable environment, $U > 0$. This concentration

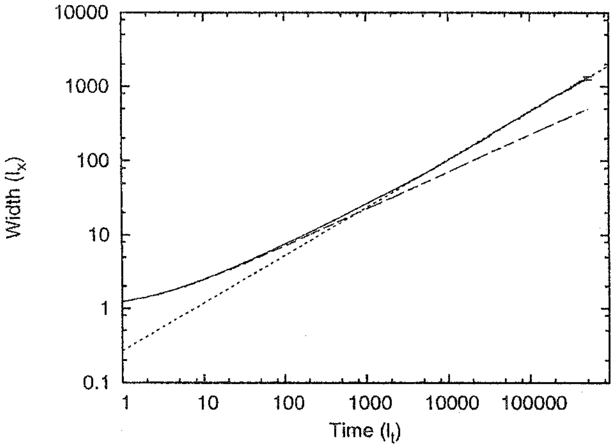

Figure 9.5: Concentration width vs. time for a disordered environment with $v = 4.0$ and $\Delta = 4.0$ (solid line) and the purely diffusive case (dashed line). The former case is averaged over 1000 disorder realizations. Both curves start out with a power-law of 0.5, but for long times the disordered case switches to a power-law of 0.647 ± 0.001. The 0.647 power-law is shown as a dotted line. Statistical errors are generally smaller than the error bar shown for the longest time.

will grow exponentially in time, and will spread additional concentration to neighboring areas via diffusion. On the other hand, in an unfavorable environment for growth, with $U < 0$, the local population will experience an exponential decay in concentration. Although this decreases the total local population, the decrease imposed on neighboring areas is not the opposite of the growth case. The asymmetry lies in the fact that the local (and total) population cannot fall below zero. One cannot have a negative number of organisms. Hence, the difference in concentration between neighboring sites, proportional to the rate of transport, is smaller with $U < 0$, leading to a reduced rate of population loss compared to the gain in population when $U > 0$. Therefore, the asymmetry of the diffusion process in the random environment effectively leads to an increased growth rate.

9.2.3 Diffusion Exponent

To measure the diffusion exponent, the width of the disorder-averaged concentration profile, such as shown in Fig. 9.3, was measured as a function of time. The resulting curves are shown in Fig. 9.5 for a disordered environment with $v = 4.0$ and $\Delta = 4.0$ and for the case of pure diffusion. In the latter case, the profile width grows as $t^{0.5}$, as one expects for pure diffusion. The disordered case is different, with two regions of clearly different power-law behaviors. For small times the disordered width follows the behavior of the purely diffusive case, as expected. However, as the time becomes large, the disordered case deviates from pure diffusion, and instead grows with a power-law exponent equal to 0.647 ± 0.001. This super-diffusive behavior is in good agreement with the exponent value 2/3 that has been previously predicted [114]. As explained in Sec. 9.2.1, this super-diffusive behavior arises due to the appearance of optimal growth rates whose positions deviate far from the center of the population that is obtained absent disorder. Upon averaging, these deviations shift concentration from the center of the profile, resulting in a width wider than the diffusive case.

9.2.4 Crossover Time Behavior

With disorder in the growth rates of the system, the increase of the population width in time crosses over from a diffusive exponent to a super-diffusive exponent. In Fig. 9.5 this crossover occurs at a relatively early time. However, this crossover time depends on the parameters in Eq. (9.1). As an example, Fig. 9.6 shows a similar plot of the width versus time for a system with $v = 4.0$ and $\Delta = 1.0$. Now the crossover to super-diffusive behavior occurs at a much later time, and the system has not yet saturated at the full super-diffusive exponent at the longest times simulated.

In Sec. 9.1.1 a prediction for the behavior of the crossover time was calculated from a perturbative analysis of Eq. (9.1). As the system is being simulated in one spatial dimension, Eq. (9.16) gives for the crossover time

$$T = \frac{24\pi v^2}{\Delta^2}. \tag{9.17}$$

Comparing the points in Figs. 9.5 and 9.6, in which the widths visually appear to cross over to super-diffusive behavior, with the value calculated from Eq. (9.17) indicates

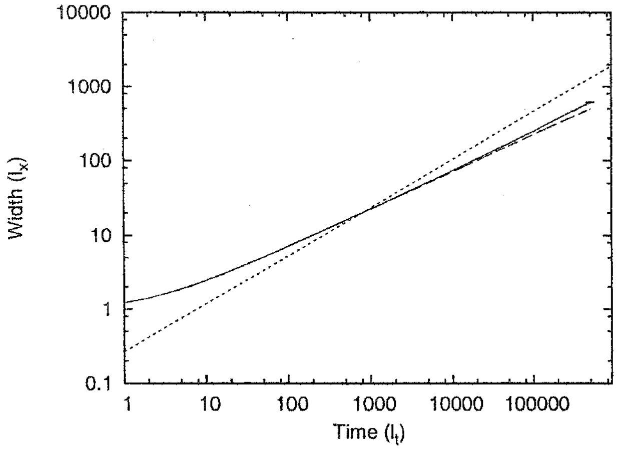

Figure 9.6: Concentration width vs. time for a disordered environment with $v = 4.0$ and $\Delta = 1.0$ (solid line) and the purely diffusive case (dashed line). The former case is averaged over 1100 disorder realizations. Both curves start out with a power-law of 0.5, but for long times the disordered case begins switching to super-diffusive behavior although it does not saturate at the full power law for the longest simulated times. A power-law of 0.647 is shown as an offset dotted line. Statistical errors are generally smaller than the error bar shown for the longest time.

that the prediction is roughly an order of magnitude too small. However, this should not be unexpected, as Eq. (9.17) really describes the time where departure from purely diffusive behavior begins. At this point, the width is growing super-diffusively, but it does not saturate at the full exponent until $t \gg T$, hence the order of magnitude discrepancy between Eq. (9.17) and Figs. 9.5 and 9.6.

To test the dependence of the crossover time, Eq. (9.17), on the velocity and width of the random growth rates the following procedure was used. First, to obtain a baseline definition of the crossover time, the difference in widths between the disordered and purely diffusive case was measured for the system with $v = 4$ and $\Delta = 1$ at roughly the crossover time predicted by Eq. (9.17), $t = 1200$. Then the values of v and Δ were varied, and the effective crossover time for a particular set of these two parameters was determined by the time at which the difference in widths between the disordered and diffusive cases equaled the value obtained in the first step. The resulting crossover times for a range of v and Δ values are shown in Fig. 9.7. Each point

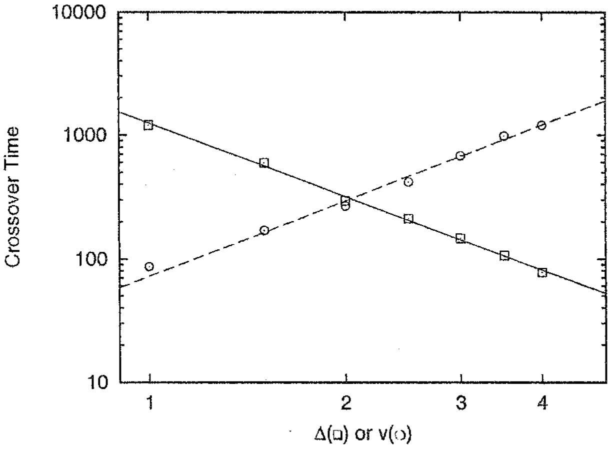

Figure 9.7: Crossover time dependence on Δ and v. Squares denote variation of Δ with $v = 4.0$ while circles show variation of v for $\Delta = 1.0$. Times were determined from a baseline difference from the pure diffusive width taken at the approximate time computed from Eq. (9.17) with $\Delta = 1.0$ and $v = 4.0$, $t = 1200$. The solid line shows a power law -1.97 ± 0.05 and the dashed line a power law 2.03 ± 0.10 as fit to the data varying Δ and v respectively. Statistical error bars are on the order of the symbol size.

was averaged over 3000 random configurations, and the statistical error is roughly the size of the symbols. As seen in Fig. 9.7, the crossover times agree well with the quadratic behaviors predicted by Eq. (9.17) for both Δ and v, $T \sim (v/\Delta)^2$.

Chapter 10

Two-Dimensional Spreading

Super-diffusive spreading was found in Ch. 9 for an equation, Eq. (9.1), that represented a simplification of the full reaction-diffusion equation describing bacterial growth in a random environment. Now attention is turned toward investigating the applicability of this simplification for the full equation. In particular, the two-dimensional spreading case will be examined, as this corresponds to the one-dimensional simplified equation studied in the previous chapter. To that end, it is assumed that spreading occurs in the (x, y) plane with the convection velocity $\vec{v}$ taken to be in the y direction, $\vec{v} = v_y$. Equation 8.1 may then be rewritten as

$$\partial_t c = D\nabla^2 c - v\partial_y c + [a + U(x,y)]c - bc^2, \tag{10.1}$$

where $c \equiv c(x, y, t)$. The initial condition is taken to be a point concentration, corresponding to a point inoculation of bacteria. The magnitude of inoculation is dependent on the parameter b, as described later. As in Ch. 9, the behavior of this initial concentration under Eq. (10.1) for $t > 0$ is of interest. Although in Ch. 9 the ratio of v to Δ, the width of random growth rates $U(x, y)$, was varied widely, one must be more careful for the case of the full equation. If the ratio of v/Δ falls too low then the initial droplet of bacteria will no longer be delocalized, but rather will leave behind populations at particularly favorable growth areas. This is true for both the $b = 0$ and $b > 0$ cases, although due to different mechanisms. Hence, to ensure a delocalized system, and thus the applicability of the arguments in Sec. 8.1, one is restricted to a reduced set of v and Δ values. Such details of the simulation code are discussed in App. B. For convenience, all time and lattice parameters are set to one in the following. To test the super-diffusive growth prediction, first a comparison will be made with the results from the simplified equation by numerically analyzing Eq. (10.1) including only the linear growth term (Sec. 10.1) followed by an numerical analysis of the effects arising from including nonlinear growth (Sec. 10.2).

10.1 Linear Equation

To test the behavior of Eq. (10.1) with only linear growth terms, the parameter b is set to zero. In addition $a = 0$ is imposed so that only the random growth rates contribute to the linear growth term. The growth rates $U(x, y)$ are chosen from a uniform distribution of width Δ. If $\Delta = 0$ then there is no growth in the system, so one expects to find a constant total population that spreads diffusively in all directions with a center that moves at the convection velocity v. On the other hand, with $\Delta > 0$ (and v implicitly large enough to give delocalization) the population should no longer grow diffusively in all directions, but on average grow super-diffusively in the x direction, as predicted in the arguments of Sec. 8.1. In the direction parallel to the flow, the y direction, the population is still expected to exhibit diffusive growth and to have the center of the colony drift with the convection velocity. In the simulations, the convection velocity was kept fixed and the width of the growth rate distribution was varied.

10.1.1 Concentration Contours

Whereas for a one-dimensional system one may easily visualize the entire concentration profile, as in Fig. 9.2, with two spatial dimensions the three-dimensional profile surface is difficult to visualize in a two-dimensional projection. For this reason equi-concentration contours are used. These contours connect neighboring points of the profile that are at the same concentration level. Typically, more contours surrounding a given point indicate that the point is at a higher level of concentration. Thus, with a few contours one may get an idea of the full shape of the concentration profile. To compare with the purely diffusive case, one may not simply pick arbitrary concentration levels to plot for the profiles. Clearly the contours for pure diffusion will be circular, and centered about the inoculation point (after accounting for the convection velocity). However, to compare with a corresponding contour for the random growth case, the total population inside a diffusive contour must equal the total population inside the corresponding random growth contour. In this way, if the case of random growth was behaving diffusively, one would find that the contours are of the same diameter. Large deviations in diameter thus indicate nondiffusive growth.

In Fig. 10.1 the concentrations of a bacterial colony at short and longer times after inoculation are shown. For the relatively short time, the concentration contours deviate only slightly from the circular diffusive contours. This situation is very similar to that in Fig. 9.2. For short times, the disordered system appears to mainly undergo simple diffusion. On the other hand, for the longer time shown in the lower portion of Fig. 10.1 the profiles no longer closely resemble the circular contours of the diffusive case. Instead, they are more elliptical in shape. At this point one must look at each direction independently. In the y direction, parallel to the convection velocity, the disordered contours still have roughly the same diameter as the purely diffusive contours. This indicates that in this direction diffusion is still dominating. However, in the direction perpendicular to the convection velocity, the x direction, the contours

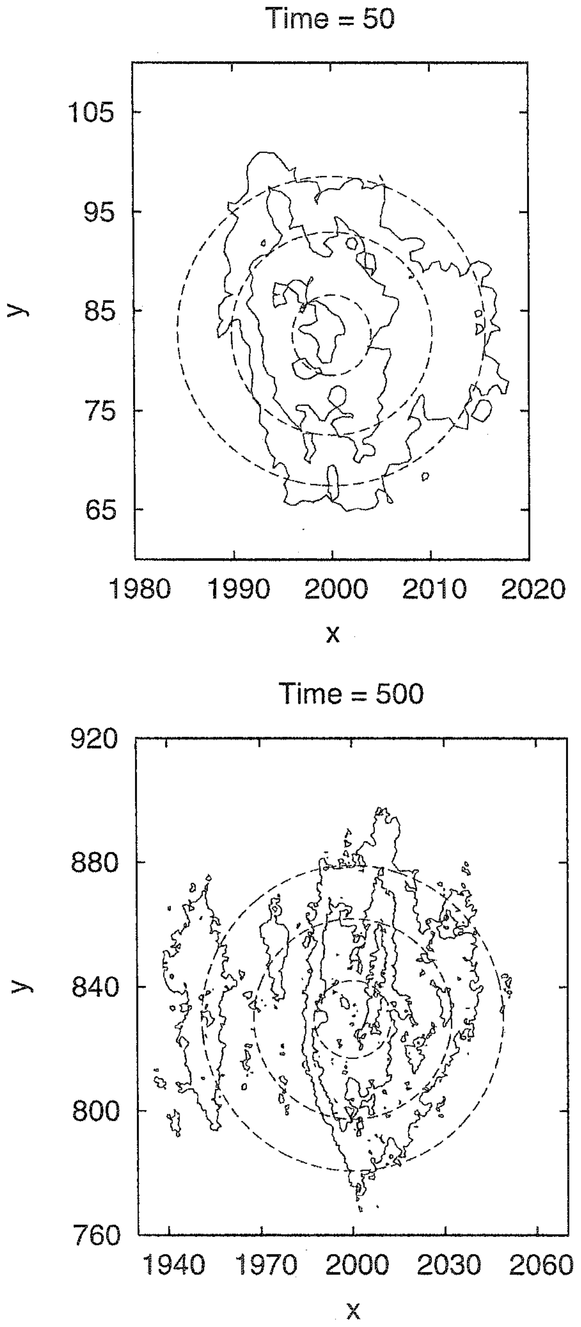

Figure 10.1: Concentration contours for two-dimensional spreading according to Eq. (10.1), normalized by the total population and starting with a point inoculation at $(2000, 0)$. Convection is in the y direction. The solid lines give contours for a disordered environment with $\Delta = 2.0$. As time increases, spikes and asymmetries develop, along the x direction evidenced by contours which deviate from the purely diffusive case (dashed lines). In the y direction contours have similar widths as the diffusive case. Contour levels starting from the outside encircle 80, 50, and 10 percent of the total population.

have much smaller diameters, and the centers appear to be shifted away from the center of the diffusive case. This indicates that an off-center peak in the concentration profile is developing in the x direction due to particularly favorable growth rates in paths to that position. This behavior is exactly mirrored in the profiles of the one-dimensional simplified equation shown in Fig. 9.2. These off-center peaks indicate that in the x direction super-diffusive behavior will be found upon taking the disorder average.

In comparing the contours with and without disorder, the purely diffusive contours were shifted downwards along the direction of convection to align with the center of the disordered contours. This is required, due to a decreased effective velocity in the disordered system. A similar decrease of v in the presence of random growth rates was predicted in the context of the average growth spectrum [114]. The actual magnitude of the shift used in Fig. 10.1 was determined by aligning in the y direction the disorder-averaged concentration contours with the purely diffusive contours. Figure 10.2 displays the disorder-averaged contours for the same times as shown in Fig. 10.1. The behavior of the disorder-averaged concentration contours again is very similar to the one-dimensional case of Fig. 9.3. For short times there is almost no difference between the random and uniform growth rates. However, at longer times the contours for the random growth become elliptical, spreading faster in the direction perpendicular to the convection (x) but still having the same diameter in the parallel direction (y). Thus there is diffusive growth along the convection velocity and super-diffusive growth perpendicular to the convection velocity, as expected.

For reasons that will become apparent in Sec. 10.2, it is useful to examine the behavior of the tails of the concentration profiles. Concentration contours for the same system as shown in the bottom of Fig. 10.1 are shown in Fig. 10.3 for very small concentration levels. At these small levels, several orders of magnitude smaller than the peak values of the profiles, the contours remain circular in appearance. Thus

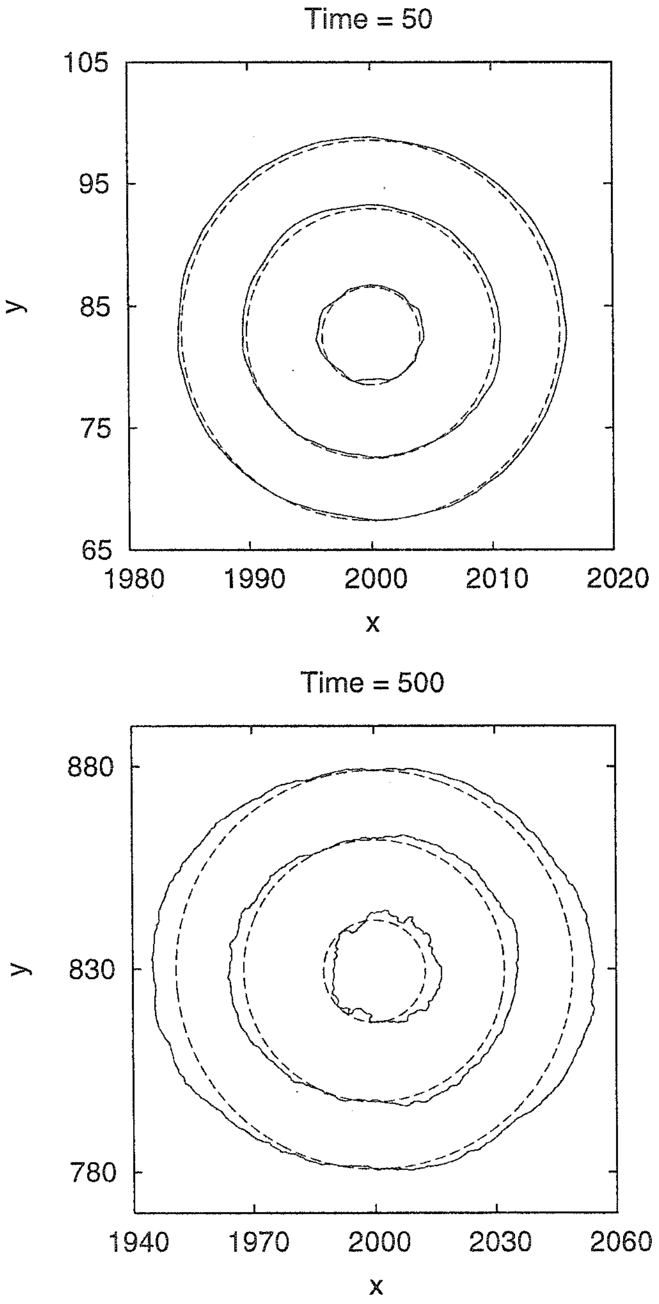

Figure 10.2: Average concentration contours for two-dimensional spreading according to Eq. (10.1) for 1000 disorder realizations, normalized by the total population and starting with a point inoculation at $(2000, 0)$. Convection is in the y direction. The solid lines give contours with $\Delta = 2.0$ and the dashed lines contours for the purely diffusive case. For short times the disordered and pure systems spread identically in all directions, while for longer times the disordered system spreads super-diffusively in the x direction, and only diffusively in the y direction. Contour levels starting from the outside encircle 80, 50, and 10 percent of the total population. To compensate for a smaller effective convection velocity, the diffusive contours are shifted downwards by 3.5 and 36 in y for $t = 50$ and 500 respectively.

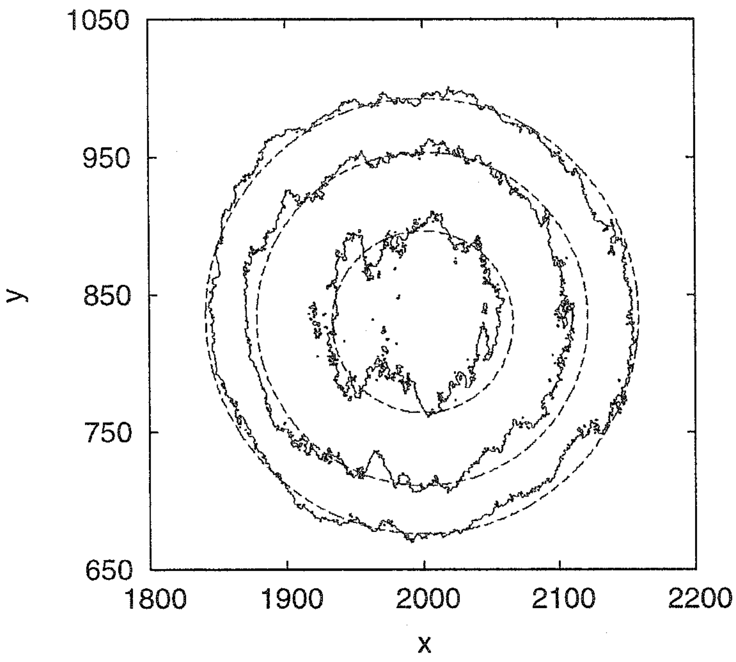

Figure 10.3: Two-dimensional spreading contours for small concentrations normalized by the total population. Convection is in the y direction. The solid lines give contours for a disordered environment with $\Delta = 2.0$ at time $t = 500$, corresponding to the same system as shown in the bottom of Fig. 10.1. For small concentration levels the contours appear roughly circular and coincide with the purely diffusive case (dashed lines) indicating that the effect of the disorder has not caused super-diffusive behavior at this level. Starting from the outside, contours have the concentration levels 10^{-11}, 10^{-8}, 10^{-5} which encloses nearly the entire population except for the last level which encloses only 94 percent.

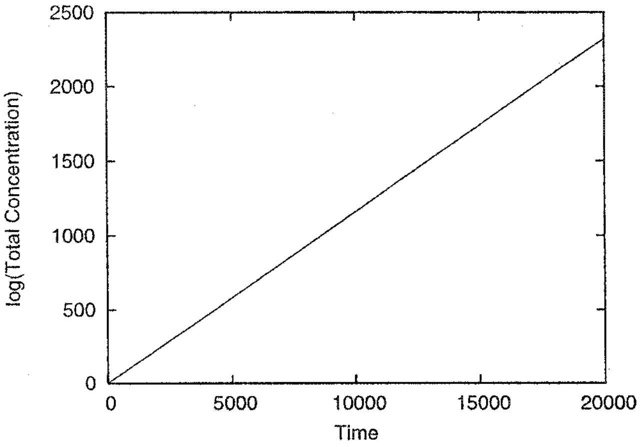

Figure 10.4: Total population vs. time for two-dimensional spreading according to Eq. (10.1) with $a = 0$, $\Delta = 2.0$, and averaged over 100 disorder realizations. The population grows linearly in time on a log scale indicating exponential growth. The slope of the line, 0.116, is the effective growth factor.

the spreading is still diffusive in nature in these areas. Recall that the disordered profile has been normalized in order to compare to the diffusive case. Hence, even though the contours have roughly the same diameter as in the diffusive case, the real concentration at these points is still larger than that found for pure diffusion. This is due to exponential growth in the disordered system, even with a zero mean growth rate ($a = 0$) [114]. The situation is very similar to the one-dimensional simplified equation, Sec. 9.2.2, in that the random growth rates cause exponential growth in the system, as seen in Fig. 10.4. Taking into account the total population's rate of increase, as given in Fig. 10.4, the population for the random growth rates of Fig. 10.3 is roughly e^{58} times larger than the diffusive case at that point ($t = 500$). Thus, with random growth rates the tails of the population are always larger than the purely diffusive case, resulting in a larger effective decay constant. The implications of this slower decay arise again when examining the nonlinear case, $b > 0$, in Sec. 10.2.3.

10.1.2 Population Width

In light of the fact that the concentration contours for the case of random growth rates contain asymmetries and spikes, as found for the simplified equation, one would expect to find super-diffusive behavior in the disorder-averaged width of the population. Qualitatively, this expectation is met, as seen in the disorder-averaged concentration contours of Fig. 10.2. From these plots it is clear, however, that the two relevant directions must be treated separately. As the asymmetries of the concentration spikes appear to occur only in the direction perpendicular to the convection velocity, super-diffusive behavior should occur in this direction, whereas in the direction parallel to the velocity there should be simple diffusion.

To test these expectations quantitatively the disorder-averaged widths of the population with random growth rates were measured for both the directions parallel to and perpendicular to the convection velocity. For a particular direction, the width is calculated as the standard deviation of the marginal distribution for that direction. The resulting curves are shown in Fig. 10.5. As expected, the purely diffusive case follows a power-law, $t^{0.5}$, for both spatial directions. The disorder-averaged width for the parallel direction also follows this power law. Whereas the width for the perpendicular direction starts out also following the diffusive behavior, at the longest times measured it has begun to spread faster, thus becoming super-diffusive. Unfortunately, due to the various limits of the simulation (see App. B) it is not clear that the full onset of super-diffusive behavior has been reached. A similar problem was encountered with the results of the one-dimensional equation in Ch. 9, in particular for Fig. 9.6, where a similar, late onset of the super-diffusive behavior made for an inaccurate measurement of the exponent. Thus, the power law measured for this two-dimensional case, t^{α} with $\alpha = 0.585 \pm 0.002$, may be an underestimate of the true value. Additionally, the accuracy of the measurement is reduced because the long times required for a simulation constrained the number of random configura-

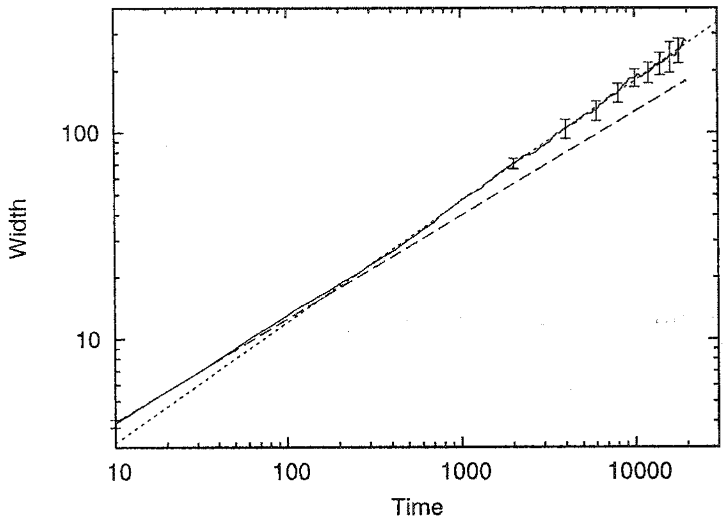

Figure 10.5: Concentration width vs. time for a two-dimensional disordered environment governed by Eq. (10.1) with $\Delta = 2.0$ averaged over 100 disorder realizations. The width of the direction perpendicular to the convection velocity (x) is shown as a solid line with several characteristic error bars, while the width in the parallel direction (y) is shown as a dashed line. The purely diffusive case, equivalent in both directions, grows in width identically to the y direction with disorder and has the expected power-law of 0.5. For the disordered case, the perpendicular curve starts out with the same power-law of 0.5, but for later times the width grows more quickly with a power-law of 0.585 ± 0.002 shown as a dotted line.

tions available for averaging. The crossover time calculated for this situation from Eq. (9.16), $T = 57$, has a similar agreement with Fig. 10.5 as discussed for the one-dimensional case in Sec. 9.2.4. Namely the predicted value of T underestimates the visually observed crossover by roughly an order of magnitude (see Sec. 9.2.4).

10.2 Nonlinear Equation

Spreading of a bacterial population with only linear growth terms was studied in one and two-dimensions in Ch. 9 and Sec. 10.1. Looking at the anomalous growth found in these situations makes it clear that, for any real physical system, the purely linear growth may apply only for a short time. For long times, the growth of the bacteria must be cut off when the bacteria concentration reaches a saturation value, limited by competition for resources such as food. Thus, to model a more realistic system, the death term in Eq. (10.1) is now included by setting $b = 0.1$. To ensure a nonzero carrying capacity, given by a/b, $a = 0.05$ was chosen. From the standpoint of the linear growth, the choice of a may be made freely, without affecting the super-diffusive behavior. However, for nonlinear growth the choice of a is more important, as will be seen below.

10.2.1 Concentration Contours

The introduction of the death term and the resulting carrying capacity produce a drastic change in the behavior of the concentration profile from the situation seen in Sec. 10.1. Absent any random growth rates, a Fisher wave moves symmetrically outward, centered about the point of inoculation shifted by the convection velocity. Inside the wavefront, the concentration is saturated at the carrying capacity, whereas beyond the wavefront the concentration decays exponentially. Here, the value of the mean growth rate a is important, as the wavefront speed, given by the Fisher velocity (see Ch. 8), is proportional to $\sqrt{a}$. To ensure that the system is delocalized, in the sense that a population is always "blown off" a favorable area for growth, this wave front speed must be smaller than the convection velocity of the system. Hence, the above choice of $a = 0.05$ was made to provide a wavefront speed well below the convection velocity.

Adding random growth rates to the equation with widths similar to those examined for the linear problem (Sec. 10.1) results in a slightly changed picture. Figure 10.6 displays several concentration contours for this case. As in the pure case, a Fisher-like wave front develops that propagates outward in a symmetric fashion. Inside this wave front, the effect of the random growth rates is apparent. The concentration fluctuates around the mean carrying capacity a/b. This is caused by the fact that the random growth rates change the local carrying capacity, and the population tries to adjust to the new value. As the response to changes is slow, due to the large convection velocity, the fluctuations tend to elongate and smear out along the direction parallel to the convection. The edge of the wave front, which should be roughly circular, may thus be easily found by examining where the fluctuations in a given contour level become large enough to destroy the circular front. Typically, for the populations shown in Fig. 10.6, this occurs at a concentration level slightly below the carrying capacity.

10.2.2 Wave Front Velocity

By introducing the nonlinear death term via setting $b = 0.1$, the diffusion found in Sec. 10.1 was replaced by a Fisher-like wave. Thus, one can no longer consider deviations from diffusive behavior in the width of the population. Instead, one must ask what effect the random growth rates have on the velocity of the wave front and whether there is a directional dependence on this change. For this purpose, the diameter of populations growing according to Eq. (10.1) is plotted against the time and is shown in Fig. 10.7. The slope of the line is twice the velocity of the wavefront as

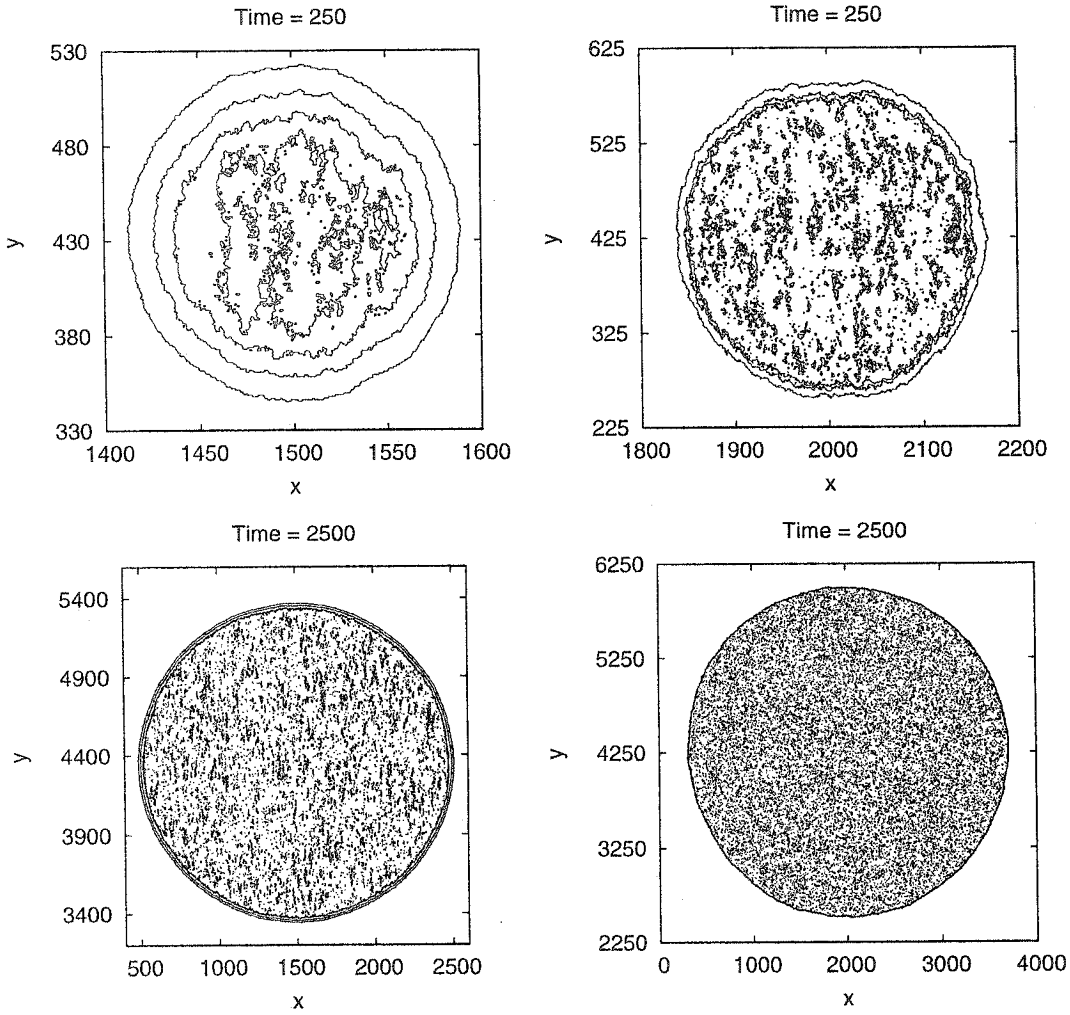

Figure 10.6: Concentration contours with a carrying capacity for two-dimensional spreading according to Eq. (10.1) at two times after a point inoculation. The outer contours show the wavefront (small concentrations) while inner contours are at concentration levels at or above the mean carrying capacity of $a/b = 0.5$ with $b = 0.1$. The left plots correspond to weaker disorder, $\Delta = 0.5$, and the right plots correspond to stronger disorder, $\Delta = 2.0$. As time increases, a Fisher like wave spreads symmetrically outward. The effect of the random growth rates is apparent inside the wavefront where the population fluctuates, following the local carrying capacity. For stronger disorder the wavefront also becomes more noisy.

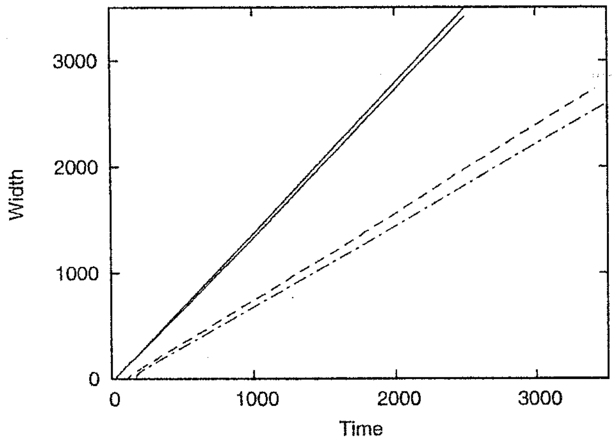

Figure 10.7: Population diameter vs. time for nonlinear spreading according to Eq. (10.1) with $a = 0.05$, $b = 0.1$. With random growth rates $\Delta = 2.0$ (solid lines) and $\Delta = 0.5$ (dashed lines) the diameter grows faster than in a uniform growth environment with $\Delta = 0$ (dot-dashed lines). Both the directions parallel and perpendicular to the convection behave identically for $\Delta = 0$ and 0.5 while the width perpendicular to the convection grows slightly faster for the strongest disorder. This slightly faster growth is just a simulation artifact due to nearing the regime where the front velocity nears the convection velocity (see text). The wave front velocities are 0.707 ± 0.010, 0.412, and 0.384 for the disorders $\Delta = 2.0$, 0.5, and 0.0 respectively where the estimated error is from the two slightly different wavefront velocities.

the velocity of the two opposite fronts add to give the population diameter's rate of increase. As seen in Fig. 10.7, this diameter grows identically in both the x and y directions, resulting in a symmetric wavefront, except for the cases of largest disorder. However, the random growth rates still have an effect as the velocity of the wavefront is clearly larger than when there is a single, uniform rate. So, although there is no asymmetry, the situation is similar to the linear growth, in that addition of random growth rates causes the population to spread out faster than with uniform growth rates, although here for both directions. The apparent, small asymmetry between the two directions, found for the largest disorder, is due to the wavefront velocity approaching the convection velocity, and is an artifact of the simulation code, which has been adapted for large convection velocities. When the wave front velocity becomes equal to the convection velocity, the trailing edge of the wave front becomes stationary, and this violates the assumptions of the code approximations (see App. B). A similar effect is seen in the absence of random growth rates if the wavefront velocity is tuned to a similar magnitude by adjusting the growth rate to $a \approx 0.17$.

The reason for the changes from the asymmetric linear growth behaviors found in Sec. 10.1 can be understood as follows. First, the asymmetry in growth found for linear growth arose from the appearance of large spikes of concentration that occurred with increasing distance from the initial center of the population. Upon taking the disorder average, these skewed profiles led to the super-diffusive behavior in the direction perpendicular to the convection. When the nonlinear death term is included, the spikes in concentration that would have developed are no longer allowed to grow, as they are cut off by the death term at the system's carrying capacity. Hence, a large skew in the population cannot develop; rather it remains roughly uniform near the bulk carrying capacity. This results in the symmetric growth of the two directions.

On the other hand, the enhanced growth found for the linear case, which has an effective growth rate greater than the mean growth rate, still applies when the nonlinear term is included. Although the growth is still cut off inside the wave front by the carrying capacity, outside the wave front the system is still effectively in the linear regime, and so enhanced growth is found. The effect of this enhanced growth on the wavefront velocity can be understood from the following argument. It has been shown that the wavefront velocity for a Fisher wave depends on the initial condition of the system [7]. In particular, if the initial condition falls off for long distances with, or faster than, exponentially (e^{-qx} with $q \geq 1$), then the wavefront will propagate at the minimum velocity, the Fisher velocity. If, on the other hand, the initial condition has a slower decay ($q < 1$) then a higher wavefront velocity will be found [7]. Hence, the random growth rates cause an increase in the wavefront velocity because the enhanced growth factor causes the concentration to fall off more slowly (by a factor of $e^{a't}$) than the uniform case.

10.2.3 Theoretical Wave Front Velocity

Using the above argument for the observed increase in wave front velocity upon introduction of random growth rates, one may derive a simple expression describing the wave front velocity. In particular, as the system is in the linear regime, far outside the wave front one may assume a simple form for the concentration:

$$c(\vec{x},t) \sim \exp\left(a't - \frac{|\vec{x}-\vec{v}t|^2}{4Dt}\right), \tag{10.2}$$

where $a' = a + a_{\text{eff}}$ is the real growth factor of the system. This includes the mean growth rate a, as well as the effective growth rate a_{eff}, which is the effective growth rate for the corresponding linear system with a zero mean growth rate. This latter parameter is of course dependent on the width of the random growth rates. The exponential growth from the compound growth rate a' is coupled with a simple diffusive form for the spatial dependence of the concentration. This form, homogeneous in all directions, is acceptable, assuming that the wave front is symmetric, which has been shown numerically in this case (see Fig. 10.6). Furthermore, the concentration outside the wavefront must also be symmetric. As found in Sec. 10.1.1 and seen in Fig. 10.3, for small concentration levels this assumption holds. In the linear regime the concentration must of course be small, and this corresponds to the argument of the exponential function in Eq. (10.2) being very negative:

$$a't - \frac{|\vec{x} - \vec{v}t|^2}{4Dt} \ll -1. \tag{10.3}$$

At a given distance $|\vec{x}_0 - \vec{v}t|$ from the center of the droplet, Eq. (10.3) becomes $|\vec{x}_0 - \vec{v}t| \gg \sqrt{4Dt(a't+1)}$, which reduces to $|\vec{x}_0 - \vec{v}t| \gg 2\sqrt{Da'}t$ for long times. This equation says that to stay at a small enough concentration level to remain in the linear regime, the distance from the droplet center must increase at the rate

$$v_{\mathrm{wf}}(\Delta) = 2\sqrt{D(a + a_{\mathrm{eff}}(\Delta))}. \tag{10.4}$$

But the speed at which a given concentration level in the linear regime moves outwards is identical to the speed of the wave front, v_{wf}. Hence, Eq. (10.4) gives the implicit dependence of the wave front speed on disorder via the effective growth rate a_{eff}. Note that uniform growth rates give $a_{\mathrm{eff}} = 0$, and so Eq. (10.4) then reduces to the Fisher velocity [7].

For the wave front speeds found in Fig. 10.7, the systems had $D = 0.75$ and $a = 0.05$. The Fisher velocity is therefore $v_{\mathrm{wf}}(0) = 0.387$. Comparing to the measured value in Fig. 10.7, $v = 0.384$, excellent agreement is found. For the case $\Delta = 2.0$, the growth rate $a_{\mathrm{eff}} = 0.116$ was measured (see Sec. 10.1.1). This gives the prediction $v_{\mathrm{wf}}(2.0) = 0.706$, again in excellent agreement with the measured value $v = 0.707 \pm 0.010$ from Fig. 10.7. Finally, for $\Delta = 0.5$ the growth rate measured for the linear case, $a_{\mathrm{eff}} = 0.00732$, gives the predicted wave front velocity $v_{\mathrm{wf}} = 0.415$. Again, the value $v = 0.412$ measured in Fig. 10.7 agrees well with the prediction of Eq. (10.4).

Appendix A

Random Field Ising Model Simulation Code

The RFIM simulation code is based upon code available on the web [123]. In all cases a sorted list algorithm was used which stores the random fields. This algorithm as well as the implementation of the base code has been described in depth in Ref. [93]. The following will thus concentrate on the extensive changes made to the code. The changes involve a reworking of the interface with the introduction of new types of field histories, an optimized sorted list algorithm, and a new avalanche algorithm to allow reverse flips in the presence of demagnetizing fields. The revised code has been made available at the Materials Computation Center software repository [124].

A.1 Interface

The web code comes with a "point and click" Microsoft Windows interface as well as a console interface. As the code was to be used for long running batch jobs on computing clusters and other machines (running Unix variants), the Windows interface was not used. The console interface, which may be run interactively or from input files, had one major problem. The interface was based upon the an associative mapping of commands to call back functions, the latter of which were all placed into a single file. These functions controlled the entire simulation including the setting of parameters, driving the simulation via manipulation of the external field, and saving the resulting data. For the saturation loop this is not a large problem as one simply must increase the field and take the data at the same time. However, as field history is taken into account, with a large number of subloops, the complexity of the problem increases rapidly. Additionally, with the introduction of more algorithms and flags for measuring various features, the interface quickly became a morass of code in which it became relatively easy to set starting parameters that were inherently conflicting resulting in an immediate program crash.

The problems with the interface is contrasted by the rest of the code which is built in a object oriented fashion in C++. To bring the problems under control and have the interface be in the spirit of the rest of the code base, a new interface with a modular design was developed. Three specific goals drove the redesign. First, the flexibility of either a simple interactive text or input file interface was desired for the ease of running batch jobs. Furthermore, the new interface needed the ability to prevent and catch inaccurate configurations before running the simulations. Finally, it was important to be able to add new options or features with relative ease while still keeping the strict checking of the previous goal.

These goals were met by implementing the interface using a modular tree framework. For simplicity the associative map was kept at the lowest level to drive the interface. The call back functions were changed however. Instead of being able to randomly change simulation features, the functions now force one to operate in a tree like hierarchy. This involves first choosing a so called simulation module, for example to perform AC demagnetization. The demagnetization module then adds its dependent parameters to the list of available options. These options in turn may do the same. Each option may be set, have the current value printed, or print a help text.

While this method is not necessarily optimal and could be improved, it does satisfy the goals given above. Looking to the future, which would ideally have similar ideas applied in merging the console and windowed based interfaces into one, the various modules and algorithms have been made to be easily extended. The implementation and use of the two modules used for the majority of simulations described in Chs. 4 and 5 follows.

A.1.1 General Commands

In any of the simulations, a large number of commands are shared between the modules and algorithms. All commands are entered via a command line or from an input file. The order of these commands is important as for example changing the simulation module will reset some parameters. General commands shared by all the modules are "help", "setup", and "quit" which have self explanatory actions. The "algorithm" command allows one to chose the underlying Hamiltonian, with or without long range forces, and the way avalanches are produced in the simulation. Available options are sorted list, brute force, bits[1], infinite range, and dipole algorithms. Note that not all algorithms are appropriate for some modules and are thus disallowed. Lastly, the general simulation parameters are also common options, including the dimension, disorder, random seed, system length, disorder precision, and random distribution type which are set via the commands "d", "r", "seed", "l", "df", and "dist" respectively. Finally, a number of simulations my be run in sequence by using the "run" command.

A.1.2 Demagnetization

To analyze the demagnetization curve as found in Ch. 4, one chooses the demagnetization module via the command "module 2". This module is implemented atop the sorted list algorithm, and so no other algorithms are available. Several demagnetization modes may be chosen with the "dmode" command. These include an exact demagnetization starting from either saturated state, and also an inexact demagnetization with a step size $\Delta H = 0.001$. In the latter case the simulation is started from saturation with the field strength decreasing by ΔH after each oscillation, as in a typical AC demagnetization, and stopped when the field strength reaches zero or no more avalanches occur. For exact demagnetization the field is only reduced enough on each subloop to prevent the last avalanche of the subloop from occurring. To accomplish this, the state of the simulation is saved before every avalanche. Upon performing a field increase and the resulting avalanche, if the avalanche returns the system to the starting point of the last subloop, then the saved state before this last avalanche is restored, leaving the system just before this last avalanche. The direction of field change is then reversed and the process continued until there are no more avalanches.

---

[1] These first three algorithms are described in detail in Ref. [93].

Several types of outputs are available during the simulation and may be set with the "actions" command. In particular, the command is given as "actions o t -1" followed by 16 "+" or "-" signs which turn on and off various outputs. These outputs are the demagnetization curve, time series, size distribution, correlation function, dM/dH, spanning avalanches, average size distribution, average correlation function, average spanning avalanches, subloop spanning avalanches, size distribution moments, average size distribution moments, output toggle, demagnetized state, jump in magnetization, and average jump in magnetization. Here "average" denotes averaging a quantity over several configurations of random fields, the number of which the "run" command has specified. To receive any output besides saving the demagnetized state, the output toggle must be set to "+". By saving the demagnetized states, data may be taken for the demagnetization curve at a later time by using the "ic 2" command. Following this command with a filename of a saved state, with the simulation parameters set as they were when the state was produced, will then allow one to run the demagnetization curve again when the "run" command is issued. Finally, a similar command, "ic 3", without any filename will output the system's spin state after the last spanning avalanche, or largest avalanche, along both the upper and lower halves of the demagnetization curve. For this there must be demagnetized states saved according to the simulation parameters that are currently entered.

A.1.3 Subloops

To obtain the concentric, symmetric subloops found in Ch. 5 a separate module was used, an arbitrary history module chosen by the command "module 1". As the module name implies, not only may concentric, symmetric subloops be simulated, but in fact any arbitrary field history path. This is accomplished by inputing an arbitrarily long list of field or magnetization points at which the field will be reversed. They are entered via the "sbp x y ..." command where the "x" is replaced by "0" or "1" denoting whether the points start along the lower or upper saturation curve respectively. The variable "y" gives the number of branch points, where the field direction reverses. The list of points follows. Whether these points are in units of field or magnetization is chosen via the "sbpu" command.

Given the list of branch points, the program then computes the field history, dividing the hysteresis branches, the curve between two branch points, into subloops. This is accomplished by recognizing that when the field is reversed at a given branch point there are two possible outcomes. Either a new subloop is started with the branch possibly completing other subloops, or the second branch of the current subloop is started after possibly completing other subloops. Which situation applies is determined by examining the field value of the branch point under the assumption of return-point memory. When a subloop is closed one returns to the previous subloop. Thus a stack is the natural choice to keep track track of the current subloop. In describing the algorithm, shown schematically in Fig. A.1, when comparing two field values the

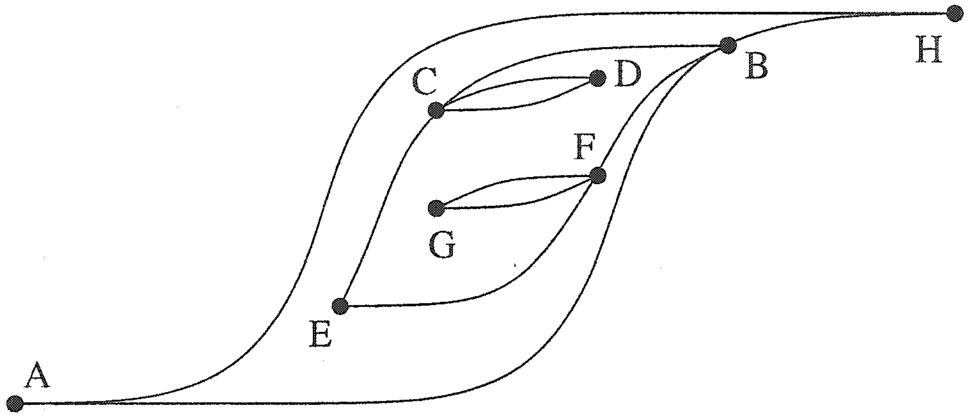

Figure A.1: Schematic of the subloop detection algorithm obtained from inputing six branch point along the increasing side of the saturation loop via the "sbp" command. The branch points B, C, D, E, F, and G are entered and the algorithm automatically adds in the A and H points corresponding to the saturated states. Branch points B, D, and F are detected as new subloop starting points while points D, E, and G are detected as subloop reversal points. The four subloops are AH (the saturation loop), BE, CD, and FG. Branches that span several subloops, such as branch GH, are automatically broken up by the algorithm into smaller branches (GF, FB, and BH) to allow for per subloop data collection.

terms "greater" and "less" will imply a dependence on the current direction of field increase. So for example if the previous branch had a field 0 and the current branch a field 1, then the field is increasing and a value 2 would be greater and a value −1 would be less than the field value 1. On the other hand if the previous branch was at a field 1 and the current branch at 0 then the field is decreasing and the value −1 would be greater and the value 2 would be less than the field 0. The algorithm begins by first checking if the field of the current branch point is greater than the starting field of the current subloop. If so then the subloop is closed and popped off the stack with the analysis restarted for the new current subloop. Branch DE in Fig. A.1 is such a case. Next, if there is a later branch point with a field value greater then the current point before there is one with a field value less than the starting point (or reversal point if already past it) of the current subloop then the current field reversal starts a new subloop, as seen in Fig. A.1 for branch point C. The new subloop is then pushed on the stack. Finally, if the opposite is true, namely a later branch point with a field value less than the subloop starting point is found first, such as for branch point E in Fig. A.1, then this point marks the reversal point of the current subloop and the second half of the current subloop is started.

Upon setting the branch points with the "sbp" command, a list of the subloops are printed. It is then possible to setup the various analysis tools on a per subloop basis by using the "actions" command. The command has a similar form as in the demagnetization module. In particular, "actions o t # ...", chooses to output calculations for entire subloops where "#" is replaced by either a subloop number or "-1" to apply to all subloops. The 16 possible actions are then chosen using the "+" or "-" as described previously. The actions output the hysteresis curve, time series, size distribution, correlation function, dM/dH, spanning avalanches, average size distribution, average correlation function, average spanning avalanches, average derivatives, size distribution moments, average size distribution moments, nucleation points, domain walls, jump in magnetization, and average jump in magnetization respectively. The magnetism value at which to output the domain walls, if this output is chosen, is set using the "dwm" command.

Note that when return-point memory is broken, such as is the case when anti-ferromagnetic terms appear in the Hamiltonian, the picture of well defined subloops also breaks. However if there is still approximate return-point memory, the picture of subloops is still sufficient for analyzing the avalanche behavior. Although it has not been implemented, the simulation code is set up so that it would be possible to easily extend the data collection for smaller subsets of the subloops, whether for the upper or lower half of subloops or on a per branch basis.

There are several other specialized commands. First, "islb" sets a check for the system to see if subsequent subloops are identical and if so to then exit from the simulation. This can be useful when working at low disorders where there is a large irreducible kernel of spins or for checking the number of reptations, the number of different subloops consecutively produced while sweeping between fixed field values [50; 125; 126], when anti-ferromagnetic terms are present. When the infinite range algorithm is used, which provides mean-field anti-ferromagnetic interactions, several other parameters are available. The long range coupling constant is set using the command "jlr". The command "dwprop" toggles whether domain wall propagation is required as opposed to also allowing avalanches to nucleate ahead of domain walls. Finally, the initial conditions of the system may be chosen with the command "ic #" where "#" is "0" to start with a saturated state or "1" to start with a predefined domain wall.

A.2 Search Algorithm

The sorted list method uses a search algorithm to find the field value that will flip the first spin, or seed of an avalanche. This algorithm is based on a list of pointers, here denoted nextSpin[n], which point (into a list of spins sorted by random field) to the next spin which would flip if it had n neighbors up. Here n can run from 0 to z, the coordination number of the lattice. In the base code implementation [123] a simple loop algorithm is used to the find the seed of the avalanche. The nextSpin pointers are scanned for the spin with the largest effective local field and the pointer for that value of n is then incremented. If the spin's real number of neighbors up was equal to the value of n and the spin had not already been flipped then that spin is the seed of the next avalanche [93]. The inefficiency of the implementation of this algorithm arises in that each time through the loop only one pointer is incremented, but all the local fields must be compared to find the maximal value. After a large avalanche, many spins have been flipped and so to find the next spin to seed an avalanche the nextSpin pointers must be incremented over all these newly flipped spins. Thus the many comparisons of the local fields performed in each loop are wasted. Of course for small or single spin avalanches the algorithm is still quite efficient.

The examination of demagnetization curves and subloops in Chs. 4 and 5 occurred at disorders close to the critical point where very large avalanches are present. Thus the search algorithm was optimized to deal more efficiently with these large events. In particular the idea of the nextSpin pointers was kept, but the looping algorithm was replaced with a linear search algorithm. The new algorithm is as follows. The previous avalanche caused the field to increase, so the nextSpin pointers are first incremented up to the new point where the effective local fields first cause an unflipped spin to be unstable and also incremented past any spins that have already been flipped. The positions of the nextSpin pointers are then saved. Next each nextSpin pointer is incremented in turn, starting with $n = 0$, until it points to an unstable spin, reaches the minimum field value for which a previous nextSpin pointer found an unstable spin, or runs out of unflipped spins. At this point the unstable spin that requires the smallest increase in field becomes the seed of the next avalanche. Finally all nextSpin pointers with n less than the avalanche seed's number of up neighbors are reset to their saved values. This last step is required as incrementing the nextSpin pointers may have them pointing to a position corresponding to a field value larger than was chosen for the avalanche. This is not required for the pointers with n greater than the seed spin's number of up neighbors as the algorithm incremented these pointers only up to the field that made the seed spin unstable.

This new search algorithm resulted in roughly a $10 - 20$ percent decrease in the computation time for the disorders simulated in Chs. 4 and 5. However, improvements still could be made. While the new algorithm is much more economical for large avalanches, unlike the original algorithm it is inefficient for small avalanches. This arises due to incrementing the nextSpin pointer many more times during the linear search for the unstable spins. Therefore by combining the two into a hybrid algorithm it may be possible to further increase the search algorithm's efficiency.

A.3 Back-Flip Algorithm

After finding the seeding spin for an avalanche, the avalanche is propagated using a queue method that flips spins in successive "shells" [93]. This provides a natural spin-flip order as all spins in a given shell are flipped before checking to see if their nearest neighbors (in the next shell) are induced to flip as well. A difficulty arises when long range anti-ferromagnetic forces as found in Ch. 6 are added ($J_{LR} > 0$). As the number of spins flipped increases, the change in magnetization may increase the demagnetization field enough to cause spins to flip opposite the direction of the field increase (back-flip) and also to prematurely stop the avalanche (as compared to the $J_{LR} = 0$ case). Hence a revised algorithm for avalanche propagation is required. At its heart, the shell method is still used so that a physical order of spin flips is preserved. Now, however, as the demagnetizing field may reduce the effective field enough to stop an avalanche in the middle of a shell, the order of spin flips within shells is important. In particular, the most unstable spin is flipped first, be it with or against the direction of field increase.

The code available on the web [123] implemented the above modified shell method, but neglected the possibility of back-flips. To allow for backward flipping spins it is first useful to analyze the requirement for such an event to take place. First it is assumed that at the start of an avalanche (or equivalently the end of the previous avalanche) all spins are aligned with their local field and are thus stable. Then for a spin to back-flip, the change in magnetization ΔM, the current size of the avalanche, must be large enough to cause the local effective field to change its sign through the effect of the demagnetization field. An approximation to this condition is for the local field to simply be smaller in magnitude than at the start of the avalanche, which requires

$$\Delta M > (\Delta H + 2\Delta n)/J_{LR} \tag{A.1}$$

where ΔH is the amount of increase in the field and Δn is the site dependent change in number of up neighbors.

From Eq. (A.1) two useful criteria may be obtained. First, assuming a spin is not next to the current avalanche, $\Delta n = 0$ and one must have $\frac{\Delta M}{\Delta H} > 1/J_{LR}$ before the spin might back-flip. This allows one to use the simpler (and faster) avalanche algorithm which neglects back-flips until ΔM becomes large enough that this relation becomes true. Furthermore, ΔM has a maximum value of one, corresponding to an avalanche flipping the entire system. For the relatively small values of J_{LR} examined this means that if a spin is in or next to the current avalanche then it will not back-flip during the avalanche since it has $\Delta n \geq 1$ and thus the right hand side of Eq. (A.1) is greater than one. Note that this argument breaks down once $J_{LR} \geq 2$. The long range behavior of the demagnetizing field is evident here as the back-flips must occur away from the current avalanche.

Due to the relation found in the previous paragraph which says that for small ΔM no back-flips may occur, the avalanche propagation algorithm starts out using the modified shell method described above except any spins in a shell that are not flipped are put on a reject queue. After completing each shell the criteria (Eq. (A.1) with $\Delta n = 0$) is rechecked. If the relation now becomes valid, then the following back-flip algorithm begins.

First the system is checked for spins that are ready to flip backwards. If the total change in magnetization of the avalanche at this point is positive and the change in magnetization of the last shell also was positive then the lattice is searched for spins which have negative local fields but are flipped upwards. This is done by decrementing the nextSpin pointers until stable spins are reached, with the nextSpin pointers restored to their original values after the search. In this way only a portion of the lattice must searched. If spins ready to flip backward were found then they are placed in the queue for the next shell. On the other hand, if the change in magnetization of the last shell was negative, then one must search for spins now ready to flip upwards due to the decrease in the demagnetization field. This is quite simple in that the only spins which may now flip up are ones that were checked in an earlier shell but did not flip then due to the size of the demagnetization field. Thus one simply scans through the reject queue, which contains all these rejected spins, and adds to the queue for the next shell any spins that are ready to flip upwards. Finally, if the total change in magnetization of the avalanche at this point is negative, then the above two situations are simply reversed. For a positive change in magnetization for the last shell the reject queue is searched for spins ready to flip backwards. On the other hand a negative change in magnetization for the last shell results in searching the lattice, via the nextSpin pointers, for spins ready to flip upwards. After using the above methods to find possible back-flipping spins, the spins of the next shell are then checked and flipped as before, always choosing to flip the most unstable spin in the queue regardless of the flipping direction. Again, spins on the queue which do not flip are put on the reject queue and once the shell is complete then one starts over checking for spins ready to back-flip.

Appendix B

Spreading Simulation Code

The spreading simulation code was used to investigate the growth of bacteria in random environments with large convection velocities as detailed in Chs. 8-10. In particular, it was necessary to solve the differential equations describing the bacterial growth and spreading for times $t > 0$ given an appropriate initial condition. A simple Runge-Kutta scheme [127] was used to propagate the solution forward in time, with finite difference methods providing the necessary lattice derivatives. The random growth rates found in the differential equations were obtained using code from the random number generator found in the GNU C library [128]. This provides a portable, nonlinear additive feedback random number generator with a period on the order of 2^{35} which was sufficient for the simulations performed. In the following sections the specifics of each implementation will be described.

B.1 1-D Code

The simplified equation, Eq. (9.1), was simulated in one spatial dimension, x. This dimension was discretized and the standard finite differencing was used for the terms of Eq. (9.1), namely

$$v\partial_t W(t)_i = \frac{D}{l_x^2}\left(W(t)_{i+1} - 2W(t)_i + W(t)_{i-1}\right) + U(t)_i W(t)_i. \qquad \text{(B.1)}$$

The lattice contained 20000 sites. This was large enough to ensure that even for the longest times, 5 million time steps, the solution did not experience the periodic boundary conditions. One complication arises in Eq. (9.1), the fact that the random growth rates $U(x,t)$ depend on the time. This means that the growth rates must be updated constantly during the simulation. To insure that the lattice constants for the time and space were equal, $l_x = l_t$, a Runge-Kutta step size of 0.1 was chosen and the random growth rates were then updated after every ten time steps.

Simulations began with a Gaussian initial condition of unit variance centered on the lattice. This Gaussian was obtained from the same code started with a Kronecker delta function at $t = 0$ and $x = 10000$ and run for twenty time steps with no random growth rates. Finally, to speed up the algorithm, a minimum cutoff $c_{\min} = 10^{-23}$ was arbitrarily imposed. After each time step the profile was normalized by the total population greater than this cutoff with points below set to zero. For the longest times simulated, this procedure did not affect the widths of the concentration profiles as compared to that calculated with full floating point precision which has an effective cutoff of approximately 10^{-45}. The cutoff concentration profiles were nearly identical to those without a cutoff imposed, with deviations only occurring on the edges of the profiles when the concentration became on the order of 10^3 the cutoff size. This cutoff resulted in over a tenfold reduction in the real-time required for each simulation.

B.2 2-D Code

The full reaction-diffusion equation, Eq. (10.1), was simulated both with only the linear growth term included, $b = 0$, and with the nonlinear growth term included, $b > 0$. Due to the differences induced from the additional term, each case required a slightly different simulation code as describe below. Nevertheless, the majority of the code was similar. Regardless of the value of b, the code used a finite differencing scheme as follows. The two spatial dimensions were placed on a triangular lattice which reduces the error in calculating the Laplacian operator [110]. The three lattice directions $\hat{x}_1$, $\hat{x}_2$, and $\hat{x}_3$ are oriented at angles of 0, $\pi/3$, and $2\pi/3$ with respect to the positive x axis. There are several ways in which finite differencing may be applied to Eq. (10.1), depending on the treatment of the convection velocity term. The naive approach is to simply use the standard second order differencing scheme which along the $\hat{x}_2$ direction, for example, takes the form, $\frac{v}{2\sqrt{3}l_0}(c_{\vec{x}-\hat{x}_2} - c_{\vec{x}+\hat{x}_2})$. This leads to

$$\begin{aligned} \partial_t c_{\vec{x}} &= \frac{2D}{3l_0^2}\left[c_{\vec{x}+\hat{x}_1} + c_{\vec{x}-\hat{x}_1} - 6c_{\vec{x}} + \sum_{i=2}^{3}\left(\left(1-\frac{g\sqrt{3}}{2}\right)c_{\vec{x}+\hat{x}_i} + \left(1+\frac{g\sqrt{3}}{2}\right)c_{\vec{x}-\hat{x}_i}\right)\right] \\ &\quad +(a+U_{\vec{x}} - bc_{\vec{x}})c_{\vec{x}}, \end{aligned} \tag{B.2}$$

where $g \equiv vl_0/2D$. For small convection velocities, or very small time increments, this differencing scheme is stable. However, a large velocity, or equivalently a large g, is desired to ensure that the bacterial colony is delocalized. When v is large the first term of Eq. (B.2) may become negative. At the trailing edge of the droplet $c_{\vec{x}-\hat{x}_i} > c_{\vec{x}+\hat{x}_i}$ for $i = 2, 3$ and thus the concentration may be decreased by a large amount, leading to strange behaviors in the concentration profile. This behavior is also unphysical, as in the bacterial colony the effect of the drift current should not kill off population. To rectify the situation, a modified differencing scheme is used to model the drift current. It is based on an Anderson tight binding model [119] from quantum mechanics and was proposed as an appropriate differencing scheme in Ref. [114]. The scheme has the form,

$$\begin{aligned} \partial_t c_{\vec{x}} &= \frac{2D}{3l_0^2}\left[c_{\vec{x}+\hat{x}_1} + c_{\vec{x}-\hat{x}_1} - (2+4\cosh(g\sqrt{3}/2))c_{\vec{x}} + \sum_{i=2}^{3}\left(e^{-g\sqrt{3}/2}c_{\vec{x}+\hat{x}_i} + e^{g\sqrt{3}/2}c_{\vec{x}-\hat{x}_i}\right)\right] \\ &\quad +(a+U_{\vec{x}} - bc_{\vec{x}})c_{\vec{x}}. \end{aligned} \tag{B.3}$$

Note that expanding the exponentials in Eq. (B.3) to first order in v recovers Eq. (B.2). Hence for small velocities the schemes are identical. For large velocities Eq. (B.3) does remove the unphysical behavior found in Eq. (B.2). Unfortunately it also introduces an additional difficulty.

For a good differencing scheme one would like v to be the true convection velocity in the lattice. However, due to the nonlinear exponential in Eq. (B.3), v no longer represents the true convection velocity. This leads to interesting behavior such as a doubling of v simultaneously increasing the effective rate of convection by more than a factor of two as well as increasing the effective diffusion constant in the $\hat{x}_{2,3}$ directions. So not only is the velocity different than one expects, but the droplet also spreads asymmetrically. For a differencing scheme of the form

$$\partial_t c = A_0 c_{\vec{x}} + \sum_{i=1}^{3} (A_i c_{\vec{x}+\hat{x}_i} + B_i c_{\vec{x}-\hat{x}_i}), \tag{B.4}$$

the effective convection velocity along the $\hat{x}_i$ direction is given by $(B_i - A_i)l_0$ and the effective diffusion constant by $3(B_i + A_i)l_0^2/4$. Applying this to Eq. (B.3) yields $v_{\text{eff}} = 4D\sinh(\sqrt{3}g/2)/\sqrt{3}l_0$, obtained by adding the velocities along the $\hat{x}_{2,3}$ directions, and $D_{\text{eff}} = D\cosh(\sqrt{3}g/2)$. Thus, increasing the parameter v increases both the effective convection velocity and effective diffusion constant. As mentioned in Sec. 8.1, one would like the parameter $g = v/2D$ to be large enough to be in the delocalization regime. The differencing scheme in Eq. (B.3) gives $g_{\text{eff}} = 2\tanh(\sqrt{3}g/2)/\sqrt{3}l_0$. But this means that $\lim_{v\to\infty} g_{\text{eff}} = 2/\sqrt{3}l_0$. No matter how large v is made, the true ratio of the velocity to diffusion constant will remain small even though it is desired to have a large value for this ratio. To deal with the problem, the limit $g \to \infty$ is taken so that g_{eff} takes on its largest possible value. However, now v_{eff} and D_{eff} are divergent. One desires these quantities to be finite, so the parameter D, for the $\hat{x}_{2,3}$ directions, is recast as $2De^{-\sqrt{3}g/2}$. The $\hat{x}_1$ direction contains no convection and so is unaffected. Applying this procedure to Eq. (B.3) yields the following differencing scheme,

$$\partial_t c_{\vec{x}} = \frac{2D}{3l_0^2}\left[c_{\vec{x}+\hat{x}_1} + c_{\vec{x}-\hat{x}_1} + 2c_{\vec{x}-\hat{x}_2} + 2c_{\vec{x}-\hat{x}_3} - 6c_{\vec{x}}\right] + (a + U_{\vec{x}} - bc_{\vec{x}})c_{\vec{x}}. \tag{B.5}$$

There remain four adjustable parameters, D, U, a, and b. To simplify the required calculations $D = 3/4$ was chosen. Now the convection velocity is fixed at $v = 4D/\sqrt{3} = \sqrt{3}$ and so to insure a delocalized system the width of the random growth rates must be adjusted appropriately. Unlike in Sec. B.1 this means that only the random growth rates may be adjusted to test the diffusive behavior of the system. A good consequence of the limit taken in Eq. (B.5) is the reduction by two in the number of terms one must compute for each lattice point, thus reducing simulation times. Effectively, the velocity is so large that only points adjacent to or trailing the current position may contribute to the change in concentration.

Allowing the droplet of bacteria to grow without experiencing the influence of the periodic boundary conditions was accomplished in the one-dimensional case, Sec. B.1, by using a sufficiently large number of lattice points. It is similarly desirable to allow the droplet to spread in two dimensions without experiencing the boundaries of the simulation, so that it appears to the droplet that it is in an effectively infinite system. A problem arises in that the droplet is not fixed in position as in Sec. B.1. Rather it moves through the system in the y direction a distance $y_d = v_{\text{eff}}t$ in time t. Clearly for any large time scale y_d will be very large and an inordinate number of lattice sites would be needed if the entire lattice was fixed beforehand. To avoid this situation, a sliding simulation box was used. In the x direction, perpendicular to the convection, a fixed length of 10000 sites was chosen, sufficient to ensure the spreading would not reach the boundaries in this direction for the times investigated. The droplet was then allowed to travel down a tube of lattice sites along the y direction. Due to the triangular lattice this means the edges of the simulation box were in a zigzag pattern. The simulations were started with a point concentration, one or the carrying capacity for the linear and nonlinear cases respectively, at the site $(5000, 0)$. The simulation box was given a fixed length in the y direction and when the droplet reached the edge of the box the box was then shifted farther along in the y direction. This is possible only because the system is delocalized. There is no concentration remaining behind the droplet and so those lattice sites may be dropped from the simulation.

B.2.1 Linear vs. Nonlinear Growth

To simulate Eq. (10.1) with only linear growth, $b = 0$ and $a = 0$ were set. The situation ends up being similar to that of the one-dimensional simulation. A cutoff of 10^{-15} was chosen, and as the system also experiences enhanced growth, the concentration was normalized after every time step by the total population above the cutoff. The case of nonlinear growth was treated differently. The parameters were set to $b = 0.1$ and $a = 0.05$ giving a carrying capacity of $a/b = 0.5$ and as before a cutoff of 10^{-15} was chosen. Due to the Fisher-like wave produced, inside there is a constant average concentration, the carrying capacity, and the total population is not normalized. Instead it was allowed to grow uninhibited. Normalizing would artificially decrease the concentration inside the wave front below the carrying capacity thus changing the dynamics.

Appendix C

Experimental Noise Determination

The Barkhausen noise measurements on the soft ferromagnet described in Ch. 2 were taken using a pick-up coil. This provides a voltage versus time curve that contains the noise arising from Barkhausen jumps. A piece of such a curve is shown in Fig. C.1. Theoretically, to obtain the avalanche size distribution such as are shown in Fig. 2.2, one must simply determine the area under each pulse in the voltage curve times a physical factor dependent on the coil. However, in practice problems arise in this process due to various instrumentation factors. These include offset voltages, the discretization of analog to digital (AD) converters, and instrumental noise. Previous

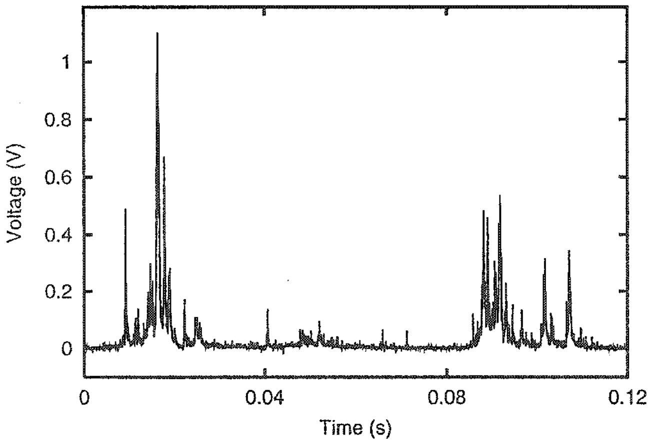

Figure C.1: Barkhausen noise as measured from the pick-up coil voltage for a portion the largest loop shown in Fig. 2.2.

experiments have overcome these problems by imposing a minimum voltage below which all data is set to zero. This voltage is slowly increased until the resulting avalanche size distributions do not show a large bump at small sizes due to noise, but instead have a power-law slope [129]. As this procedure appears to be somewhat biased in the removal of noise from the data, a more quantitative process for noise removal was developed.

First an appropriate voltage offset level must be determined as a baseline for calculating avalanche sizes. One could simply visually choose a particular region that appears to be devoid of avalanches and thus determine the voltage level from the average of the noise at that spot. However, the experimental voltage curves typically contain over 10^5 points and it is desirable to average over a number of sections to reduce the errors arising from fluctuations. This quickly becomes untenable for a visual inspection and so an automated process is required. The difficulty arises in how to automatically differentiate between regions with small avalanches and those devoid of avalanches. Examining the power spectrum, the moduli of the discrete Fourier transform [130], for a section of the voltage trace resolves the problem. In a region devoid of avalanches, the fluctuations in the voltage come from instrumental noise and the offset voltage falling in between the discretization steps of the AD converter. These should produce white noise and thus the power spectrum should be flat. On the other hand, avalanches have been shown to exhibit a power-law in their power spectra which clearly will not appear flat. A final possibility is noise arising from thermal fluctuations in the sample, which has been shown to have a voltage power spectrum linear in the frequency [131]. While this case could also be differentiated from white noise, due to large energy barriers in the measured sample the thermal fluctuations were negligible.

Using the above information, the following procedure was applied to obtain the baseline voltage. First, the voltage traces were examined to find a typical distance

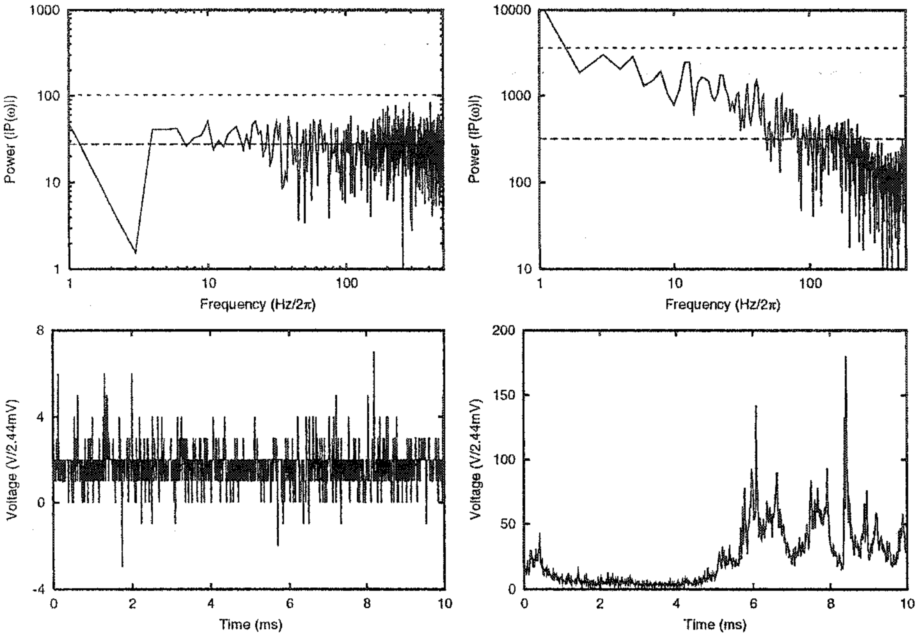

Figure C.2: Noise window power spectra (top) with corresponding voltage traces (bottom) for the largest loop shown in Fig. 2.2 with the mean and five sigma distance shown as a dashed line and dash-dot line respectively. On the left the spectrum is flat and the window acceptable while on the right it is not, due to the presence of avalanches in the window.

between avalanches. This distance was then taken to be the window size on which the power spectra would be computed. Note that for the procedure to apply one must sweep the field at a sufficiently slow rate in comparison to the voltage sample rate to provide a reasonable distance between avalanches. For the sample measured in Ch. 2 this window was 1024 time steps which corresponds to 10.24 ms. A determination of the "flatness" of the power spectra was made using the mean and standard deviation of the power. If the power at any frequency fell 5 or more standard deviations from the mean then the window was deemed to contain avalanches. Note that the zero frequency is not included as this contains the offset voltage itself. If the window was acceptable, then the average voltage level was determined. An example of this calculation is shown in Fig. C.2 with the left plot showing an acceptable window and the right plot a window with avalanches.

This procedure is applied to the entire train of avalanches by sliding the window

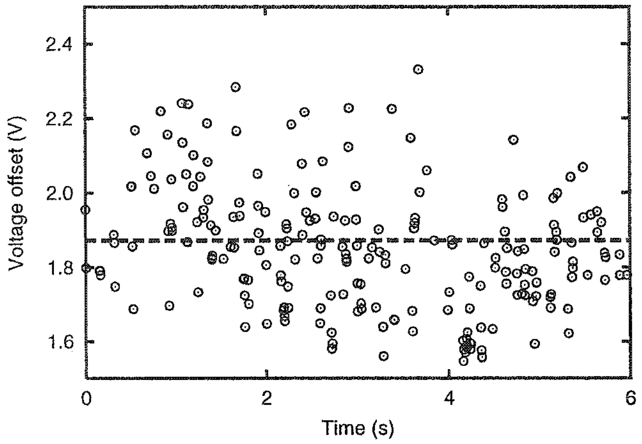

Figure C.3: Voltage offsets for acceptable windows from a measurement of the noise in the largest loop shown in Fig. 2.2. The dashed line shows a constant fit to the levels giving an offset voltage of 1.872 ± 0.050V.

along by approximately half the window width, 5 ms. This is to allow for more windows to be "good", since the small avalanches do not necessarily line up on the same spacing as the initial window width. Figure C.3 shows the resulting voltage levels for one measurement of the largest loop shown in Fig. 2.2. Out of 1200 possible windows, 217 were found to be acceptable. While the levels in Fig. C.3 fluctuate, the offset is roughly constant. Due to the fluctuations, a visual inspection of only a few points might come to the conclusion that there is a nonconstant offset, but the automated procedure avoids this error. The voltage offset was then determined by fitting a constant to the measured levels with the quoted error equal to three times the asymptotic standard error of the fit value. This is shown as a dashed line in Fig. C.3.

With the offset voltage determined, it is now simply a matter of calculating the avalanche sizes from the voltage trace. This is done by determining the area between the voltage trace and the offset voltage. The end, or equivalently beginning, of an avalanche is determined when the voltage trace crosses the offset. The avalanches are binned according to size, with positive and negative sizes kept in two separate distributions. These are then plotted and the two distributions compared, as shown

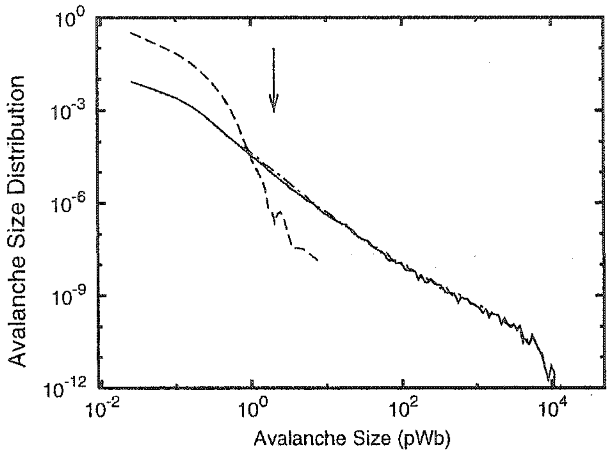

Figure C.4: Avalanche size distributions for positive (solid line) and negative (dashed line) avalanches measured on the largest subloop shown in Fig. 2.2 and averaged over 8 measurements. The dash-dot line, which falls on top of the positive avalanche line, shows the avalanche size distribution calculated using an arbitrary voltage cutoff. An arrow at 2pWb indicates the point where the solid line is free of noise.

in Fig. C.4. The negative avalanches arise from the noise present as well as from any negative avalanches in the system. The latter are rare if present at all. With the correctly chosen voltage offset, there should be an equal amount of noise above and below the offset, thus the sharp drop off in the negative avalanche distribution indicates the point at which the noise drops out of the measured positive avalanche distribution. Therefore the avalanche size distribution above roughly 2pWb is free of noise. Also shown in Fig. C.4 is the distribution that would result from employing the cutoff voltage technique of Ref. [129] described above with a cutoff voltage of 3V. It results in a smallest avalanche size roughly equal to that calculated from the negative avalanches, although some fluctuations for the smallest sizes have been removed. Smaller sizes fluctuate more than the latter calculation. Another drawback to the technique of Ref. [129] is the loss of the negative avalanches resulting from Barkhausen events. Although there are relatively few of these events, Fig. C.4 clearly shows that some were detected in the experiment.

References

[1] P. J. Cote and L. V. Meisel, Phys. Rev. Lett. **67**, 1334 (1991).

[2] S. Field, J. Witt, F. Nori, and X. Ling, Phys. Rev. Lett. **74**, 1206 (1995).

[3] W. Wu and P. W. Adams, Phys. Rev. Lett. **74**, 610 (1995).

[4] E. Vives, J. Ortín, L. Mañosa, I. Ràfols, R. Pérez-Magrané, and A. Planes, Phys. Rev. Lett. **72**, 1694 (1994).

[5] J. P. Sethna, K. Dahmen, S. Kartha, J. A. Krumhansl, B. W. Roberts, and J. D. Shore, Phys. Rev. Lett. **70**, 3347 (1993).

[6] P. Cizeau, S. Zapperi, G. Durin, and H. E. Stanley, Phys. Rev. Lett. **79**, 4669 (1997).

[7] J. D. Murray, *Mathematical Biology* (Springer-Verlag, New York, 1993).

[8] A. J. Koch and H. Meinhardt, Rev. Mod. Phys. **66**, 1481 (1994).

[9] K. A. Dahmen, Ph.D. thesis, Cornell University (1995).

[10] A. Berger, A. Inomata, J. S. Jiang, J. E. Pearson, and S. D. Bader, Phys. Rev. Lett. **85**, 4176 (2000).

[11] G. Bertotti, *Hysteresis in Magnetism* (Academic Press, 1998).

[12] F. Liorzou, B. Phelps, and D. L. Atherton, IEEE Trans. Magn. **36**, 418 (2000).

[13] M. Pardavi-Horvath, J. Oti, G. Vertesy, L. H. Bennett, and L. J. Swartzendruber, J. Magn. Magn. Mater. **104-107**, 313 (1992).

[14] F. Preisach, Z. f. Physik B **94**, 277 (1935).

[15] V. Basso, IEEE Trans. Magn. **34**, 2207 (1998).

[16] D. R. Comejo, M. L. Bue, V. Basso, G. Bertotti, and F. P. Missell, J. Appl. Phys. **81**, 5588 (1997).

[17] J. B. Restorff, H. T. Savage, A. E. Clark, and M. Wun-Fogle, J. Appl. Phys. **67**, 5016 (1990).

[18] D. Hughes and J. T. Wen, Smart Mater. Struct. **6**, 287 (1997).

[19] G. Friedman, L. Liu, and J. S. Kouvel, J. Appl. Phys. **75**, 5683 (1994).

[20] L. A. L. de Almeida, G. S. Deep, A. M. N. Lima, H. F. Neff, and R. C. S. Freire, IEEE Trans. Instrum. Meas. **50**, 1030 (2001).

[21] E. König, B. Kanellakopulos, B. Powietzka, and J. Nelson, J. Chem. Phys. **99**, 9195 (1993).

[22] A. H. Wootters and R. B. Hallock, J. Low Temp. Phys. **121**, 549 (2000).

[23] M. P. Lilly and R. B. Hallock, Phys. Rev. B **63**, 174503 (2001).

[24] I. D. Mayergoyz, *Mathematical Models of Hysteresis* (Springer-Verlag, New York, 1991).

[25] A. Ktena, D. I. Fotiadis, and C. V. Massalas, IEEE Trans. Magn. **36**, 3926 (2000).

[26] O. Henze, W. M. Rucker, M. Jesenik, V. Goričan, M. Trlep, A. Hamler, and B. Štumberger, IEEE Trans. Magn. **39**, 1151 (2003).

[27] F. Ossart, T. A. Phung, and G. Meunier, J. Appl. Phys. **67**, 5379 (1990).

[28] S. Seeck and M. Lambeck, J. Appl. Phys. **78**, 5577 (1995).

[29] A. Ktena, D. I. Fotiadis, and C. V. Massalas, J. Appl. Phys. **87**, 4780 (2000).

[30] S. F. H. Parker, C. A. Faunce, P. J. Grundy, M. G. Maylin, J. L. C. Ludlow, and R. Lane, J. Magn. Magn. Mater. **145**, 51 (1995).

[31] J. Ortín, J. Appl. Phys. **71**, 1454 (1992).

[32] G. Friedman, Physica B **275**, 173 (2000).

[33] D. C. Jiles and D. L. Atherton, J. Magn. Magn. Mater. **61**, 48 (1986).

[34] D. C. Jiles, J. B. Thoelke, and M. K. Devine, IEEE Trans. Magn. **28**, 27 (1992).

[35] N. L. Mi, R. Oruganti, and S. X. Chen, IEEE Trans. Magn. **34**, 1294 (1998).

[36] G. J. Tomka, J. G. Gore, J. Earl, N. Murray, M. G. Maylin, and P. T. Squire, J. Magn. Magn. Mater. **219**, 275 (2000).

[37] B. Kvasnica and F. Kundracík, J. Magn. Magn. Mater. **162**, 43 (1996).

[38] D. C. Jiles, A. Ramesh, Y. Shi, and X. Fang, IEEE Trans. Magn. **33**, 3961 (1997).

[39] W. C. Stoner and W. P. Wohlfarth, Philos. Trans. Roy. Soc. London **240**, 599 (1948).

[40] E. P. Wohlfarth, J. Appl. Phys. **29**, 595 (1958).

[41] O. Henkel, Planet. Space Sci. **7**, 919 (1964).

[42] M. Corte-Real, Z. Chen, H. Okumura, and G. Hadjipanayis, IEEE Trans. Magn. **36**, 3306 (2000).

[43] V. Villas-Boas, S. A. Romero, and F. P. Missell, J. Appl. Phys. **81**, 4434 (1997).

[44] D. R. Comejo, F. P. Missell, and J. M. González, J. Appl. Phys. **79**, 6312 (1996).

[45] B. Alessandro, C. Beatrice, G. Bertotti, and A. Montorsi, J. Appl. Phys. **68**, 2901 (1990).

[46] B. Alessandro, C. Beatrice, G. Bertotti, and A. Montorsi, J. Appl. Phys. **68**, 2908 (1990).

[47] S. Zapperi, P. Cizeau, G. Durin, and H. E. Stanley, Phys. Rev. B **58**, 6353 (1998).

[48] E. Vives and A. Planes, Phys. Rev. B **63**, 134431 (2001).

[49] E. Vives and A. Planes, Phys. Rev. B **50**, 3839 (1994).

[50] O. Hovorka and G. Friedman, `cond-mat/0306300`.

[51] C. P. Bean, Rev. Mod. Phys. **36**, 31 (1964).

[52] D.-X. Chen, A. Sanchez, and J. S. Muñoz, J. Appl. Phys. **67**, 3430 (1990).

[53] Y. B. Kim, C. F. Hempstead, and A. R. Strnad, Phys. Rev. **129**, 528 (1963).

[54] P. W. Anderson, Phys. Rev. Lett. **9**, 309 (1962).

[55] K. Yamamoto, H. Mazaki, and H. Yasuoka, Phys. Rev. B **47**, 915 (1993).

[56] S. Tochihara, H. Yasuoka, and H. Mazaki, Physica C **295**, 101 (1998).

[57] S. Tochihara, H. Yasuoka, and H. Mazaki, Physica C **268**, 241 (1996).

[58] P. Chaddah, S. B. Roy, S. Kumar, and K. V. Bhagwat, Phys. Rev. B **46**, 11737 (1992).

[59] J. Tellinen, IEEE Trans. Magn. **34**, 2200 (1998).

[60] S. E. Zirka and Y. I. Moroz, IEEE Trans. Magn. **35**, 2090 (1999).

[61] H. Hauser, J. Appl. Phys. **75**, 2584 (1994).

[62] J. H. Krah and A. J. Bergqvist, Physica B **343**, 35 (2004).

[63] J. Zhang, S.-Y. Zhang, H.-W. Zhang, and B.-G. Shen, J. Appl. Phys. **89**, 5601 (2001).

[64] M. A. Wells, R. W. Fitzpatrick, R. J. Gilkes, and J. Dobson, Geophys. J. Int. **138**, 571 (1999).

[65] A. Yan, A. Bollero, O. Gutfleisch, and K.-H. Müller, J. Phys. D: Appl. Phys. **35**, 835 (2002).

[66] W.-Y. Zhang, X.-D. Zhang, Y.-C. Yang, and B.-G. Shen, J. Alloys Comp. **353**, 274 (2003).

[67] E. Girt, K. M. Krishnan, G. Thomas, E. Girt, and Z. Altounian, J. Magn. Magn. Mater. **231**, 219 (2001).

[68] J. H. Carpenter, K. A. Dahmen, J. P. Sethna, G. Friedman, S. Loverde, and A. Vanderveld, J. Appl. Phys. **89**, 6799 (2001).

[69] J. H. Carpenter, K. A. Dahmen, A. C. Mills, M. B. Weissman, A. Berger, and O. Hellwig, `cond-mat/0401023`.

[70] M. T. Johnson, P. J. H. Bloemen, F. J. A. den Broeder, and J. J. de Vries, Rep. Prog. Phys. **59**, 1409 (1996).

[71] C. Kittel, Phys. Rev. **70**, 965 (1946).

[72] O. Hellwig, G. P. Denbeaux, J. B. Kortright, and E. E. Fullerton, Physica B **336**, 136 (2003).

[73] J. E. Davies, K. Liu, O. Hellwig, and E. E. Fullerton, unpublished.

[74] S. Y. Jeong, Z. S. Shan, and D. J. Sellmyer, Jpn. J. Appl. Phys. **37**, 819 (1998).

[75] M. Pardavi-Horvath and G. Vertesy, IEEE Trans. Magn. **33**, 3975 (1997).

[76] A. Lisfi and J. C. Lodder, J. Phys.: Condens. Matter **14**, 12339 (2002).

[77] H. Hauser and R. Groessinger, IEEE Trans. Magn. **39**, 2887 (2003).

[78] D. Wang, R. D. Kirby, B. W. Robertson, and D. J. Sellmyer, J. Appl. Phys. **73**, 6353 (1993).

[79] D. R. Cornejo and F. P. Missell, J. Magn. Magn. Mater. **203**, 41 (1999).

[80] H.-W. Zhang, W.-Y. Zhang, A.-R. Yan, Z.-G. Sun, B.-G. Shen, I.-C. Tung, and T.-S. Chin, Mater. Sci. Eng. A **304-306**, 997 (2001).

[81] C. S. Schneider, J. Appl. Phys. **91**, 7637 (2002).

[82] C. S. Schneider, J. Appl. Phys. **89**, 1281 (2001).

[83] J. L. Tsai, T. S. Chin, E. Y. Huang, and S. K. Chen, J. Appl. Phys. **83**, 6241 (1998).

[84] I. A. Al-Omari and D. J. Sellmyer, Phys. Rev. B **52**, 3441 (1995).

[85] Z. Hong-Wei, R. Chuan-Bing, Z. Jian, Z. Shao-Ying, and S. Bau-Gen, Acta Phys. Sin. **52**, 722 (2003).

[86] M. Polak and L. Krempasky, Physica C **357-360**, 1144 (2001).

[87] A. K. Pradhan, K. Kuroda, T. Takagi, and N. Koshizuka, Physica C **300**, 77 (1998).

[88] J. M. Cruz-Hernández and V. Hayward, IEEE Trans. Contr. Syst. Technol. **9**, 17 (2001).

[89] J. R. Petta, M. B. Weissman, and G. Durin, Phys. Rev. E **56**, 2776 (1997).

[90] M. C. Kuntz and J. P. Sethna, Phys. Rev. B **62**, 11699 (2000).

[91] G. Durin and S. Zapperi, Phys. Rev. Lett. **84**, 4705 (2000).

[92] H. Ji and M. O. Robbins, Phys. Rev. A **44**, 2538 (1991).

[93] M. C. Kuntz, O. Perković, K. A. Dahmen, B. W. Roberts, and J. P. Sethna, Comput. Sci. Eng. **1**, 73 (1999).

[94] O. Perković, K. A. Dahmen, and J. P. Sethna, Phys. Rev. B **59**, 6106 (1999).

[95] P. Bak, C. Tang, and K. Wisenfeld, Phys. Rev. A **38**, 364 (1998).

[96] J. S. Urbach, R. C. Madison, and J. T. Markert, Phys. Rev. Lett. **75**, 276 (1995).

[97] P. Shukla, Phys. Rev. E **62**, 4725 (2000).

[98] P. Shukla, Phys. Rev. E **63**, 027102 (2001).

[99] F. Colaiori, A. Gabrielli, and S. Zapperi, Phys. Rev. B **65**, 224404 (2002).

[100] L. Dante, G. Durin, A. Magni, and S. Zapperi, Phys. Rev. B **65**, 144441 (2002).

[101] S. Zapperi, A. Magni, and G. Durin, J. Magn. Magn. Mater. **242-245**, 987 (2002).

[102] H. G. Katzgraber, G. Friedman, and G. T. Zimányi, Physica B **343**, 10 (2004).

[103] J. H. Carpenter and K. A. Dahmen, Phys. Rev. B **67**, 020412(R) (2003).

[104] O. Perković, K. Dahmen, and J. P. Sethna, Phys. Rev. Lett. **75**, 4528 (1995).

[105] A. P. Roberts, C. R. Pike, and K. L. Verosub, J. Geophys. Res. **105**, 28461 (2000).

[106] M. C. Kuntz and J. P. Sethna, unpublished.

[107] N. Goldenfeld, *Lectures on Phase Transitions and the Renormalization Group* (Addison Wesley, 1992).

[108] O. Perković, Ph.D. thesis, Cornell University (1996).

[109] K. A. Dahmen, D. R. Nelson, and N. M. Shnerb, J. Math. Biol. **41**, 1 (2000).

[110] K. A. Dahmen, D. R. Nelson, and N. M. Shnerb, in *Statistical Mechanics of Biocomplexity*, edited by D. Reguera, J. M. G. Vilar, and J. M. Rubí (Springer, Berlin, 1999), p. 124.

[111] A. L. Lin, B. A. Mann, G. Torres-Oviedo, B. Lincoln, J. Käs, and H. L. Swinney, Biophys. J. **87**, 75 (2004).

[112] T. Neicu, A. Pradhan, D. A. Larochelle, and A. Kudrolli, Phys. Rev. E **62**, 1059 (2000).

[113] N. M. Shnerb, Phys. Rev. E **63**, 011906 (2000).

[114] D. R. Nelson and N. M. Shnerb, Phys. Rev. E **58**, 1383 (1998).

[115] B. Drossel and M. Kardar, Phys. Rev. B **66**, 195414 (2002).

[116] R. A. Fisher, Ann. Eugenics **7**, 355 (1937).

[117] A. Kolmogorov, I. Petrovsky, and N. Piskunov, Bull. Univ. Moscow. Ser. Intl. Sec. A **1**, 1 (1937).

[118] A. Lemarchand, A. Lesne, and M. Mareschal, Phys. Rev. E **51**, 4457 (1995).

[119] N. Hatano and D. R. Nelson, Phys. Rev. B **56**, 8651 (1997).

[120] T. Halpin-Healy and Y.-C. Zhang, Phys. Rep. **254**, 215 (1995).

[121] M. Kardar and Y.-C. Zhang, Phys. Rev. Lett. **58**, 2087 (1987).

[122] D. Forester, D. R. Nelson, and M. J. Stephen, Phys. Rev. A **16**, 732 (1977).

[123] M. C. Kuntz and J. P. Sethna.
URL `http://www.lassp.cornell.edu/sethna/hysteresis/code`

[124] The Materials Computation Center software archive may be accessed through their main website found at the following address.
URL `http://www.mcc.uiuc.edu/`

[125] L. Neél, Compt. rend. (Paris) **246**, 2313 (1958).

[126] L. Neél, J. Phys. radium **20**, 215 (1959).

[127] W. H. Press, S. A. Teukolsky, W. T. Vetterling, and B. P. Flannery, *Numerical Recipes in C* (Cambridge University Press, 1992).

[128] The GNU C library.
URL `http://www.gnu.org/software/libc/libc.html`

[129] G. Durin, G. Bertotti, and A. Magni, Fractals **3**, 351 (1995).

[130] The FFTW library was used to compute the discrete Fourier transforms.
URL `http://www.fftw.org/`

[131] R. A. White, K. A. Dahmen, and A. Travesset, unpublished.

Curriculum Vitae

PERSONAL DATA

Name: John H. Carpenter

Born: 1977

Citizenship: USA

EDUCATION

Graduate

University of Illinois at Urbana-Champaign (UIUC) (June 1999 – October 2004)

Degree: Ph.D. in Physics (2004)

Thesis topic: History induced critical behavior in disordered systems and bacterial spreading in highly advective, random environments.

Thesis advisor: Professor Karin A. Dahmen

Undergraduate

Kansas State University (KSU) (August 1995 to May 1999)

Degree: B.S. in Physics and Math, with Chemistry Minor (1999)

PROFESSIONAL EMPLOYMENT

Graduate Research Assistant

Department of Physics, UIUC, 2001-present.

Advisor: Professor Karin A. Dahmen

- Investigated the role of history in the hysteresis curves of magnets using the Random Field Ising Model (RFIM).
- Derived consistent scaling picture for demagnetization curve and subloops.
- Modified existing code to allow arbitrary histories and a fool-proof interface.
- Developed algorithms for simulating RFIM (short and long range).
- Collaborated with experimentalists to test theoretical predictions.
- Numerically tested prediction of super-diffusive bacterial spreading.

Graduate Teaching Assistant

Department of Physics, UIUC, Spring 2001 and Fall 2000 semesters.

Supervisors: Professors Susan A. Lamb and Philip W. Phillips

- Taught laboratory sessions for the first course in engineering physics (mechanics).
- Led help sessions before examinations.

Undergraduate Research

Department of Physics, KSU, Summers of 1996-1998.

Supervisor: Professor Bruce M. Law

- Developed new model for bulk order parameter surface scaling functions.
- Determined model's coefficients through numerical calculations and comparison with experiment.
- Investigated finite size effects in critical wetting films.
- Collected data on samples using a Brewster angle ellipsometer.

Research Apprentice

USDA Grain Marketing and Production Research Laboratory, Summer 1995
Supervisor: Dr. Inna Zayas

- Created algorithm to analyze bread grain images.
- Evaluated a digital image processing platform for future use.

AWARDS and FELLOWSHIPS

Outstanding Teacher Award (Fall 2000 and Spring 2001)
Distinguished University Fellowship (UIUC 1999)
Goldwater Scholarship (KSU 1997)

PUBLICATIONS

- J. H. Carpenter and K. A. Dahmen, "Super-diffusive spreading in highly advective, disordered environments", pre-print.
- J. H. Carpenter, K. A. Dahmen, A. C. Mills, M. B. Weissman, A. Berger, and O. Hellwig, "History-Induced Critical Behavior in Disordered Systems", submitted to *Phys. Rev. Letters.*

- J. H. Carpenter and K. A. Dahmen, "Barkhausen noise and critical scaling in the demagnetization curve", *Phys. Rev. B* **67**, 020412(R) (2003).

- J. H. Carpenter, K. A. Dahmen, J. P. Sethna, G. Friedman, S. Loverde, and A. Vanderveld, "Subloops, Barkhausen noise, and disorder induced critical behavior", *J. Appl. Phys.* **89**, 6799 (2001).

- J. H. Carpenter, J.-H. J. Cho, and B. M. Law, "Ellipsometric determination of universal critical adsorption scaling functions", *Phys. Rev. E* **61**, 532 (2000).

- J. H. Carpenter, B. M. Law, and D. S. P. Smith, "Universal surface scaling function for critical adsorption", *Phys. Rev. E* **59**, 5655 (1999).

TALKS at CONFERENCES

- "The role of long-range fields for history-induced critical scaling in disordered systems." 2004 March Meeting of the American Physical Society, Montreal, Quebec, Canada, March 22–26, 2004.

- "The role of long-range fields for history-induced critical scaling in magnets." 9th Joint MMM-Intermag Conference, Anaheim, CA January 5–9, 2004.

- "Super-diffusive Bacterial Growth in Highly Advective Random Environments" 2003 March Meeting of the American Physical Society, Austin, TX March 3–7, 2003.

- "Disorder Induced Critical Scaling and Barkhausen Noise in Demagnetization Curves" 2002 March Meeting of the American Physical Society, Indianapolis, IN March 18–22, 2002.

- "Subloops, Avalanches, and History-Induced Critical Behavior in Disordered Systems" 2001 March Meeting of the American Physical Society, Seattle, WA

March 12–16, 2001.

- "Subloops, Barkhausen Noise, and History Induced Critical Behavior" 8th Joint MMM-Intermag Conference, San Antonio, TX January 7–11, 2001.
- "Universal scaling functions for critical adsorption" Centennial Meeting of the American Physical Society, Atlanta, GA March 20–26, 1999.

PERSONAL REFERENCES

- Prof. Karin A. Dahmen
  Department of Physics
  University of Illinois at Urbana-Champaign
  1110 W. Green St., Urbana, IL 61801
  Phone: (217)244-8873
  E-mail: dahmen@uiuc.edu
- Prof. Michael B. Weissman
  Department of Physics
  University of Illinois at Urbana-Champaign
  1110 W. Green St., Urbana, IL 61801
  Phone: (217)333-7897
  E-mail: mbw@uiuc.edu
- Dr. Andreas Berger
  Hitachi Global Storage Technologies
  San Jose Research Center
  650 Harry Rd., San Jose, CA 95120
  Phone: (408)323-7210

E-mail: Andreas.Berger@hgst.com

RESEARCH ACCOMPLISHMENTS AND CURRENT RESEARCH

- **Barkhausen noise and Critical Scaling in the Demagnetization Curve**, with Karin A. Dahmen.

  The demagnetization curve, or initial magnetization curve, was studied by examining the embedded Barkhausen noise using the non-equilibrium, zero temperature random-field Ising model. The demagnetization curve was found to reflect the critical point seen as the system's disorder is changed. Critical scaling was found for avalanche sizes and their second moments, correlation functions, and the size and number of spanning avalanches. The critical exponents were derived from those related to subloops. Finally, the behavior in the presence of long range demagnetizing fields was found to be the same as for the saturation loop. Results were obtained from simulations of up to one million spins.

- **History-Induced Critical Behavior in Disordered Systems**, with Karin A. Dahmen, Andrea C. Mills, Michael B. Weissman, Andreas Berger, and Olav Hellwig.

  The effect of history on Barkhausen noise as found in magnets was studied both with and without the presence of long-range (LR) demagnetizing fields using the non-equilibrium, zero-temperature random-field Ising model. Two distinct subloop behaviors arose and were shown to be in qualitative agreement with experiments on thin film magnets and soft ferromagnets. With LR fields present subloops resembled a self-organized critical system, while their absence resulted in subloops that reflected the critical point seen in the saturation loop as the system disorder changes. In the former case, power-law distributions of noise were found in subloops, while in the latter case a critical subloop was discovered inside which history-induced critical scaling was found in avalanche size distributions, spin-flip correlation functions, and finite-size scaling of the second moments of the size distributions. This scaling was shown to differ from that found in the saturation loop and demagnetization curve. Results were obtained from simulations of over 10^8 spins.

- **Super-diffusive Bacterial Spreading in Highly Advective Random Environments**, with Karin A. Dahmen and David R. Nelson.

  The growth of bacteria was studied in the large velocity limit using a reaction-diffusion equation with Fisher-like growth terms. This included a growth term proportional to the bacterial concentration in addition to a nonlinear term to prevent unbounded growth. An additional random growth term was added to simulate the spatial fluctuation of nutrients in the environment. Recent calculations for such a model with only linear terms predicted that in the highly advective regime bacterial growth is super-diffusive in directions orthogonal to the convection velocity [D. R. Nelson and N. M. Shnerb, Phys. Rev. E 58, 1383 (1998)]. These predictions were tested via numerical simulations of a simplified one-dimensional equation as well as the linear equation in two dimensions. Super-diffusive behavior was found in both cases. The onset of nondiffusive behavior was found to agree with a crossover time obtained from a perturbative expansion of the simplified equation. The full nonlinear equation was also numerically simulated and found to exhibit spreading with a wavefront velocity, identical in both directions, that was larger than the Fisher velocity.

- **Universal surface scaling functions for critical adsorption**, with Bruce

M. Law, D. S. P. Smith, and J.-H. J. Cho.

The one and two phase universal surface scaling functions describing critical adsorption at noncritical interfaces of critical binary liquid mixtures was studied. While the asymptotic behavior near and far from the surface has been well described, the crossover regime between the two behaviors is poorly understood. A model scaling function was constructed to describe the ellipsometric critical adsorption data for four critical binary liquid mixtures. By numerically calculating the effective signal from the model functions, a quantitative fit of the experimental data was obtained along with 95% confidence levels for the functions.

Generally, I have a wide range of interest in the simulation and modeling of systems. One topic in particular that interests me is the optimization of algorithms through new techniques as well as through parallelization. This is important for many types of simulations which require large amounts of resources, like time and memory, to obtain usable results. While simulations are an engaging topic, I also enjoy working in the world of experimental analysis. This includes crafting models to conform with and predict experiments as well as interpreting the physical data itself. Finally, I also find the general area of software development appealing. Specifically, I am interested in quality assurance and also usability issues such as well documented, intuitive interfaces.